ORNL/TM-2023/2970

FUSION MATERIALS RESEARCH AT OAK RIDGE NATIONAL LABORATORY IN FISCAL YEAR 2022

Y. Katoh

C. On

C. M. Parish

July 2023

OAK RIDGE National Laboratory

ORNL IS MANAGED BY UT-BATTELLE LLC FOR THE US DEPARTMENT OF ENERGY

DOCUMENT AVAILABILITY
Reports produced after January 1, 1996, are generally available free via OSTI.GOV.

Website www.osti.gov

Reports produced before January 1, 1996, may be purchased by members of the public from the following source:

National Technical Information Service
5285 Port Royal Road
Springfield, VA 22161
Telephone 703-605-6000 (1-800-553-6847)
TDD 703-487-4639
Fax 703-605-6900
E-mail info@ntis.gov
Website http://classic.ntis.gov/

Reports are available to US Department of Energy (DOE) employees, DOE contractors, Energy Technology Data Exchange representatives, and International Nuclear Information System representatives from the following source:

Office of Scientific and Technical Information
PO Box 62
Oak Ridge, TN 37831
Telephone 865-576-8401
Fax 865-576-5728
E-mail reports@osti.gov
Website https://www.osti.gov/

This report was prepared as an account of work sponsored by an agency of the United States Government. Neither the United States Government nor any agency thereof, nor any of their employees, makes any warranty, express or implied, or assumes any legal liability or responsibility for the accuracy, completeness, or usefulness of any information, apparatus, product, or process disclosed, or represents that its use would not infringe privately owned rights. Reference herein to any specific commercial product, process, or service by trade name, trademark, manufacturer, or otherwise, does not necessarily constitute or imply its endorsement, recommendation, or favoring by the United States Government or any agency thereof. The views and opinions of authors expressed herein do not necessarily state or reflect those of the United States Government or any agency thereof.

ORNL/TM-2023/2970

Materials Science and Technology Division

FUSION MATERIALS RESEARCH AT OAK RIDGE NATIONAL LABORATORY IN FISCAL YEAR 2022

Complied by:
Y. Katoh
C. On
C. M. Parish

June 2023

Prepared by
OAK RIDGE NATIONAL LABORATORY
Oak Ridge, TN 37831
managed by
UT-BATTELLE LLC
for the
US DEPARTMENT OF ENERGY
under contract DE-AC05-00OR22725

CONTENTS

1. INTRODUCTION

Y. Katoh and C. M. Parish

The materials science challenge of providing a suite of suitable materials to satisfy the technology to achieve fusion energy is addressed in this ORNL program. The inability of currently available materials and components to withstand the harsh fusion nuclear environment requires development of new materials, and an understanding of their response to the fusion environment. The overarching goal of the ORNL fusion materials program is to provide the applied materials science support and materials understanding to underpin the ongoing DOE Office of Science - Fusion Energy Sciences program, in parallel with developing the materials for fusion power systems. In this effort the program continues to be integrated both with the larger U.S. and international fusion materials communities and with the U.S. and international fusion design and technology communities.

The excitement of this program comes from the priorities given to this subject in the two recent fusion reviews, by the FESAC and NAS committees. An important element of those recommendations is the support for the long-advocated Fusion Prototypic Neutron Source, and for the Fusion Pilot Plant study that will help focus program direction and efforts.

This eleventh annual report of the ORNL (Oak Ridge National Laboratory) Fusion Reactor Materials Program summarizes the accomplishments in Fiscal Year 2022 (FY2022). The year was again productive but reflected the tail of the COVID19 work restrictions. The prevalence of COVID19 in the U.S. disrupted all program work since mid-March 2020. Program travel, workshops, and in-person technical meetings began again in FY2022. The reduced experimental tempo of FY2021 manifested in a slightly below-average number of publications for FY2022. The international assignees and students returned over the course of FY2022, and by the end of FY2022 the tempo was back to normal levels.

Following the pattern of planning used in this program, work for the year FY2022 and leading to FY2023 are focused on having the data and productivity to support a strong presence at the International Conference on Fusion Reactor Materials (ICFRM) 21, organized by Spain and scheduled for October 2023. For the ICFRM20 conference, held virtually in October 2021, ORNL presented more than 40 authored and coauthored papers in this virtual gathering of the world fusion materials community.

Two ARPA-E GAMOW awards initiated in FY2021 continued into FY2022. A collaboration with LLNL (Lawrence Livermore National Laboratory) and TAMU (Texas A&M University) is exploring Additive Manufacturing options for fabrication of Plasma Facing Components, and an ORNL effort is scaling up Castable Nanostructured Alloy production. Both projects continued actively with excellent productivity through FY2022.

The major elements of this long-running ORNL program continue to pursue development of low activation structural materials, with the greatest effort directed at the Reduced Activation Ferritic/Martensitic (RAFM) Steels, higher strength/higher creep resistant/coolant compatible/radiation tolerant advanced steels, and Silicon Carbide Composites. Tasks within the steels portfolio are pursuing several options for advanced steels: These include development of Castable Nanostructured Alloys (CNAs), exploratory work on Bainitic steels and Oxide Dispersion Strengthened (ODS) steels, and aluminum-containing iron-based alloys that promise improved liquid metal compatibility. Parallel to this is the increased emphasis on radiation effects, high heat flux testing and the development of refractory metals, especially tungsten materials. This includes the development and evaluation of new tungsten materials, and the study and understanding of the irradiation performance of tungsten. Newer efforts also support the Blanket and Fuel Cycle Programs. In each case the materials are being developed in a design-informed fashion where

properties improvements are led by fusion-relevant design studies and directed at advancing the Technology Readiness Level (TRL) of the material systems.

Effort continues on tasks initiated in FY2019, including the investigation of application of Additive Manufacturing (AM) technologies to the production of materials and components for fusion systems. While the development of tungsten AM technologies and compositionally graded tungsten-RAFMS transition was transferred to an FES/ARPA-E GAMOW program, fundamental study on thermal stability of the transition continues in this research. Moreover, development of additively nanostructured RAFMS and AM SiC ceramics & composites are explored.

Limited integrated fundamental modeling is included in the program, directed especially at understanding experimentally observed behavior. Recent focus has been on the irradiation effects in the W-Re-Os system and on exploring new options for solid ceramic tritium breeder candidate materials.

This fusion materials program makes heavy reliance on neutron irradiation in the High Flux Isotope Reactor (HFIR) at ORNL, complemented by limited use of ion irradiation facilities when these are better suited to explore fundamental aspects of materials behavior under irradiation. Associated with the HFIR irradiations is the infrastructure needed to evaluate the effects of the irradiation on the material properties and microstructures. This infrastructure includes: 1) hot cells, which are needed for capsule/experiment disassembly and for testing highly radioactive specimens; and 2) the Low Activation Materials Development and Analysis (LAMDA) Laboratory, which contains shielded test equipment for lower-level radioactive materials. Maintaining, upgrading, and replacing these state-of-the-art suites of instruments and test stands is an ongoing effort, shared with other programs focused on similar needs.

The fusion materials effort consists of a wide array of tasks and collaborations with both US and international partners. The major continuing international collaborating partners are the Japan Agency for Quantum and Radiological Science and Technology (QST), focused on structural materials, the Japanese National Institute for Fusion Sciences (the FRONTIER collaboration) and the Karlsruhe Institute of Technology in Germany, acting for EUROfusion (examining steel materials). A collaboration with the United Kingdom Atomic Energy Authority (UK AEA) was negotiated in FY2022 to start in FY2023.

Productivity and recognition of the ORNL Fusion Materials Program is demonstrated in Chapter 14 Awards, Honors and Recognition and Chapter 15 Publications and Presentations.

This research is funded by the Department of Energy, Office of Science, Office of Fusion Energy Sciences. We would like to acknowledge the active guidance that Daniel Clark of FES provides in setting the direction and priorities of this work, and his help in the effective conduct of the program.

2. ADVANCED STEELS

2.1 TENSILE PROPERTIES OF HFIR IRRADIATED ODS STEELS SHOW IRRADIATION HARDENING AND LOSS OF DUCTILITY UP TO HIGH TEMPERATURES

A. Bhattacharya, S.M. Levine, D.T. Hoelzer, J. Reed, J.W. Geringer, H. Tanigawa (QST), T. Nozawa (QST), S.J. Zinkle

2.1.1 OBJECTIVE

Different HFIR irradiated ODS steels (MA957, 12YWT, PM2000) were uniaxial tensile tested in the hot cells. These materials were irradiated in the QST collaboration in various irradiation capsules including JP26 and JP27. Previously, Vickers hardness data on these steels was reported. Here, results from the tensile tests at room temperature (RT) and irradiation temperature (T_{irr}) are presented. The results revealed significant irradiation hardening in ODS steels for T_{irr}>400 °C and up to 500 °C The results are compared with literature and with HFIR irradiated RAFM steels to develop a detailed understanding of low temperature hardening-embrittlement (LTHE) in ODS steels. This report details the dose and temperature dependent hardening and loss of ductility of the studied materials.

2.1.2 SUMMARY

Tensile tests were completed on 14% Cr base MA957, 12% Cr base 12YWT and 18% Cr-5.5%Al base PM2000 from JP26 and JP27 experiments (4.5 - 13.1 dpa, T_{irr} = 300, 450 and 500 °C). This report summarizes the uniaxial properties of the irradiated steels to quantify the irradiation hardening/loss of ductility behavior. The results from the present study are compared with HFIR irradiated RAFM steels (F82H) and with literature on MA957 irradiated in OSIRIS and BOR60 reactors. The results show significant irradiation hardening in ODS steels up to 450-500 °C. The data produced validated the previously reported Vickers hardness data on the same HFIR irradiated ODS steels showing hardening in this class of materials at temperatures where RAFM steels do not show much hardening (T_{irr} > 350-400 °C). The results suggest different underlying irradiation damage mechanisms might be operating in the high-Cr based ODS steels compared to RAFM steels. The elevated temperature hardening in ODS alloys might emerge as a design challenge for the first-wall/blanket structures in future fusion devices. The results highlight that different lower-operating-temperature limit should be considered for ODS as compared to RAFM steels purely from the LTHE issue.

2.1.3 PROGRESS AND STATUS

Numerous ODS alloys were neutron irradiated at ORNL in various irradiation experiments to map the dose-temperature dependent irradiation behavior of these materials. Here, irradiated tensile properties are summarized for samples irradiated in JP26 and JP27 experiments. Uniaxial tensile tests were performed in the hot cells at RT and 300 °C with guidance from ASTM E8 Standard Test Methods for Tension Testing of Metallic Materials and ASTM E21 Standard Test Methods for Elevated Temperature Tension Tests of Metallic Materials, using a strain rate of 10^{-3} s^{-1} (5×10^{-3} mm/s extension rate). Like previous studies, the tensile properties were measured using the tangent modulus method. RT tests were performed in air. Elevated temperature tests were performed in vacuum at pressures $\leq 5 \times 10^{-6}$ torr.

2.1.3.1 Compilation of dose-dependent irradiation hardening & loss of ductility:

The dose dependent yield stress (σ_{YS}) for MA957 and 12YWT are shown in Figure 1. Figure 1 also presents data for MA957 from literature and for HFIR irradiated F82H steels for comparison. Both MA957 and 12YWT showed significant irradiation hardening upon irradiation. At 300 °C, hardening in MA957 seems

to continuously increase with doses up to ~13.1 dpa, while 12YWT seems to show saturation between 4.5-13.1 dpa. Collectively looking at MA957 data from HFIR, OSIRIS and BOR60 suggest hardening in 14%Cr steels such as MA957 may not attain saturation up to high doses, such as ~35-40 dpa. Figure 1 compares the MA957 results from HFIR with previous research on bar type samples after irradiations in OSIRIS and BOR60 reactors where some differences between their hardening behavior can be seen. Although this difference is likely due to test temperature effects on measured irradiation hardening: HFIR samples were tested at RT while BOR60/OSIRIS samples were tensile tested at T_{irr}.

Additional high dose (>60 – 80 dpa) data is needed to identify the saturation hardening doses for these two materials.

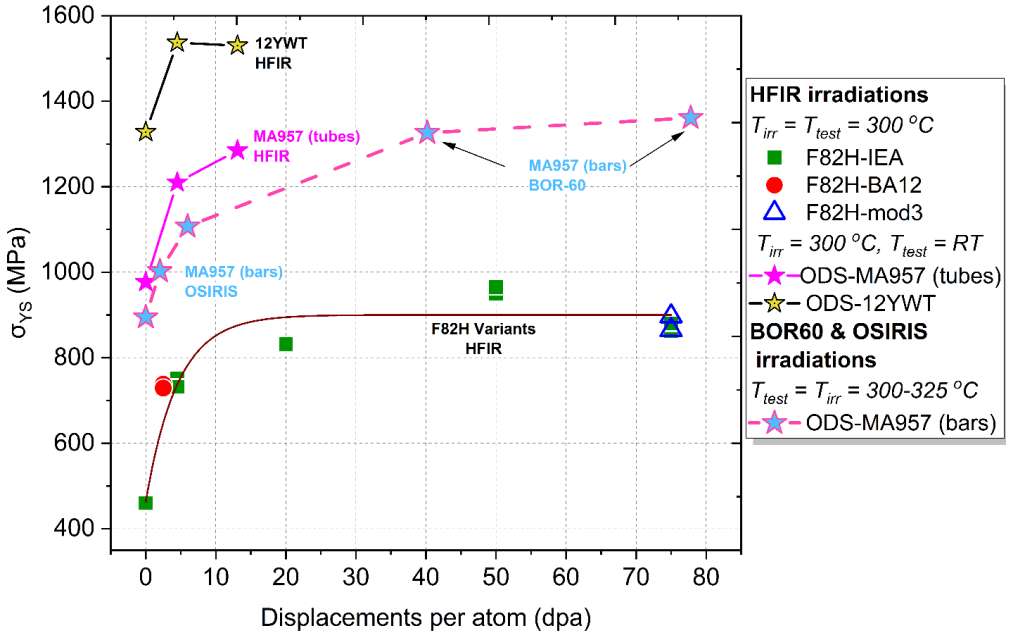

Figure 1. Dose dependent yield stress in F82H steel variants (IEA, BA12 and mod3), and ODS steels (MA957, 12YWT) after HFIR neutron irradiations at 300 °C. Literature results on MA957 is also plotted, with data taken from Refs. [1,2].

Figure 2 presents the dose dependent ductility, uniform plastic elongation (UEp) and total plastic elongations (TEp), with results compared to RAFM steels. While the RAFM steels typically lose UEp very rapidly, the elongation properties of the studied ODS steels were strongly material dependent. The 12YWT alloy behaved very similar to RAFM steels, showing an initial sharp loss in UEp and thereafter a tendency to saturate around ~0.4-0.6%. However, TEp of 12YWT seems to decrease continually with dose at least until ~13.1 dpa, with values much lower than those measured for RAFM steels. For 14%Cr based MA957, the ductility was significantly better than RAFM steels and 12YWT after irradiation. Initially, there is irradiation induced reduction of both UEp and TEp. However, the UEp remains higher than 8% for doses as high as 13.1 dpa. The UEp seems to saturate at these high values between ~4.5 to 13.1 dpa. The ductility of MA957 after irradiation in HFIR is compared with literature data after irradiations in OSIRIS and BOR60 reactors. The behavior is material dependent: overall the samples from MA957 tubes irradiated in HFIR performed better than samples taken from bars that were irradiated in BOR60/OSIRIS. For the bar type specimens, the UEp is still higher than typical values for RAFM steels like F82H. It should be noted that for all three neutron irradiation experiments (HFIR, BOR60 and OSIRIS), the samples were machined along

the extrusion direction implying this was the best-case scenario for tensile ductility. In ODS alloys, properties can be direction dependent, and it is likely the behavior may be different if samples perpendicular to the direction of extrusion were extracted.

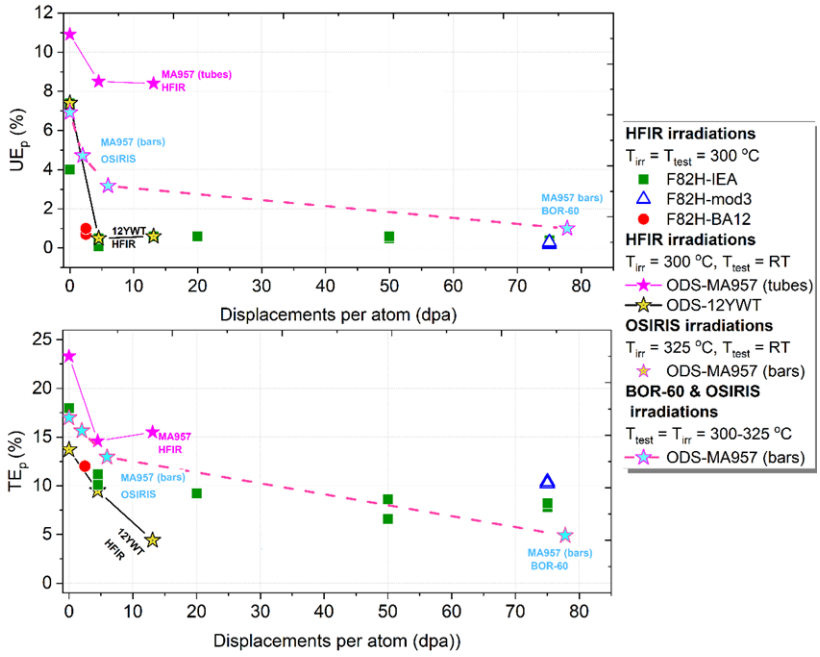

Figure 2. Dose dependent loss in uniform and total plastic elongations in F82H steel variants (IEA, BA12 and mod3), and ODS steels (MA957, 12YWT) after 300 °C HFIR neutron irradiations. Literature results on MA957 is also plotted, with data taken from Refs. [1,2]

2.1.3.2 Effect of irradiation temperature on irradiation hardening & loss of ductility:

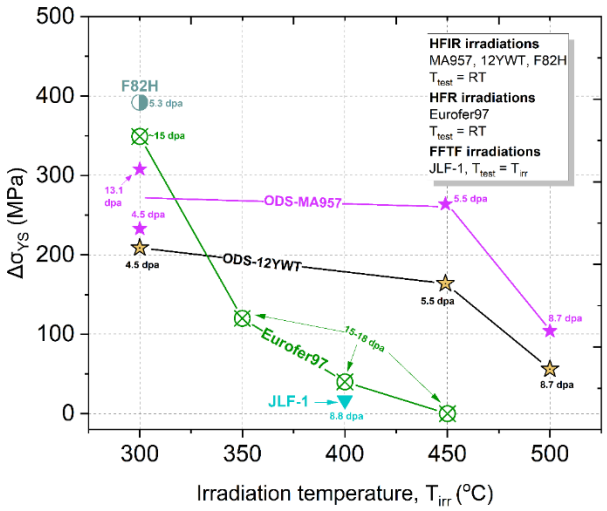

Figure 3. Temperature dependent irradiation hardening in HFIR irradiated ODS steels compared with literature on RAFM steels. Literature data taken from Refs. [3,4].

Figure 3 compiles the measured irradiation hardening, taken as the difference between nonirradiated and irradiated σ_{YS} of the ODS alloys irradiated in HFIR at 300, 450 and 500 °C and compares their properties to RAFM steels data in literature. The results showed significant irradiation hardening in MA957 and 12YWT alloys at high temperatures. Between 300 and 450 °C, there is not much recovery in hardening behavior. At 500 °C, there is a reduction in hardening but it is not completely recovered. This is an unexpected observation because for temperatures as high as 450-500 °C, irradiation hardening is not a major problem for RAFM steels – and RAFM steels often show softening at these temperatures. The results are consistent with previous low dose (0.01-0.75 dpa) data in literature from JMTR on a few Fe-Cr and Fe-Cr-Al based ODS steels [5]. The combined HFIR and JMTR results highlight that ODS steels with Cr concentrations >12 wt.% will continue hardening for temperatures as high as ~450 °C, and higher temperatures will be needed to suppress this behavior. Because hardening is directly related to degradation in fracture toughness, continued hardening up to high temperatures may pose a challenge to fusion first-wall/blanket designs using ODS alloys. The primary contributor to this hardening is Cr rich α' formation.

2.1.4 FUTURE RESEARCH

Atom probe tomography (APT) data were collected from all the HFIR irradiated ODS steels help explain the cause of this hardening. That study is now complete, and two manuscripts are under preparation.

2.1.5 REFERENCES:

[1] J. Henry, X. Averty, A. Alamo, Tensile and impact properties of 9Cr tempered martensitic steels and ODS-FeCr alloys irradiated in a fast reactor at 325 C up to 78 dpa, J. Nucl. Mater. 417 (2011) 99-103

[2] A. Alamo, J.L. Bertin, V.K. Shamardin, P. Wident Mechanical properties of 9Cr martensitic steels and ODS-FeCr alloys after neutron irradiation at 325 C up to 42 dpa. J. Nucl. Mater. 367-370 (2007) 54-59

[3] X. Chen, L. Clowers et al. Post-irradiation evaluation of eurofer97 fracture toughness using miniature multinotch bend bar specimens *American Society of Mechanical Engineers, Pressure Vessels and Piping Division (Publication) PVP* vol 1 pp 1–8 (2020)

[4] I. Sacksteder, H.-C. Schneider and E. Materna-Morris, Determining irradiation damage and recovery by instrumented indentation in RAFM steel , *J. Nucl. Mater.* 417 (2011) 127–30

[5] H.S. Cho, R. Kasada, A. Kimura, Effects of neutron irradiation on the tensile properties of high-Cr oxide dispersion strengthened ferritic steels, J. Nucl. Mater. 367-370 (2007) 239-243

2.2 ION IRRADIATION RESPONSE OF CASTABLE NANOSTRUCTURED ALLOYS

Tim Graening (ORNL), T.M. Kelsy Green (University of Michigan), Weicheng Zhong (ORNL), Kevin Field (University of Michigan), Lizhen Tan (ORNL)

2.2.1 OBJECTIVE

Two tailored castable nanostructured alloys (CNAs) have been ion-irradiated with single (Fe^{2+}) and dual beam (Fe^{2+} and He^{2+}) ion irradiation at 500 °C in a collaboration with University of Michigan to investigate the effects of ion irradiation on CNAs with different carbon contents. The objective of this work is to investigate the ion irradiation effects on and potential dissolution of MX-type and $M_{23}C_6$ precipitates and the formation of cavities in respect of the different carbon contents of two CNA alloys.

2.2.2 SUMMARY

Single and dual ion beam irradiation has been performed on tailored CNA steels to investigate temperature, dose, and carbon content dependencies and effects on the irradiation response. Here the cavity sizes and number densities have been investigated to determine dependence on the carbon content. The other results are investigated further in collaboration with the University of Michigan.

2.2.3 PROGRESS AND STATUS

CNA8 (high carbon) and CNA9 (low carbon) were manufactured for this study and their microstructures, together with elemental maps of Cr and Ti, are shown in transmission electron microscopy (TEM) images in Figure 4. Cr can usually be found as a major element in $M_{23}C_6$ and is only visible in the high carbon containing CNA8 in the first row of Figure 4. CNA9 mainly shows Ti-rich precipitates in different sizes with many nanosized precipitates visible in the bottom right micrograph.

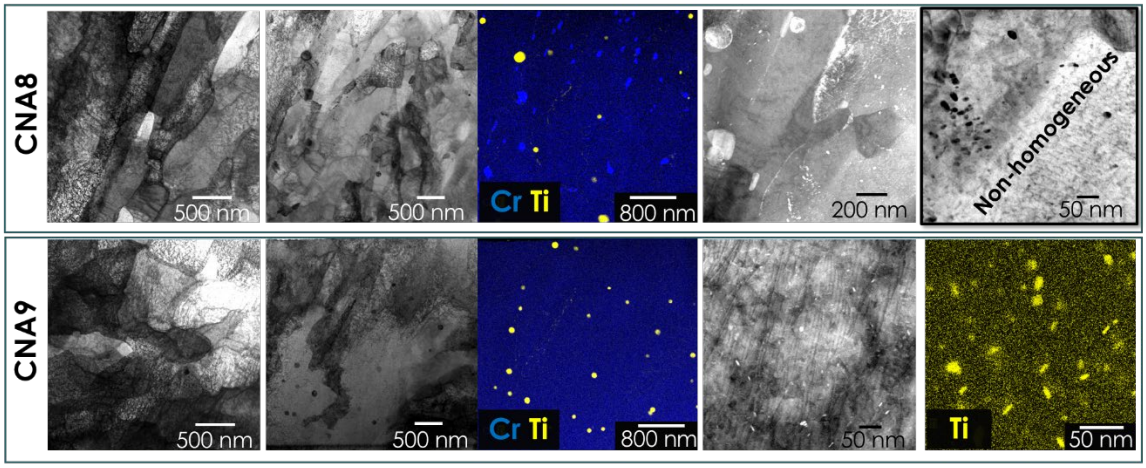

Figure 4. CNA8 and CNA9 microstructure in comparison with EDS maps of Cr (blue) and Ti (yellow) highlighting the precipitate formation.

Single and dual ion-beam irradiations with 15, 50, and 100 dpa were performed. The intended target ratio of 10 appm He per dpa was achieved in a depth between 600 and 1300 nanometer from the surface. It became obvious from the large amount of TEM samples that the investigated area highly influences the

number of precipitates and that even though the microstructure is macroscopically homogeneous, the area where the ion irradiation can be investigated is too limited in respect to the heterogeneous microstructure, as shown in Figure 5, where the left side of the micrograph shows significantly fewer $M_{23}C_6$ precipitates. For that reason, investigations of ballistic dissolution of precipitates need to be performed using in-situ experiments in the future, while cavity sizes and numbers were studied more extensively in this work. Over- and under-focused bright field (BF) images and high-angle annular dark field images in scanning TEM mode were utilized to identify cavities as a function of depth, binned to 200 nanometer sections in depth.

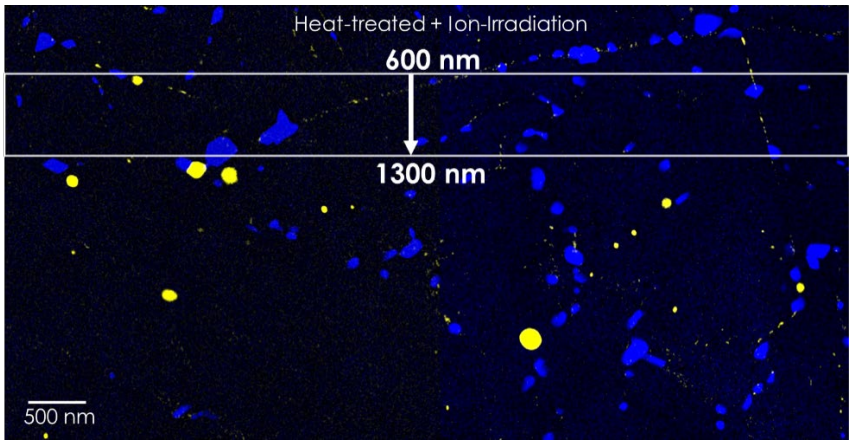

Figure 5 EDS map of Cr (blue) and Ti (yellow) with the invesitgated ion-irradiated area between 600 and 1300 nm.

The cavity sizes taken from the 50 and 100 dpa dual ion irradiation samples plotted in Figure 6 are clearly highlighting that a dose of 50 dpa led to slightly larger cavities in CNA9. After an ion-irradiation dose of 100 dpa no clear trend or difference between CNA8 and CNA9 is visible, with a higher number of smaller cavities and bubbles found in both alloys. That indicates that $M_{23}C_6$ carbides and the higher amount of carbon in CNA8 act as sinks at lower doses, but do not provide a difference in sink strength to pin cavities and He bubbles at 100 dpa.

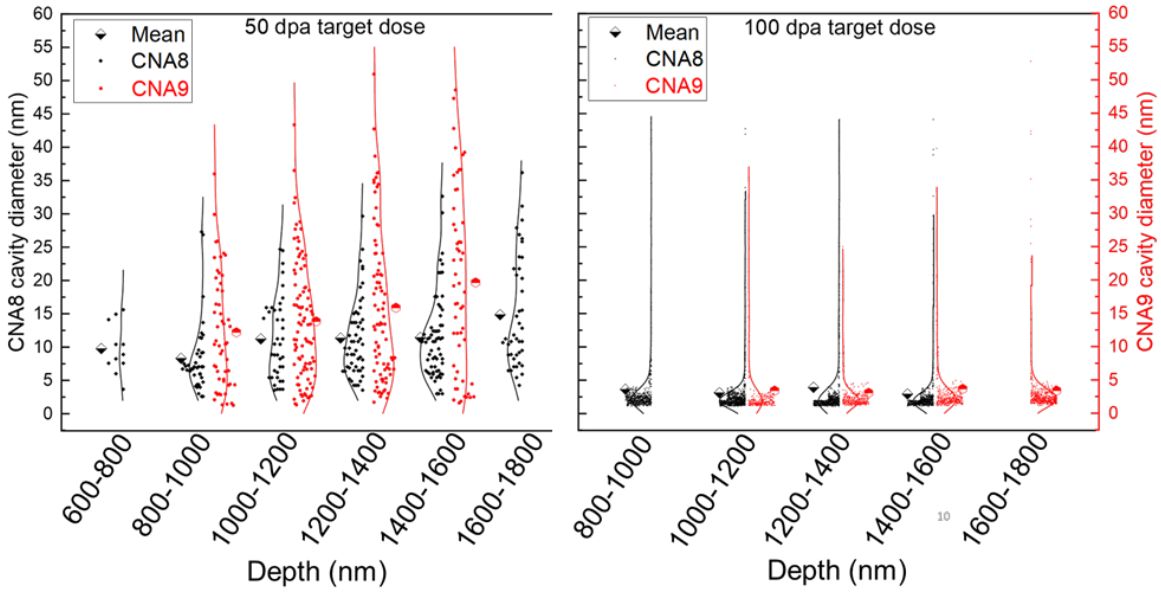

Figure 6 Cavity size diameter in CNA8 and CNA9 for 50 and 100 dpa target dose in respect to the ion irradiation depth.

Voids and He bubbles were not distinguished for the measure of counting, and "cavity" is used here to describe both. The cavity number was calculated in the same manner using the binned sections and is plotted in Figure 7. It is shown that while the cavity sizes for CNA8 and CNA9 are similar after 100 dpa, the number density increased for the high carbon CNA8 at 100 dpa. A slightly higher number density was measured for CNA9 after 50dpa. That indicates that a higher carbon content and more precipitation of $M_{23}C_6$ do not suppress the growth of cavities and their formation at very high doses. That potentially could be caused by the higher amount of nano-scaled MX precipitates in CNA9 but needs to be investigated further.

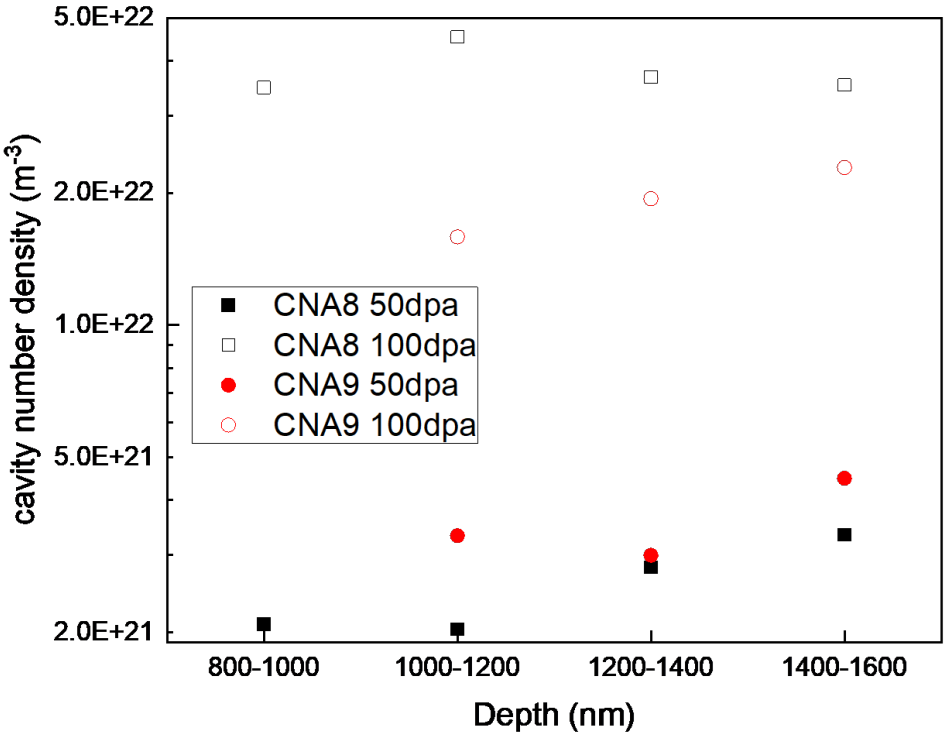

Figure 7 Cavity number density plotted against the ion irradiation depth for CNA8 and CNA9

2.2.4 FUTURE WORK

In-situ ion-irradiation experiments need to be performed to understand ballistic dissolution of MX precipitates under ion-irradiation in comparison with neutron irradiated samples.

2.3 $M_{23}C_6$ CARBIDES IN RAFM STEELS AND IN ADDITIVELY MANUFACTURED CONVENTIONAL FM STEELS SUFFER FROM RADIATION INDUCED AMORPHIZATION

A. Bhattacharya, S.M. Levine, S.J. Zinkle. W.-Y. Chen (ANL), P. Baldo (ANL), C.M. Parish, P.D. Edmondson

2.3.1 OBJECTIVE

Resilience of carbides in RAFM and conventional FM steels ultimately controls irradiation tolerance. In-situ irradiations were performed using energetic ions at the IVEM facility on extraction replica samples from a Eurofer97 steel and an additively manufactured Grade91 steel. Experimental results on amorphization behavior of $M_{23}C_6$ are presented. The experiments validated the use of replica samples for irradiation experiments to understand the amorphization behavior of different carbide phases in conventional FM and RAFM steels.

2.3.2 SUMMARY

1 MeV Kr^{2+} ion in-situ irradiations in a transmission electron microscope were performed on carbon extraction replica samples containing $M_{23}C_6$ carbides from FM steels: (i) Fe-9%Cr-1%W-TaV based Eurofer97 and (ii) Fe-9%Cr-1%Mo-VNb (all in wt.%) additively manufactured (AM) Grade91 steel. The irradiations were performed between 100 – 773 K up to a maximum dose of ~2.4 displacements per atom (dpa). The $M_{23}C_6$ carbides are highly susceptible to radiation induced amorphization (RIA). Between 100-423 K, RIA of $M_{23}C_6$ carbides occurs rapidly with critical amorphization doses ranging between ~0.35 – 0.9 dpa, increasing to higher doses at 573 K. The critical temperature for the crystalline-to-amorphous phase transformation ($T_{c\rightarrow a}$) of $M_{23}C_6$ carbides irradiated as replica samples, i.e. without the surrounding metal matrix, was estimated to be ~812 K. The critical amorphization dose of $M_{23}C_6$ carbides increases nearly exponentially with irradiation temperature. Comparing the present results with neutron irradiation data on bulk samples reveals a decrease in the critical amorphization dose for $M_{23}C_6$ and an increase of $T_{c\rightarrow a}$, highlighting the effect of dose rate on the amorphization behavior. Changes in the minor chemistry of $M_{23}C_6$, has negligible effect on the amorphization behavior.

2.3.3 PROGRESS AND STATUS

Figure 8 presents a dose-temperature map of $M_{23}C_6$ carbide evolution in Eurofer97, while Figure 9 presents a similar dose-T_{irr} mapping of $M_{23}C_6$ in AM-Grade91 steel. RIA of $M_{23}C_6$ occurred at all T_{irr} between cryogenic (100 K) and 773 K for doses up to 2.4 dpa. Complete amorphization of $M_{23}C_6$ occurred between 100-573 K, but particles stayed partially crystalline at higher temperatures. The doses at which $M_{23}C_6$ completely amorphized increased with T_{irr}. At each T_{irr}, the doses at which these carbides amorphized was nearly identical between the two studied alloys, suggesting the chemistry differences between $M_{23}C_6$ phase (M = Fe, Cr, W, V rich) in a RAFM steel versus $M_{23}C_6$ (M = Fe, Cr, Nb, Mo) in a conventional FM steel seems to have negligible effect on RIA.

The experimentally measured critical amorphization dose and amorphization onset doses are plotted in Figure 10 and fitted using the equation below:

$$D_c = \frac{D_0}{1-exp\left[\left(\frac{E_a}{k_b}\right)\left(\frac{1}{T_{c\rightarrow a}}-\frac{1}{T_{irr}}\right)\right]} \quad (1)$$

where D_0 is the dose to achieve amorphization at 0 K, k_b is Boltzmann's constant, E_a is activation energy (in eV) associated with defect migration/recombination, defect and ion diffusion in the amorphous material, or epitaxial recrystallization at the crystalline-amorphous interface [2]. Equation 1 provided an excellent fit for the experimental data in Figure 10. By fitting our experimental data with equation 1 and using a least squares refinement for each temperature, we obtained $T_{c\rightarrow a}$ of ~812 K for irradiations of extraction replicas.

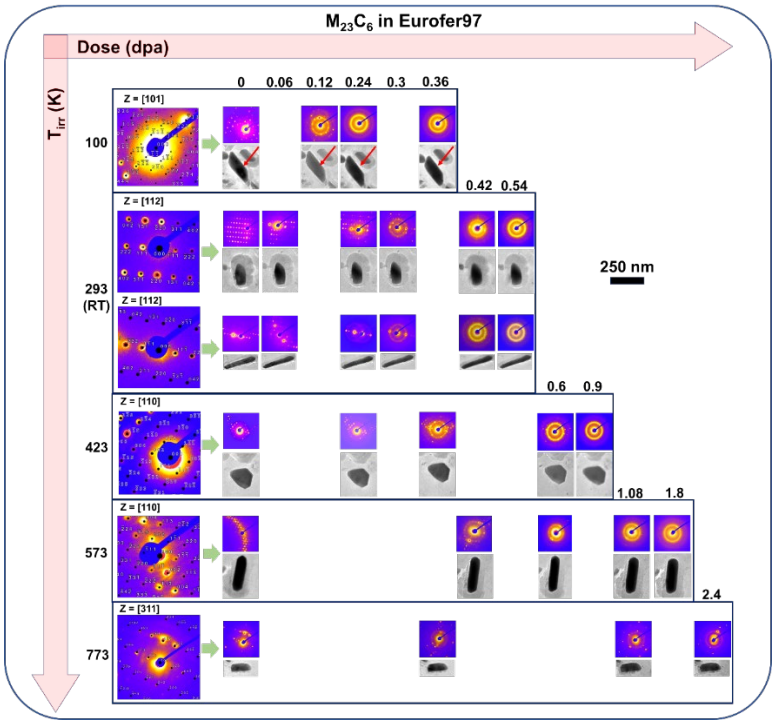

Remove this text and insert figure here

Figure 8. Dose-temperature mapping of RIA in $M_{23}C_6$ nanoprecipitates extracted from CEA-Eurofer97 steel and irradiated using 1 MeV Kr ions. The figure presents evolution of $M_{23}C_6$ particles using bright field (BF) TEM imaging and the associated nanobeam diffraction (NBD) patterns.

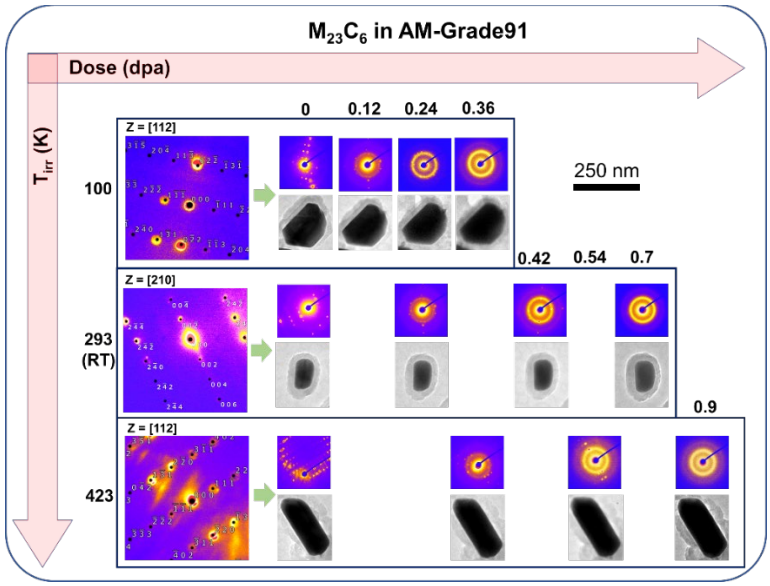

Figure 9. Dose-temperature mapping of RIA in $M_{23}C_6$ nanoprecipitates extracted from AM-Grade91 steel.

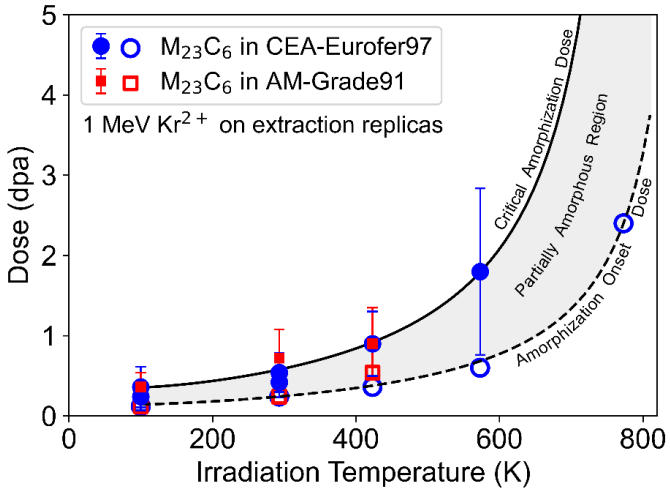

Figure 10. Evolution of critical amorphization dose and onset amorphization doses of $M_{23}C_6$ carbides in Eurofer97 and AM-Grade91 steel for irradiations using 1 MeV Kr^{2+} ions on extraction replica samples. Curves fitted using equation (1).

2.3.4 FUTURE RESEARCH

This study is complete with a publication [1]. Similar analysis methodologies are being applied to carbides/nitrides in HFIR irradiated RAFM steels.

2.3.5 REFERENCES:

[1] A. Bhattacharya, S.M. Levine, S.J. Zinkle. W.-Y. Chen, P. Baldo, C.M. Parish, P.D. Edmondson, Radiation induced amorphization of carbides in additively manufactured and conventional ferritic-martensitic steels: *In-situ* experiments on extraction replicas, J. Nucl. Mater 563 (2022) 153646.

[2] W.J. Weber, R.C. Ewing, C.R.A. Catlow, T. Diaz De La Rubia, L.W. Hobbs, C. Ki-Noshita, H. Matzke, A.T. Motta, M. Nastasi, E.K.H. Salje, E.R. Vance, S.J. Zinkle, Radiation effects in crystalline ceramics for the immobilization of high-level nuclear waste and plutonium, J. Mater. Res. 13 (1998) 1434–1484

2.4 ADVANCED CASTABLE NANOSTRUCTURED ALLOYS (CNAs) FOR FIRST-WALL/BLANKET APPLICATIONS

Ying Yang, Weicheng Zhong, Tim Graening, Lizhen Tan, Yutai Katoh

2.4.1 OBJECTIVE

The objective of this project is to establish a US-RAFM (reduced-activation ferritic-martensitic) steel based on the carbide-strengthened Castable Nanostructured Alloys (CNAs) and to demonstrate the viability and advantages of CNAs through the production and performance of industry-scale heats for use in integrated first-wall and blanket systems. This project is intended to establish or demonstrate a path toward technical feasibility for the fusion energy subsystem of integrated first-wall and blanket technologies, and improve the ease of maintainability, reduce regulatory risk, and increase environmental friendliness.

2.4.2 SUMMARY

In FY2022, the project efforts were primarily focused on procurements of two ton-scale CNA heats: 5-ton plates and 0.25-ton rods. Part of the 0.25-ton rods was used to make 0.045-in. diameter welding wire for weldability studies. The remaining rods and the 5-ton heat will be used to generate mechanical property measurements following the ASME standard. The irradiation behavior under ion and neutron irradiation, as well as liquid metal compatibility will also be studied for these two heats. For the 5-ton scale heat, ORNL signed a contract with the Saarschmiede GmbH (a producer of Eurofer97) and issued a purchase order in Oct. 2022. For the 0.25-ton scale rods, we have received both the 1 in. dia. rods and the 0.45 in. dia. welding wire made from the rods. We have evaluated the chemistry, microstructure, and mechanical properties of the rods. The compositions of the as-received CNAs rods meet the specified requirement; however, the hardness (94 HRB or 16 HRC) is lower than the design specification (102±2 HRB or 25±3 HRC). To increase the hardness, additional heat treatments were performed on the as-received CNA rods. Preliminary examination of hardness, tensile properties, and microstructure suggested the additionally heat-treated CNAs rods have achieved the design specification and they have comparable or better tensile properties than the previous lab-scale CNAs.

2.4.3 PROGRESS AND STATUS

The 5-ton scale heat was originally contracted to VDM Inc. The chemical analysis from the VIM ingot shows overall good control on composition except for the P content of 110 ppm which is greater than the design specification of 50 ppm. However, the subsequent ESR on the VIM ingot caused significant composition deviations for elements Cr, Ti, Ta, P, N, O, Ni and Cu from design specifications, rendering the VDM ingot a failed production. Due to the lack of VAR capability of VDM for improving the chemistry and unavailability of other domestic companies, we resorted to Saarchmiede GmbH (a German company who is a producer of Eurofer97) to make the 5-ton scale of CNAs. ORNL signed a contract and issued a PO to Saarschmiede GmbH in Oct. 2022. The company will warrant the chemistry of the produced CNAs to be compatible with the design specification by using clean raw materials and combining VIM and VAR techniques. The expected delivery will be in July or August of 2023.

The 0.25-ton scale heat was contracted to Metalwerks Inc. We have received both the rods and the welding wire made from the rods, as shown in Figure 11. The chemical analysis results for the rods and wires are listed in Table 1 below, which meets the design specification.

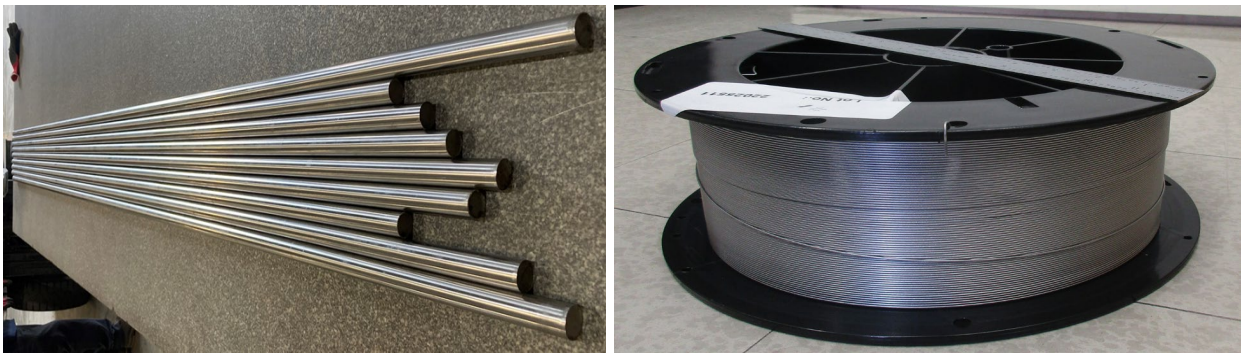

Figure 11. The 1 in. dia. rods (left) and 0.45 in. dia. welding wires (right) from the 0.25-ton heat..

Table 1: The chemical analysis results of CNA rods and the design specification

CNA	C	Cr	Mn	Si	Ta	Ti	W	V	Fe
Rod	0.1	8.4	0.47	0.15	0.045	0.12	1.18	0.05	Bal.
Nominal	0.1	8.5	0.5	0.12	0.045	0.12	1.3	0.05	Bal.
Tolerance	0.08~ 0.12	8.4~ 8.6	0.45~ 0.6	0.08~ 0.15	0.05~ 0.1	0.1~ 0.15	1.2~ 1.4	0.04~ 0.08	Bal.

The delivered CNA rods have met the desired composition specification; however, their hardness is 94 HRB or 16 HRC, which is lower than the design specification of 102±2 HRB or 25±3 HRC. To increase the hardness or strength of CNAs, we need to understand the primary strengthening mechanisms in carbide CNAs, which can be explained through the phase property diagram in Figure 12. There are two primary strengthening mechanisms: Lath boundary strengthening from martensite and precipitation strengthening from MC. Several metallurgical features are needed to ensure these mechanisms are active, as illustrated in Figure 12. First, a single γ phase (fcc austenite) window is needed at the high temperature where normalization heat treatment is performed. During subsequent quenching, the supersaturated austenite will transform to martensite. Second, a high-volume fraction of homogeneous distribution of MC nanoprecipitates are needed for precipitation strengthening. To achieve this, all solutes to form MC should be dissolved in the austenite during normalization and then precipitated during tempering. For the as-received rods, the normalization temperature and tempering temperature are 1050 °C and 750 °C, respectively, as shown in dashed lines in Figure 12. At 1050 °C, a large amount of C and Ti have already precipitated. The TiC precipitates formed at normalization temperature are large and have a neglectable contribution in strengthening the material. Therefore, for additional heat treatments, we need to push the normalization temperature higher, knowing that the prior austenite grain sizes will grow, potentially leading to larger martensite laths widths. On the other hand, the difference between the normalization and tempering temperatures determined the chemical driving force for precipitation kinetics at tempering temperature. The larger the difference, the greater the driving force for nucleation of precipitates resulting in more and smaller

MC precipitates. Therefore, we also push the tempering temperature lower, ensuring it is higher than the target operating temperature of 650 °C.

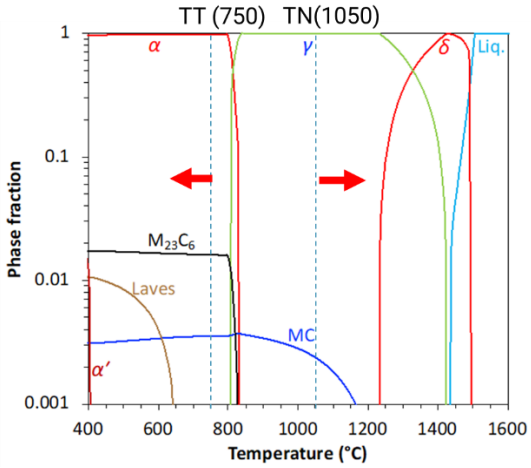

Figure 12. Phase fraction in the CNA rod alloy as a function of temperature

Following this strategy, the following seven heat treatments have been performed on the as-received rods:

1) Normalization at 1080 °C for 30min→water quench→tempering at 730 °C for 30min→air cooling
2) Normalization at 1130 °C for 20min→water quench→tempering at 730 °C for 30min→air cooling
3) Normalization at 1180 °C for 10min→water quench→tempered at 730C ° for 30min→air cooling
4) Normalization at 1130 °C for 20min→water quench→tempered at 750 °C for 30min→air cooling
5) Normalization at 1180 °C for 10min→water quench→tempered at 750 °C for 30min→air cooling
6) Normalization at 1180 °C for 10min→water quench→tempered at 710 °C for 30min→air cooling
7) Normalization at 1180 °C for 10min→water quench→tempered at 710 °C for 60min→air cooling

These heat treatments have normalization temperature that ranged from 1080 ℃ to 1180 ℃ and tempering temperature from 710 ℃ to 750 ℃. Rockwell B and/or Rockwell C hardness measurement have been performed on these heat-treated components. Four to eight measurements have been taken for the reported mean and deviation in Table 2. The hardness results suggested that HT3, HT6 and HT7 can produce hardness close to the design specification.

Table 2: Rockwell B and C hardness measurements on various heat-treated CNAs rods.

Samples	As received	HT1	HT2	HT3	HT4	HT5	HT6	HT7
HRB	93.9±0.7			95.6±0.4			101.4±0.3	101.3±0.2
HRC		17.2±0.2	19.6±0.5	21.8±0.3	18.4±0.1	19.4±0.1	23.3±0.2	23.1±0.7

In addition to the hardness measurement at room temperature, tensile properties have been evaluated at 23 ℃ and 600 ℃ for as-received, HT2, HT3, HT5, HT6, and HT7. Two tests have been performed for each condition to ensure repeatability. Figure 13 shows the stress-strain curves for both 23 ℃ and 600 ℃, with comparison to the lab-scale CNAs, reported in Ref. [1]. All heat-treated CNAs rods have demonstrated higher strength than the as-received CNAs rods at both 23 ℃ and 600 ℃, with some sacrifice of total

elongations at 23 °C. However, HT7 CNA rods demonstrates higher strength with ductility comparable to the as-received rod at 600 °C. The heat-treated rods also demonstrate better properties than the lab-scale CNAs [1]. For example, heat-treated CNA rods have higher ductility at 23°C with similar yield strength as the lab-scale CNAs. At 600 °C, the yield strength of HT6 and HT7 rods are approaching that of lab-scale CNAs, and with greater elongation.

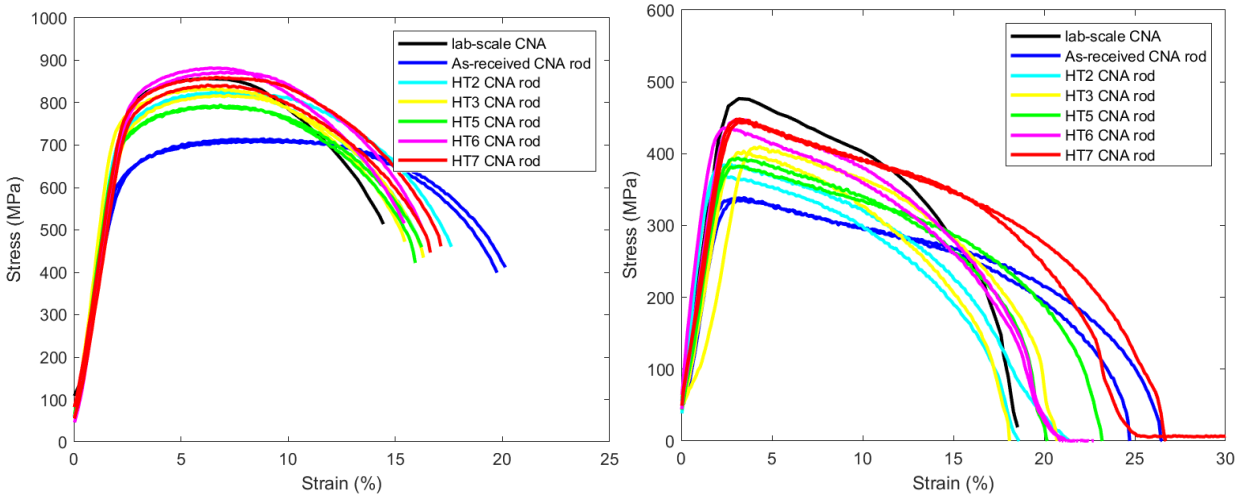

Figure 13. Tensile properties of CNA rods after multiple heat treatments and lab-scale CNAs [1] at 23 °C (left) and 600 °C (right). Two tests were performed for each condition.

Because we increased the normalization temperature from 1050 °C to 1180 °C, we need to check the prior austenite grain (PAG) size. The EBSD results from the as-received, HT3 and HT7 states are shown in Figure 14. We observed significant growth of PAG.

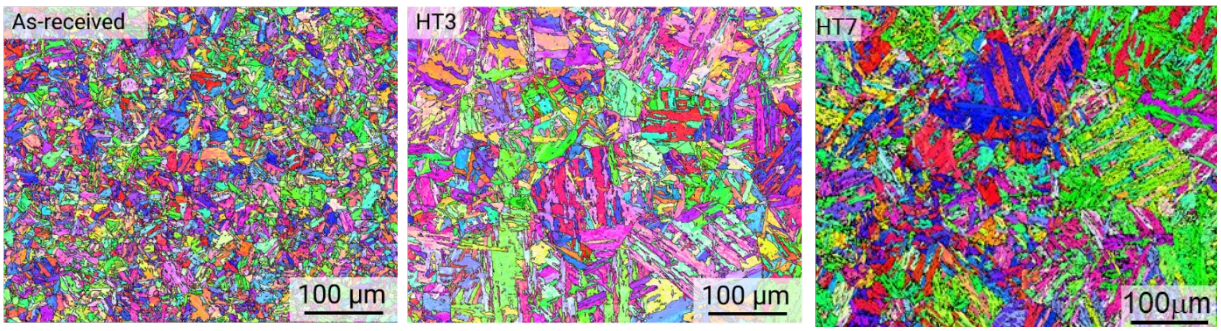

Figure 14. EBSD results showing the prior austenite grain size of the as-received, HT3 and HT7.

Microstructure characterization used scanning electron microscopy (SEM) for identifying the grain structure and precipitates. Examples of SEM images of as-received, HT3 and HT7 CNAs rods of different magnifications are provided in Figure 15. Tempered martensite structures are observed in all samples, with $M_{23}C_6$ precipitates distributed at prior-austenite grain boundaries. Most precipitates observed in the higher magnification images are $M_{23}C_6$, except a few larger and spherical TiC precipitates only in as-received CNA rods, labeled with yellow arrows. Characterization of nanoscale TiC precipitates using transmission electron microscopy is ongoing.

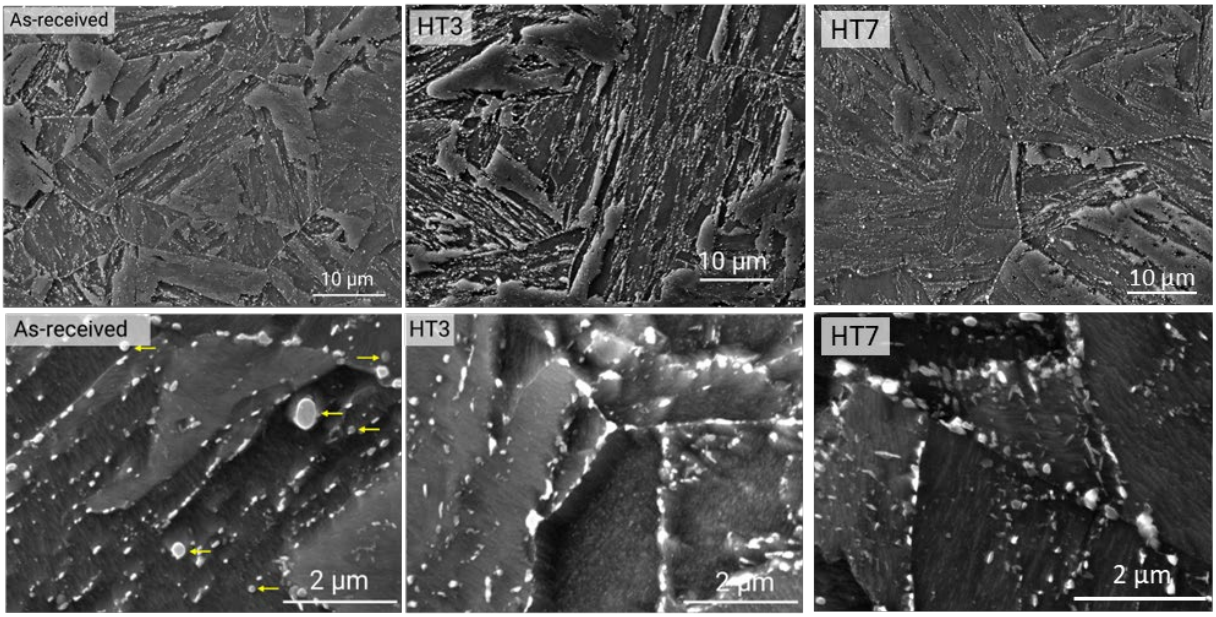

Figure 15. Scanning electron microscopy images of CNAs rods after multiple heat treatments.

2.4.4 FUTURE WORK

Based on the results from different heat treatments on the CNA rods, we chose the HT7 as the optimal heat treatment for CNA rods. Next, we will follow ASME standard to measure tensile, fracture toughness, creep-rupture, low cycle fatigue properties, and weldability. At the same time, we will investigate liquid-metal compatibility and ion/neutron irradiation of the HT7 treated CNA rods.

2.4.5 REFERENCES

[1] Tan, L., T. Graening, X. Hu, W. Zhong, Y. Yang, S. J. Zinkle, and Y. Katoh. "Effects of carbonitrides and carbides on microstructure and properties of castable nanostructured alloys." Journal of Nuclear Materials 540 (2020): 152376.

2.5 DISLOCATION NETWORK WITH SOME DISLOCATION LOOPS IN IRRADIATED MA957 ODS STEEL

A. Bhattacharya (bhattacharya@ornl.gov), S.M. Levine, Y.R. Lin

2.5.1 OBJECTIVE

This task is aimed at quantifying the neutron irradiation induced dislocation loops in ODS alloys. An Fe-14%Cr based MA957 ODS alloy irradiated in HFIR between 5.1 – 8.6 dpa and 335-500 °C was studied. The microstructures were analyzed using scanning transmission electron microscopy (STEM) and diffraction contrast TEM.

2.5.2 SUMMARY

Diffraction contrast TEM and STEM characterization used flashed-polished focused ion beam (FIB)-prepared neutron-irradiated MA957. The results revealed no dramatic changes to the initial dislocation density of the materials due to irradiation. Complex dislocation forest, however, was particularly prominent at 500 °C; at lower temperatures, the net dislocation line density was similar to the nonirradiated condition. Dislocation loops in very low concentration were detected at all irradiation temperatures. The results suggest a lack of dislocation loop formation in ODS MA957 alloys under neutron irradiation which is beneficial to the properties – but previous results showed such materials suffer from severe radiation-enhanced and radiation-induced precipitation of Cr rich α' and NiTi rich phases (likely radiation induced).

2.5.2.1 Progress and Status

HFIR irradiated ODS-MA957 alloy was investigated in this study. The material was irradiated to 5.1, 6, and 8.6 dpa at 335, 450, and 500 °C respectively. Previously, analytical STEM and APT study had revealed radiation-enhanced Cr rich embrittling α' formation and Ni-Ti rich clustering (likely radiation induced) in MA957 [1,2]. Here, focus was on dislocation loop formation. STEM characterization revealed mostly line dislocations and dislocation network in the nonirradiated and irradiated steels, with line dislocation density ranged between ~$1.8x10^{14}$ m^{-2} to ~$51.8x10^{14}$ m^{-2}. The results suggest some minor increase in the line dislocation density. Additionally, dislocation loops were detected in the irradiated alloys with their measured largest diameter in the range of 45-50 nm. However, the number of identified dislocation loops in the samples was very low – as indicated by the red arrows in Figure 16. The results suggest very low formation of dislocation loops in ODS MA957. The studied material was derived from ODS tubes that were in stress-relieved condition with high starting dislocation density. It must be noted that although the alloy showed little change in the overall dislocation line/loop population, this should not be seen as an overall positive behavior. Such alloys, as shown in Refs [1,2], suffer from phase instability under neutron irradiation between 300-500 °C that ultimately dominates the mechanical properties. No cavities were detected in the irradiated sample. Raft formation or clustering of dislocation loops around pre-existing dislocations was not observed, in contrast to results typically reported for ion irradiation at this temperature.

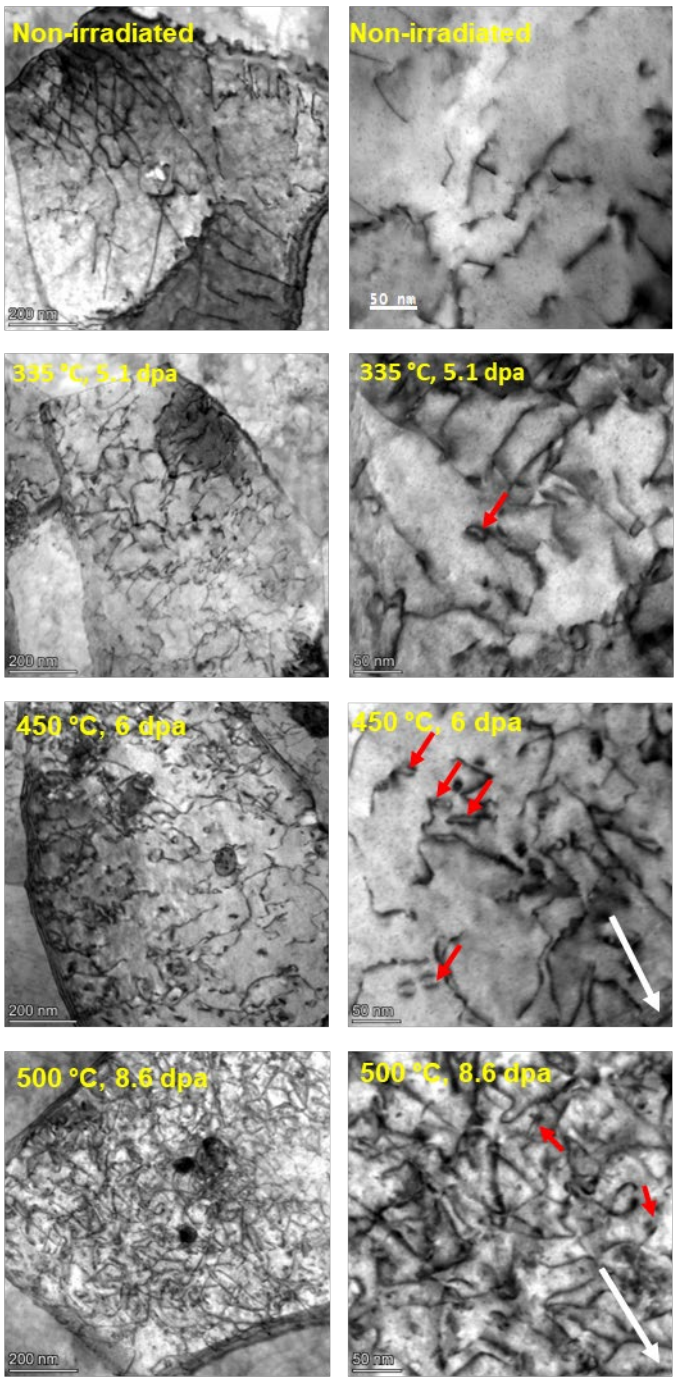

Figure 16. STEM BF images showing the dislocation lines, dislocation loops (indicated using red arrows) and dislocation network in the ODS-MA957 alloy after neutron irradiations in HFIR. The dose and temperatures are overlaid in the images. White arrows indicate the g vectors. Left column provides an overview of the dislocation network in the studied grains while the column on the right provides relatively higher magnifications showing some identified dislocation loops. Imaging performed close to [001] zone axis in all the images.

2.5.3 FUTURE PLANS

Because of small grain sizes (typically around ~700-800 nm), it was challenging to perform any detailed g.b analysis on the dislocation network and on the dislocation loops. In future, g.b analysis will be attempted again on the foils if a double-tile rotation holder becomes available.

2.5.4 REFERENCES:

[1] A. Bhattacharya, S.J. Zinkle, J. Henry, S.M. Levine, P.D. Edmondson, M.R. Gilbert, H. Tanigawa, C.E. Kessel, Irradiation damage concurrent challenges with RAFM and ODS steels for fusion reactor first-wall/blanket: a review, J. Phys. Energy 4 (2022) 034003.

[2] A. Bhattacharya, S.M. Levine, D.T. Hoelzer, J. Poplawsky, J.W. Geringer, Y. Katoh, S.J. Zinkle, Atom probe tomography reveals hardening features in irradiated ODS steels, Fusion Materials Semiannual Progress Report, ORNL/TM-2021/2352.

2.6 DEFORMATION MECHANISMS IN ADDITIVELY MANUFACTURED COMPOSITIONALLY GRADED STEELS

T.S. Byun (byunts@ornl.gov), M.N. Gussev, N. Bibhanshu, T.G. Lach (ORNL)

2.6.1 OBJECTIVE

This research explores an alternative additive manufacturing-based approach for the dissimilar metal joints in the structures of nuclear energy systems. We aimed to understand the microstructure-dependent deformation behavior of an additively manufactured compositionally graded alloy (CGA) whose microstructure transitions from an austenite dominant dual phase structure to a fully ferritic structure.

2.6.2 SUMMARY

The microstructure-dependent deformation behavior was investigated for an additively manufactured compositionally graded alloy (CGA) printed by the laser-directed energy deposition (L-DED) method to explore an alternative approach for fabricating dissimilar metal joints in nuclear energy systems. The electron backscatter diffraction (EBSD) maps display a clear microstructural transition with decreasing austenite-forming elements (Ni and Mn), from the austenite (γ) dominant structures, to complex composite structures containing ferrite (α), martensite (α′), and retained austenite, and then to fully ferritic structures. EBSD data was recorded in-situ during tensile testing in SEM, and the evolution of deformation mechanism and microstructure was characterized using Kikuchi diffraction pattern analysis. The austenite-dominant microstructures showed a complex deformation mechanism of two-step martensitic transformation (γ→ε→α′), whereas the minor austenite phase retained in the ferrite and/or martensite matrix showed a single transformation route (γ→α′).

2.6.3 PROGRESS AND STATUS

The CGA plates with a monotonic compositional change from an austenitic alloy to a low-alloy ferritic steel were printed using the DED process. Two base alloy powders were blended to the desired ratios and fed to the DED printing system to produce the test material plates (16 mm thick × 65 mm high × 50–80 mm wide) with linearly varying composition and constituent phases along the build (Z) direction (and later tensile loading direction). The austenitic (γ-phase) alloy powder was the JAS 2114 powder (Alloy #1: Fe(bal.)-17.1Cr-8.2Ni-7.8Mn-4.2Si) and the ferritic (α-phase) alloy powder was the AISI 8620 low-alloy steel powder (Alloy #8: Fe(bal.)-0.5Cr-0.55Ni-0.8Mn-0.25Si). Prior to the in-situ tensile testing, SS-J2 miniature specimens were mechanically ground and polished following a standard metallographic procedure, with colloidal silica polishing as the final preparation step. Each tensile specimen was tested in the Kammrath and Weiss (K&W) 5 kN tensile stage installed in Tescan Mira3 SEM. All in-situ tests were conducted at a nominal strain rate of 0.001 s^{-1} in vacuum at room temperature, each of which consists of multiple extension-stop cycles (a few to 15 stops). EBSD mapping was performed to display a clear microstructural transition with decreasing austenite-forming elements (Ni and Mn).

As the composition gradually changed with location, the phase constituents and their distribution varied along the build direction accordingly. As summarized in Figure 17, the EBSD-based phase maps clearly show that changing the source powder fraction, and hence modifying the local composition, effectively controls the microstructure of the printed materials. Three different phases were observed over the eight different locations of the build: an FCC austenite (red, with varying grain size), ferrite (green, BCC), and martensite (green BCC/BCT). Note that martensite generally has a body-centered tetragonal (BCT) crystallographic structure, but the two body centered phases, BCT and BCC, formed in low carbon alloys, are not discernable with the current EBSD technique. In detail, the first two alloys, #1 and #2, have dominant austenite phase (matrix phase, red) containing minor ferrite phase (green), which can be named

the austenite-ferrite dual phase alloy. The ferrite contents are about 14% and 9%, respectively, in alloys #1 and #2. It is noted that this minor ferrite phase is a high temperature ferrite and often called the δ-ferrite. In the alloys #3 to #5, the martensite phase with lath structure, mixed with ferrite phase, becomes the major phase constituent, whose content increases from 54% to 95% in #4 and to 100% in #5 with decreasing austenite stabilizing elements (Ni and Mn). Lastly, the last three materials (#6 – #8) are purely ferritic alloys (green phase).

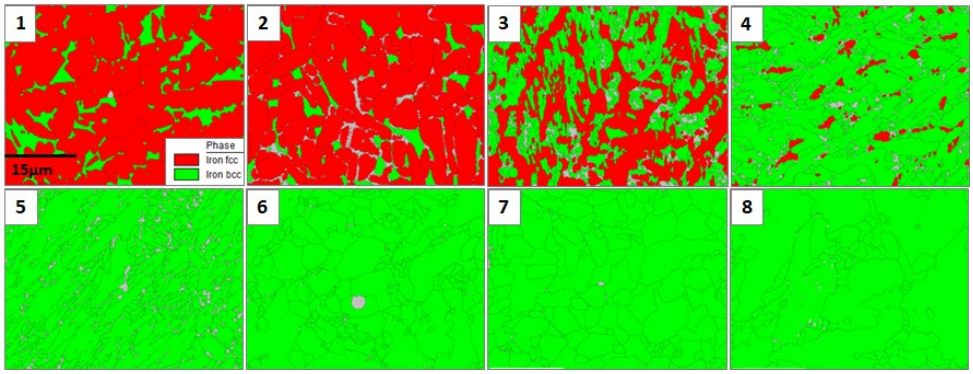

Figure 17. Phase maps for the #1 to #8 alloys of the CGA plate showing a clear transition of phase mixture and grain structure (tensile loading in the horizontal direction or in the build direction).

The engineering tensile properties determined from stress-strain curves are summarized in Table 3. The austenite-ferrite duplex structures have both high strength (YS > 600 MPa; UTS > 1000 MPa) and high ductility (UE and TE > 30%). The alloys with the austenite-martensite duplex or full martensite (with some ferrite) structures, #3 – #5, show very high ultimate strengths but relatively low ductilities. In composition, these alloys are close to the ferritic-martensitic steels that typically require normalization, quenching (martensite formation), and tempering treatments. It is natural that the as-built microstructures with brittle martensite show high strength (UTS > 900 MPa) but low ductility (UE < 12%). The fully ferritic alloys (#6 & #8) have relatively low strength (500 – 600 MPa) and decent ductility (UE = 8 – 16%), except for the #7 showing particularly low ductility (TE < 5%), which might be due to a defect in the gauge portion.

Table 3. Mechanical properties and constituent phases of additively manufactured alloys taken from eight different positions in the build with graded composition.

Position/ Alloy #	Mechanical Properties				Constituent Phases before Deformation
	YS (MPa)	UTS (MPa)	UE (%)	TE (%)	
1	650.9	1106.6	44.5	46.5	Austenite + Ferrite
2	663.9	1055.9	31.6	37.7	Austenite + Ferrite
3	482.8	1465.0	10.2	11.3	Austenite + Martensite
4	979.1	1361.6	3.5	3.6	Austenite + Martensite
5	903.5	950.6	0.5	0.5	Martensite (+ some ferrite)
6	415.2	507.2	8.4	13.0	Ferrite
7	342.7	377.2	1.6	4.5	Ferrite
8	486.0	579.6	15.5	24.1	Ferrite

As seen in Figure 18, the as-printed microstructures of the alloys #1 and #2 are austenite-dominant because they have high austenite stabilization contents such as Ni and Mn. The multi-component austenite (FCC) phase in the alloys #1 and #2, which include a high content (>30 wt.%) of the secondary alloy elements (Cr-Ni-Mn-Si), is usually metastable and has a low stacking fault energy. Such a metastable phase may undergo transformation to more stable phases, such as ε-martensite (HCP) and α′-martensite (BCT/BCC), at the low-test temperature (i.e., room temperature) with the strong mechanical stimulus exerted by tensile loading. These phase transformation (and twinning) mechanisms are highly stress-dependent, and hence those mechanisms are surely enhanced in the as-printed composite structures with relatively high strengths. In the alloy #1, there exist only austenite (red) and ferrite (green) in the as-printed microstructure with 0% plastic strain, but black lines (or needle like features), black areas and yellow areas are already apparent after straining to 7%. The yellow areas are the ε-martensite with HCP structure, while the black features are the crystalline areas that cannot be indexed. These black features, producing weak non-reliable Kikuchi patterns, are heavily deformed crystal spots or α′-martensite areas, both of which have dense dislocations and severe lattice distortion. As the plastic strain increases to 11% and then to 24% in Figure 19(a), the yellow and blackened areas increase further by mostly spreading into the red (austenite) grains. The black features appear within the ferrite (green) and yellow (ε-martensite) phases. It is also observed that the yellow phase (ε-martensite) transforms to the green phase (α′-martensite). Such a gradual growth of α′-martensite into ε-martensite area indicates the HCP phase can retransform into more stable α′-martensite with increasing strain level. Figure 18(b) demonstrates the same deformation process with phase transformation mechanisms up to a higher strain of 31%.

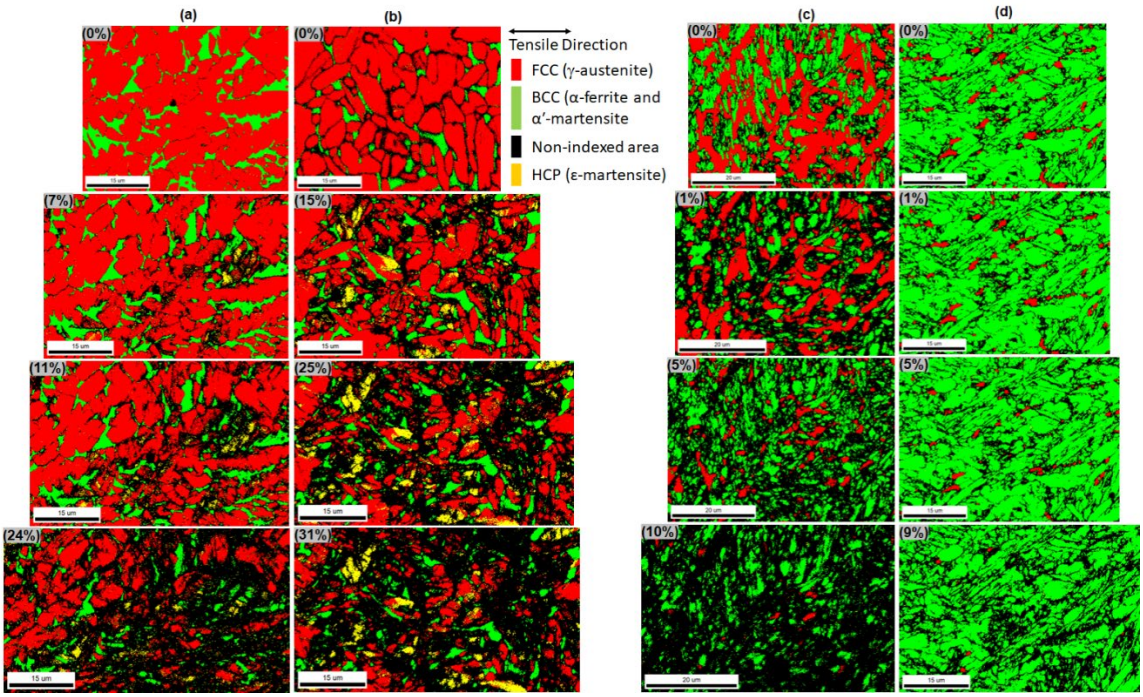

Figure 18. EBSD phase maps showing deformation induced phase transformations in the austenite dominant alloys, (a) and (b), and martensite dominant alloys, (c) and (d).

The alloys #3 through #5 include medium-level amounts of Cr-Ni-Mn-Si content (17 – 27%) among the eight alloys and their major constituents are martensite (α′) and ferrite (α) phases (54 – 100%). In these alloys the plastic deformation is primarily a combined process of the martensitic transformation of retained austenite phase (γ→α′ transformation) and typical dislocation glide. The high strength, but low ductility, of these alloys should be the key evidence for containment of α′-martensite in their microstructures. Stress should be a strong stimulus for the deformation-induced martensitic transformation in the structures with retained austenite. As displayed in Figure 18(c) and 18(d), therefore, the austenite phase disappeared quickly with increasing strain (and stress) to the near uniform deformation limits of 10% and 9%, respectively, for the two alloys. In detail, the column 2(c) for alloy # 3 shows that during tensile loading to the high stresses of ~1200 MPa (at 5% strain) and ~1400 MPa (at 10% strain), the γ→α′ transformation occurs very quickly by consuming the relatively small amount of retained austenite, leaving less than 2% austenite after 10% strain. It is interesting that no transformation to HCP phase is detected in the deformation process, although the content of secondary elements (Cr-Ni-Mn-Si) is still high (e.g., 28% for the alloy #3 versus 32% for the alloy #2). The column 2(d) for alloy #4 included relatively small amount of austenite (~5%) and the martensitic transformation occurred at a much slower rate. The volume fraction of the FCC phase (γ) decreased to ~3.7%, 1.9%, and <0.5% as the phase is deformed by 1%, 5%, and 9% strains, respectively. Again, no sign of ε-martensite was detected up the highest strain level examined.

Deformation behavior in the ferrite-only microstructures is rather simple when compared to those of the high-Cr compositions with austenite. All the ferrite alloys #6, #7, and #8 showed very similar behavior in EBSD data, without showing any phase transformation, indicating dislocation glide and severe grain deformation/distortion activities. A representative deformation behavior in the ferrite only alloys is summarized in Figure 19, where the IPF (left column) and IQ (right column) EBSD maps for a ferrite specimen (#6) are displayed before deformation (0%) and after deformation to the plastic strains of 7% and 10%. A few discernable phenomena have developed in these ferritic alloys with increasing strain level: grain rotation towards [110]-corner of unit triangle (with respect to the tensile direction), accumulation of

more geometrically necessary dislocations (GNDs) (indicated in color variation evolution in the IPF maps), and grain distortion by local straining and constraints after deformation.

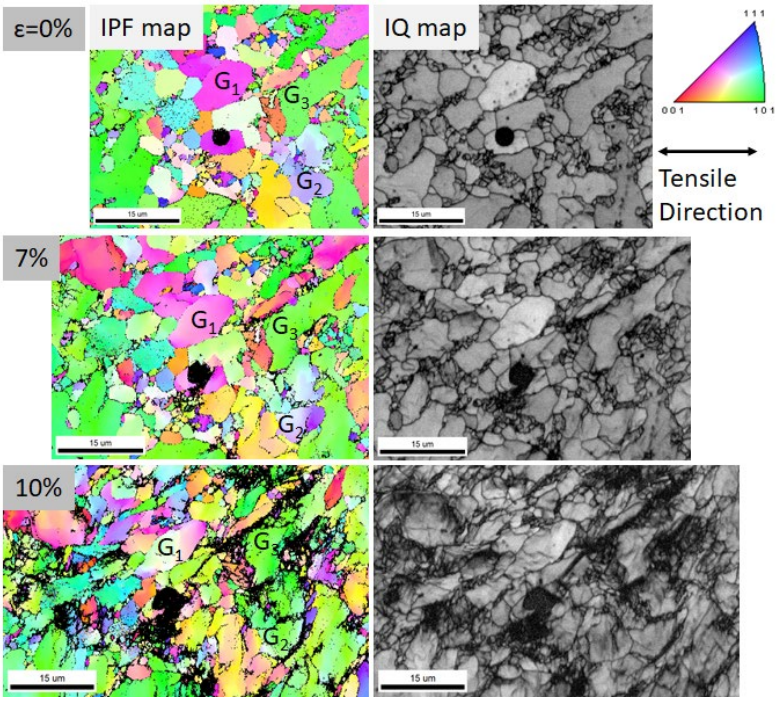

Figure 19. IPF and IQ EBSD maps recorded at different steps (0, 7, and 10% plastic strains) for a ferrite specimen (#6). Note that the black round feature near the center of each image is a non-metallic inclusion (most likely an oxide) that does not show visible Kikuchi pattern. G_1-G_2: grains showing strain-induced lattice rotation, G_3: grain with stable orientation.

2.6.4 FUTURE WORK

This exploratory research provides some key fundamental understanding of the deformation behavior of AM CGA under tensile load, which can guide us to define obstacles to using the AM technology for joining dissimilar materials and to resolve those by developing proper alloy combinations and post-build thermomechanical treatments.

2.7 PROCESS DEVELOPMENT FOR LOW-COST ODS ALLOYS

T.S. Byun (byunts@ornl.gov), D.T. Hoelzer, T.G. Lach, D.A. Collins (ORNL)

2.7.1 OBJECTIVE

This research is to develop an economically attractive, technically feasible processing route for oxide dispersion strengthened (ODS) ferritic alloys for fusion reactor structural components. Various processing routes were applied and evaluated to achieve desirable mechanical properties.

2.7.2 SUMMARY

Production of ODS steels was attempted via new processing routes different from the traditional mechanical alloying process. Continuous application of high-temperature rolling is the key process used in this alloy development since a high-temperature mechanical processing (extrusion, rolling, or forging) is one of the most effective methods to refine microstructures and redistribute alloying elements. Alloys with high oxygen contents were produced via two different routes using powder mixtures: thermomechanical consolidation and vacuum arc melting followed by rapid solidification. Various thermomechanical processes have been applied to the consolidated or solidified alloys to produce fine grain structures and dispersions of oxide particles. Tensile strength and ductility parameters were used to screen the processing routes and down-select materials for further studies. Tensile testing over a wide temperature range of room temperature to 700 °C and microstructural characterization using SEM and TEM were performed for a few selected materials. Some newly produced ODS alloys demonstrated desirable mechanical properties, such as high strength and ductility, although the distribution of oxide particles and other precipitates require further improvement.

2.7.3 PROGRESS AND STATUS

For the fiscal year, twenty (20) different ODS alloy versions have been produced by combining different alloy and oxide powders and applying various thermomechanical treatments (TMTs) and melting process, and majority of the products were evaluated with tensile testing. A set of powder mixtures were prepared for the production of solid materials. As listed in Table 4, three alloy powders (14 YWT base alloy, 14YWT alloy doped with yttrium and oxygen, and 10YWT base alloy) and two oxide powders (Fe_2O_3 and Y_2O_3) were combined to make various mixtures with enough yttrium and oxygen contents to have at least 0.3 wt.% of O and Y rich oxide particles in the products. As listed in the table, HR-1 through HR-4 define the contents of the powder mixtures: O and Y doped 14YWT (HR-1), 14YWT mixed with iron oxide (HR-2), 14YWT mixed with yttrium oxide (HR-3), and 10YWT mixed with yttrium oxide (HR-4).

Consolidation of the O and Y doped alloy powder and alloy-oxide powder mixtures was made through the high temperature rolling (HR) after annealing at 1200 °C or 900 °C for 30 minutes to designated thickness reductions. The powder mixtures were compacted into stainless steel containers before the HRs were applied. Multiple HRs were applied to the container until enough thickness reduction is achieved for near complete consolidation (strain > 50%). Two consolidated materials (see HR-1Ma and HR-2Ma) were supplied to the remelting-solidification process in a vacuum furnace, where the melt was poured into a small copper crucible to increase sonification rate. Two small ingots with diameters of about 9 mm and 6 mm were produced for each material and examined with and without further thermomechanical treatment.

Other consolidated ODS alloys were exposed to different thermomechanical processes, each of which consisted of multiple HR steps at one or two temperatures. These continuous (repeated) thermomechanical activation processes were applied to achieve different degrees of microstructure refinement and element redistribution to the consolidated ODS steels with the enhanced thermal activation with stress and

dislocations. Table 4 also shows the total strains applied by consolidation and continuous TMTs were up to 310%, which is a severe plasticity. The annealing time in each HR was 10 minutes.

Table 4. Summary of base materials, processing steps, and testing status for the ODS alloys.

Process ID	Base Materials (Alloy and Oxide Powders)	Consolidation Process (Strain)	Continuous TMT (Total Strain)	Screening Test
HR-1 HR-2	14YWT alloy (with Y, O) 14YWT base+Fe_2O_3	6 x HR at 900°C (80%)	9 x HR at 900 °C (310%)	Tensile Properties
HR-1a HR-2a HR-3	14YWT alloy (with Y, O) 14YWT base+Fe_2O_3 14YWT base+Y_2O_3	6 x HR at 900°C (80%)	8 x HR at 700 °C (240%)	Tensile Properties
HR-1b HR-2b HR-3a	14YWT alloy (with Y, O) 14YWT base+Fe_2O_3 14YWT base+Y_2O_3	6 x HR at 900°C (80%)	8 x HR at 550 °C (240%)	Tensile Properties
HR-2c HR-2d HR-4	14YWT base+Fe_2O_3 14YWT base+Fe_2O_3 10YWT base+Y_2O_3	4 x HR at 1200°C (60%)	8 x HR at 600 °C (220%)	Tensile Properties
HR-4a	10YWT base+Y_2O_3	4 x HR at 900°C (70%)	8 x HR at 600 °C (220%)	Tensile Properties
HR-1cc	14YWT alloy (with Y, O) 14YWT base+Fe_2O_3	6 x HR at 900°C (80%)		Tensile Properties
HR-2cc	14YWT alloy (with Y, O) 14YWT base+Fe_2O_3	6 x HR at 900°C (80%)		Tensile Properties
HR-2cd HR-2dd	14YWT base+Fe2O3 14YWT base+Fe2O3	6 x HR at 900°C (80%)	3 x HR at 700 °C & 3 x HR at 500 °C (270%)	Test in progress
HR-4c	10YWT base+Y2O3	4 x HR at 1200°C (60%)		Test in progress
HR-4ac	10YWT base+Y2O3	4 x HR at 900°C (60%)		Test in progress
HR-1Ma	14YWT alloy (with Y, O)	Vacuum Arc Melting in Cu crucible	6 x HR at 600 °C (150%)	Test in progress
HR-2Ma	14YWT base+Fe2O3	Vacuum Arc Melting in Cu crucible		Test in progress

Tensile ductility and strength are used as screening parameters for the processing routes tested in the research. Figure 20 compares the yield and ultimate strengths (YS and UTS) and uniform and total elongations (UE and TE) for the processed materials. The strength of the TMT processed ODS alloys is highly dependent on the processing routes. Two combinations of consolidation and continuous thermomechanical processes, HR-2 (900 °C/600 °C) and HR-3 (900 °C/600 °C), demonstrate high strengths: YS > 800 MPa and UTS > 1 GPa, which fall within the strength range of some ODS steels. The tensile property dataset also indicates that the highest temperature consolidation (at 1200 °C) and continuous TMT (at 900 °C) result in relatively low strengths, which might be due to over-coarsening of grains and precipitates.

The TMT processed materials demonstrate overall significant ductilities for the measured strengths: no prompt necking (i.e., zero UE) is observed among the materials displayed in the figure. It is notable that the two highest strength materials show good uniform ductility of ~5% or higher.

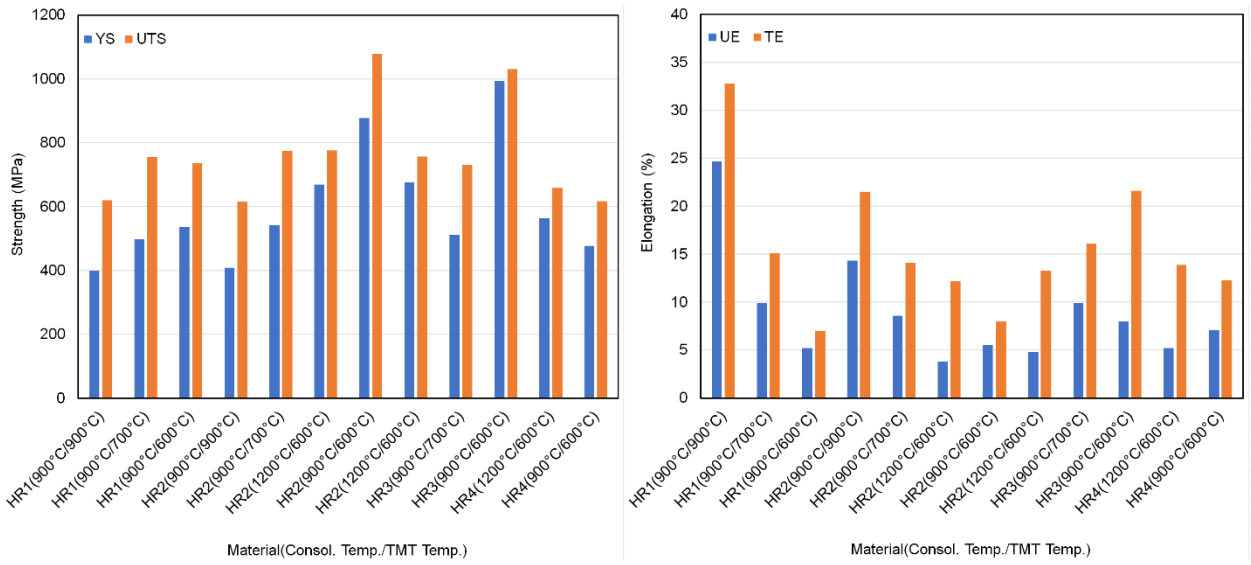

Figure 20. Summary of tensile strength (left) and ductility (right) for the ODS materials newly processed and evaluated.

Microstructure analyses to characterize grain structures and particle distributions were performed using SEM-EBSD and STEM for a selected set of materials that demonstrate desirable properties. The elemental maps in Figure 21 for one of the high strength materials, HR-2 (900 °C/600 °C), show a highly inhomogeneous distribution of precipitate particles, a mixture of Y-O (oxide) particles, Ti-C (carbide) particles, and minor W-rich particles next to the surface of Ti-C particles, Figure 21. The oxide particles have a wide size distribution of a few to ~50 nm, and carbide particles are in ~20-50 nm, some of which have high aspect ratios probably due to shearing and elongation during rolling. The pinkish curved lines seen in both maps indicate tungsten has segregated to grain boundaries.

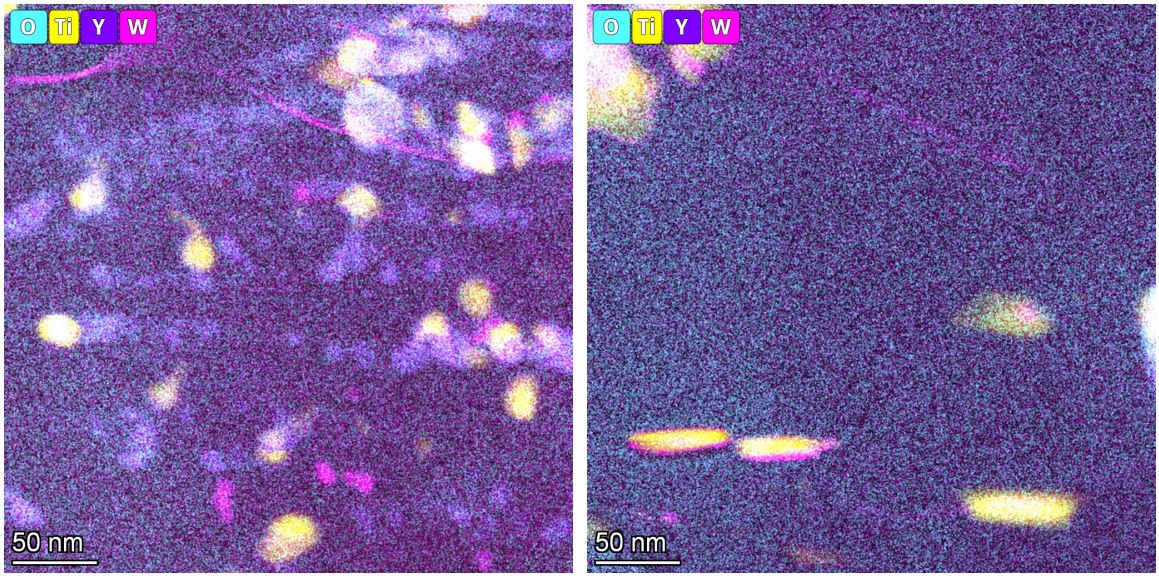

Figure 21. Elemental maps from STEM showing relatively high density (left) and low density (right) areas. The nanoparticles seen on the maps are Y-O (light purple), Ti-C (yellow), and W-rich (pink).

2.7.4 FUTURE WORK

Additional processing routes will be tested to achieve ODS alloys with higher strengths but maintaining adequate ductility (more than a few percent). High resolution microscopy is also pursued for the materials with high strength and ductility. Using the key mechanical property data (ductility, strength, fracture toughness) and microstructure characteristics, processing routes will be selected for further research such as irradiation effects experiments and larger scale production. The roles of plasticity in oxide particle distribution and grain refinement will be also further studied.

2.8 IN-SITU IRRADIATIONS SHOW THAT MX PARTICLES IN FM STEELS ARE AMORPHIZATION RESISTANT

A. Bhattacharya, S.M. Levine, S.J. Zinkle. W.-Y. Chen (ANL), P. Baldo (ANL), C.M. Parish, P.D. Edmondson

2.8.1 OBJECTIVE

MX carbonitrides in RAFM and conventional FM steels ultimately control the high-temperature properties, so a fundamental understanding of their tolerance to irradiation is important. Here, in-situ irradiations were used to understand tolerance of MX precipitates to radiation induced amorphization and compared to $M_{23}C_6$ carbides data reported separately. The study was performed on an additively manufactured 9%Cr-1%MoVNb (Grade91) steel using the extraction replica technique.

2.8.2 SUMMARY

Similar to an accompanying report and details published in Ref. [1], in-situ irradiation experiments were performed using the IVEM facility at Argonne National Lab. The experiments were performed on extraction replica samples from an additively manufactured 9Cr-1MoVNb steel using 1 MeV Kr^{2+} ions, inside a transmission electron microscope. The irradiations were performed at relatively low temperatures of 100 and 293 K where amorphization susceptibility of nonmetallic phases is typically higher than at higher temperatures [2]. The experiments were performed up to a maximum dose of ~2.4 displacements per atom (dpa). The study showed no evidence of amorphization of MX carbonitrides for doses as high as ~2 dpa and for temperatures as low as 100 K. This highlights the good irradiation tolerance of the MX type particles with strong resistance to radiation induced amorphization (RIA). This is in contrast to $M_{23}C_6$ carbides, where similar experiments show RIA for one-tenth of the maximum doses explored in this present study. The results are consistent with previous data on RIA studies of MX and further highlights the need to maximize MX fraction and minimize $M_{23}C_6$ fraction in steels for irradiation service.

2.8.3 PROGRESS AND STATUS

The MX nanoprecipitates, which were primarily V-rich carbonitrides, were studied in the AM 9Cr-1MoVNb steel after irradiations at 100 and 293 K. Figure 22 shows an overview of the precipitate distribution in this alloy recorded by analytical STEM on the extraction replica sample. Up to ~2 dpa, the MX phase remained crystalline with no sign of amorphization. This is visible in conventional bright field (BF) TEM images and the associated nanobeam diffraction (NBD) patterns in Figure 23, where fully amorphous rings were detected for $M_{23}C_6$ carbides while strong diffraction spots are indexed for the MX particles after ~2 dpa. The lack of amorphization of MX can also be inferred from the relatively strong diffraction contrast visible in these particles as compared to a flat, uniform amorphous contrast of the nearby $M_{23}C_6$ carbides.

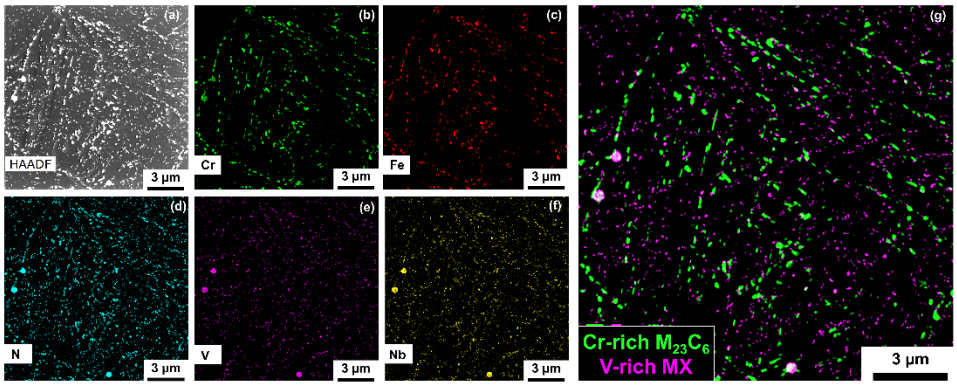

Figure 22. Cr rich M23C6 and V rich MX precipitates in AM-Grade91 steel detected by STEM-EDX on extraction replicas. (a) high angle annular dark field (HAADF) image of nanoprecipitates, (b–f) STEM-EDX elemental quant maps of nanoprecipitate chemistries, (g) Cr and V EDX maps overlaid to show M23C6 and MX precipitates. Dwell time/pixel = 90 µs.

Many MX particles in this steel were large (up to ~150-200 nm) and almost equivalent in size to the $M_{23}C_6$ particles. This is visible in Figure 23b where the highlighted MX particle is almost similar in size to $M_{23}C_6$ in the main TEM image. Therefore, the difference in the amorphization behavior is likely not due to any size difference but reflects the inherent radiation tolerance of MX type particles. Figure 22a- Figure 22b show some structural damage contrast inside the MX particles, most likely extended defects and/or black dot defect structures. At present, a fundamental reason to explain the lack of amorphization in MX compared to $M_{23}C_6$ is unavailable and more dedicated research is needed to identify the key underlying mechanisms that control the behavior of MX under irradiation.

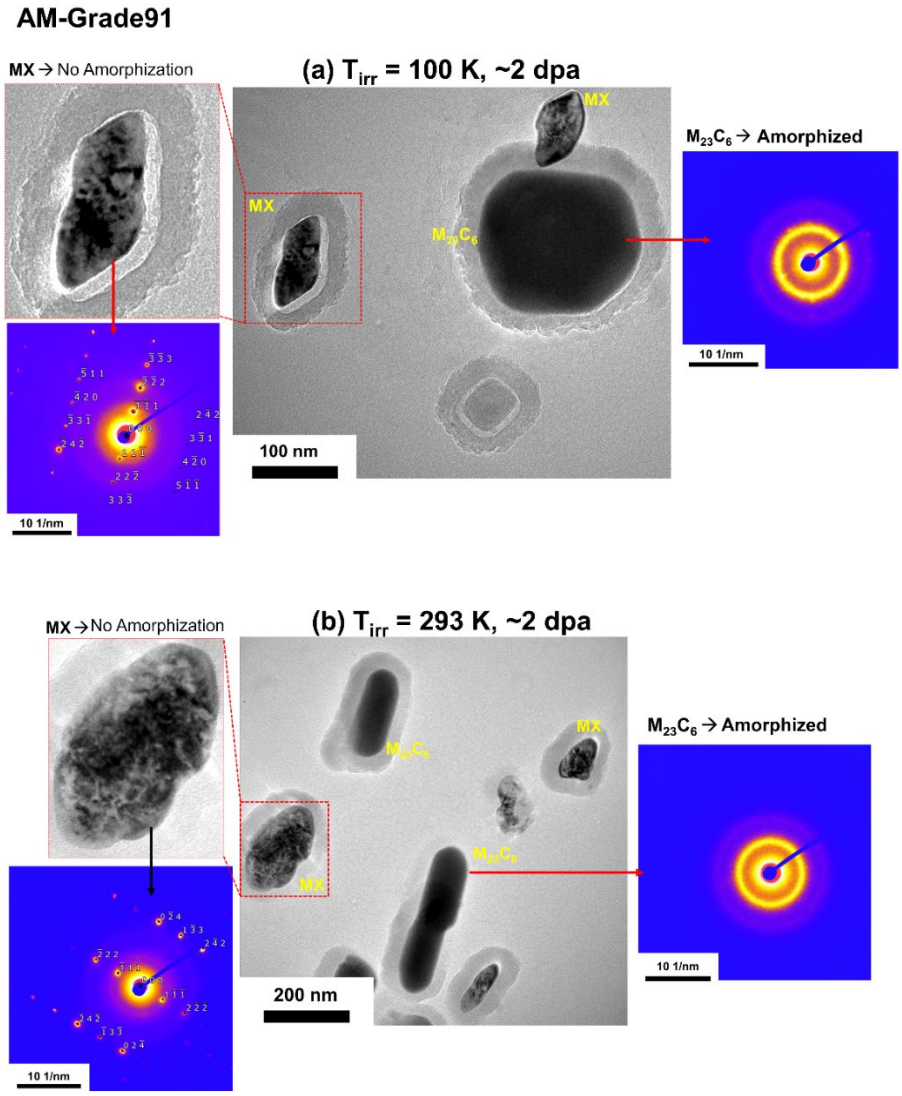

Figure 23. BF TEM images and indexed diffraction patterns comparing MX and $M_{23}C_6$particles after ~2 dpa irradiations on extraction replicas at (a) 100 K and (b) 293 K. The diffraction ring patterns from fully amorphized $M_{23}C_6$ and spot patterns from crystalline MX particles indexed are presented. Some other MX and $M_{23}C_6$ particles are highlighted in the TEM image where contrast difference between MX and amorphous $M_{23}C_6$ can be seen. Diffraction patterns indexed using SingleCrystal™ software.

It should be noted that to track amorphization with ion dose in this study, the experiments were stop-start in nature with periodic recording of the diffraction patterns to observe evidence of amorphous rings. During the experiments, the electron beam was switched off to avoid any deleterious artifacts due to high electron energy deposition from the 200 keV electrons on the amorphization behavior of the nonmetallic particles.

2.8.4 FUTURE RESEARCH

This study is complete with a publication [1]. The results are currently being compared to FM and RAFM steels following HFIR neutron irradiations.

2.8.5 REFERENCES:

[1] A. Bhattacharya, S.M. Levine, S.J. Zinkle. W.-Y. Chen, P. Baldo, C.M. Parish, P.D. Edmondson, Radiation induced amorphization of carbides in additively manufactured and conventional ferritic-martensitic steels: *In-situ* experiments on extraction replicas, J. Nucl. Mater. 563 (2022) 153646.

[2] W.J. Weber, R.C. Ewing, C.R.A. Catlow, T. Diaz De La Rubia, L.W. Hobbs, C. Ki- noshita, H. Matzke, A.T. Motta, M. Nastasi, E.K.H. Salje, E.R. Vance, S.J. Zinkle, Radiation effects in crystalline ceramics for the immobilization of high-level nuclear waste and plutonium, J. Mater. Res. 13 (1998) 1434–1484

2.9 INFUSE − CHARACTERIZATION AND QUALIFICATION OF JK2LB ALLOY FOR ADDITIVE MANUFACTURING OF FUSION COMPONENTS

X. Chen (chenx2@ornl.gov), N. Russell, R. Volberg (Type One Energy), W. Zhong, Y. Yang, Y. Katoh

2.9.1 OBJECTIVE

The application of additive manufacturing (AM) for building complex fusion components may enable substantial savings in cost and time and a wider design envelope compared to conventional fabrication methods. However, additively manufactured materials may exhibit different microstructure features compared to their counterparts made by conventional manufacturing methods. A critical concern for the AM technique is how the AM material behaves in a fusion environment. A nuclear-rated alloy of interest for AM qualification is JK2LB, a Japanese high manganese austenitic stainless steel designed for fusion components, e.g. ITER central solenoid. JK2LB has high tensile strength, high ductility, and high resistance to fatigue at cryogenic temperatures. In addition, the material has a low Ni content so that it decays to safe radioactivity levels below the IAEA clearance limit in a much shorter time compared with conventional austenitic stainless steels containing high Ni content. The project is qualifying AM JK2LB for fusion applications by performing neutron irradiation in the High Flux Isotope Reactor (HFIR) at Oak Ridge National Laboratory (ORNL) and the following post-irradiation evaluation in the hot cells and possibly the Low Activation Materials Development and Analysis (LAMDA) facilities.

2.9.2 SUMMARY

The project aims for neutron irradiation and the following characterization of the mechanical properties and microstructures of AM JK2LB, a Japanese high manganese austenitic stainless steel designed for fusion applications. To date, we have completed the rabbit capsule design and parts ordering for two rabbit capsules for irradiating SS-J3 tensile specimens at 80 °C to 5 dpa (displacements per atom) and at 300 °C to 5 dpa. Our INFUSE partner, Type One Energy, has finalized the material matrix for irradiation with us and is currently performing additive manufacturing of JK2LB specimens for irradiation and additional characterization.

2.9.3 PROGRESS AND STATUS

We adopted two rabbit capsule designs shown in Figure 24 and Figure 25 for the 300 °C and 80 °C irradiations, respectively. The 300 °C GENTEN design has been used in various irradiation campaigns and it relies on gamma heating and gas gap control for controlling the irradiation temperature. The rabbit can accommodate 24 SS-J3 specimens in total. More details for this design can be found in Ref. [1]. The 80 °C perforated rabbit capsule design is a relatively new design adopted from the irradiation campaign for SHINE Technologies. Since the specimens are in direct contact with the reactor coolant, the irradiation temperature is similar to the average coolant temperature of HFIR at 80 °C. The perforated rabbit capsule design allows 30 SS-J3 specimens to be irradiated.

To fully utilize the available irradiation space, we designed the materials irradiation matrix shown in Table 5. Besides the AM JK2LB, we also include the baseline wrought JK2LB for comparing material properties differences due to the AM process. In addition, we will evaluate AM JK2LB with 3.3 wt% of Y_2O_3 for additional oxide dispersion strengthening. Lastly, we will include the castable nanostructured alloy (CNA), an advanced reduced activation ferritic-martensitic steel developed at ORNL, for irradiation because limited post-irradiation mechanical properties are available for this material.

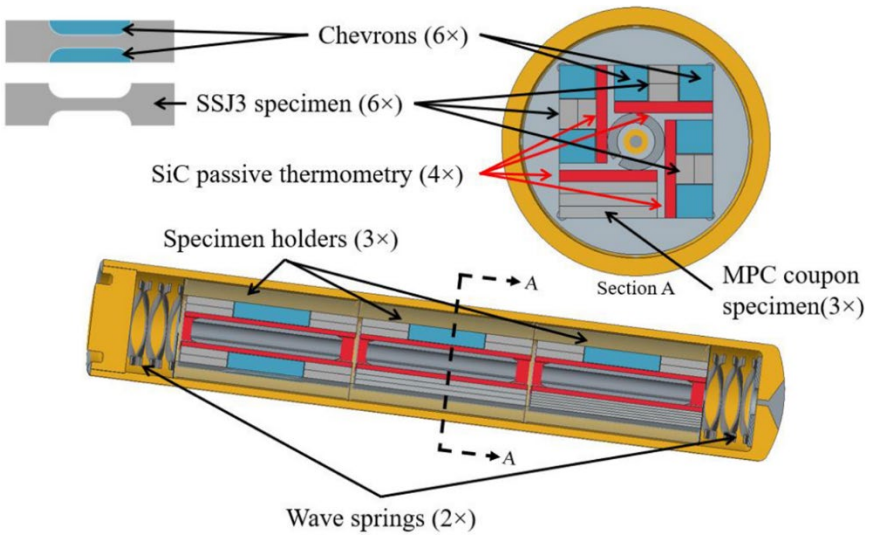

Figure 24. 300 °C GENTEN rabbit capsule design [1].

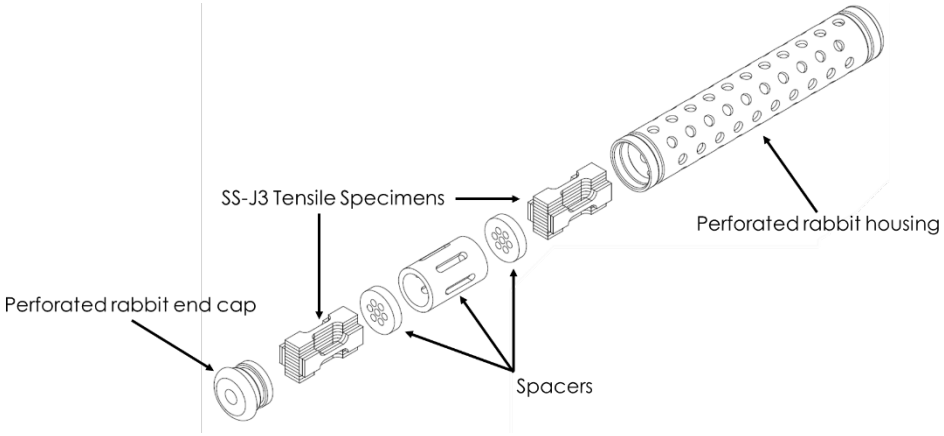

Figure 25. 80 °C perforated rabbit capsule design.

Table 5. Materials irradiation matrix.

Irradiation temperature (°C)	Number of SS-J3 specimens from different types of materials			
	ORNL CNA	JK2LB	AM-JK2LB	AM-JK2LB-Y_2O_3
80	3	3	11-12	11-12
300	6	2	8	8

2.9.4 FUTURE WORK

Our INFUSE partner Type One Energy is currently performing additive manufacturing of JK2LB specimens for irradiation and additional characterization. Once we receive AM SS-J3 specimens from Type One Energy, we will start HFIR irradiation preparation. We anticipate the irradiation would start in Spring 2023.

2.9.5 REFERENCES

[1] R.H. Howard, K.R. Smith, "Development of a Flexible Design for Irradiation of Miniature Tensile and Charpy Test Specimens in the High Flux Isotope Reactor", ORNL/TM-2018/872, 2018, doi:10.2172/1460197

2.10 QUANTIFICATION OF IRRADIATION HARDENING AND LOSS OF DUCTILITY IN HFIR IRRADIATED F82H AND ISOTOPICALLY TAILORED F82H

A. Bhattacharya, S.J. Zinkle, J.W. Geringer, J. Reed, D. Hamaguchi (QST), T. Nozawa (QST), H. Tanigawa (QST)

2.10.1 OBJECTIVE

Mechanical property testing was completed in the hot cells on HFIR irradiated F82H-IEA and F82H-mod3 isotopically-tailored F82H steels. The effect of neutron dose up to ~86 dpa at 300 °C on irradiation hardening and loss of ductility was quantified for F82H-IEA and mod3 variants. The isotopically tailored steel, which leveraged parallel activities in the fusion LDRD project at ORNL, compared ^{58}Ni- and ^{60}Ni-isotopically tailored F82H to quantify the effect of He on hardening and loss of ductility at high doses (>70-80 dpa). The results from uniaxial tension tests are compiled. The irradiation experiments used SS-J3 type flat tensile samples.

2.10.2 SUMMARY

Tensile tests were completed on F82H-IEA, F82H-mod3, (1.4% ^{58}Ni)-F82H, and (1.4% ^{60}Ni)-F82H that were irradiated in HFIR in different irradiation experiments in QST collaboration, such as F8B1, F8B2, RB15J and JP29 irradiation experiments (maximum dose ranging from 76.7 to ~86.2 dpa, T_{irr} = 300±30 °C). The results from F82H-IEA show significant irradiation hardening, with severe loss in tensile elongation; however, the overall properties are similar to typical RAFM steel behavior with hardening saturation around ~20 dpa. A comparison of ^{58}Ni- and ^{60}Ni-F82H quantified the effect of helium on hardness and tensile properties. The 1.4% ^{58}Ni-F82H produced ~936 appm He (~11 appm He/dpa) while 1.4% ^{60}Ni-F82H produced ~26 appm He (~0.3 appm He/dpa) for doses up to 86.2 dpa. The results highlight that while there is indeed additional hardening due to He generation, the extent of additional hardening under HFIR relevant conditions is in the range of ~100-160 MPa for doses >75-80 dpa at 300 °C. The effect of He on uniform plastic elongation (UEp) appears insignificant. However, there is a further reduction in total plastic elongation (TEp) due to He generation for doses >80 dpa. The TEp generally stayed above 5% for most of the tested conditions.

2.10.3 PROGRESS AND STATUS

F82H-IEA, 1.4%^{58}Ni-F82H, and 1.4%^{60}Ni-F82H were neutron irradiated in the JP29 experiment in HFIR to doses between ~76.7-86 dpa at 300 °C. Irradiated uniaxial tensile properties are summarized. Uniaxial tensile tests were performed in the hot cells at RT and 300 °C with guidance from ASTM E8 Standard Test Methods for Tension Testing of Metallic Materials and ASTM E21 Standard Test Methods for Elevated Temperature Tension Tests of Metallic Materials using a strain rate of 10^{-3} s^{-1} (5×10^{-3} mm/s extension rate). The tangent modulus method was used to provide values for the yield strength (σ_{YS}), ultimate tensile strength (σ_{UTS}), uniform plastic elongation (UEp) and total plastic elongation (TEp) in the absence of gauge extensometry for miniature tensile samples. The specimens were shoulder-loaded for testing using an Instron 5967 tensile machine equipped with a 5 kN load cell and connected with an Instron Bluehill3 analysis software. RT tests were performed in air. Elevated temperature tests were performed in vacuum at pressures $\leq5\times10^{-6}$ torr. For tensile tests at 300 °C, the temperatures were measured using two thermocouples welded onto the fixture. The temperature ramp-up time from room to test temperature was typically between ~25–30 min. The tests were performed only when the sample temperature stabilized to the setpoint of 300±5 °C.

2.10.4 COMPARING DOSE DEPENDENT IRRADIATION HARDENING AND LOSS OF DUCTILITY IN THE DIFFERENT ALLOYS

A compilation of the dose-dependent σ_{YS} of HFIR irradiated F82H variants is presented in Figure 26. For F82H-IEA, results show a sharp increase in irradiation hardening at low doses (<10 dpa), and saturated hardening occurring around ~20 dpa. At high doses (>70 dpa), F82H-IEA and mod-3 variants behave almost in an identical manner. These alloys lose their ductility very sharply with dose. The UEp drops very rapidly to values lower than ~0.5% for doses less than 3-5 dpa. Thereafter, the UEp saturates at such low values for doses as high as >80 dpa. The TEp also sharply drops, but overall stays above 5% at the highest studied dose. The results confirm that the primary ductility remaining in this class of materials post-irradiation is necking ductility, with practically no UEp. The results from 76.7-86.2 dpa irradiated ^{58}Ni-F82H/^{60}Ni-F82H are overlaid in the same figures. There is additional hardening in ^{58}Ni-F82H (~936 appm He) as compared to ^{60}Ni-F82H (~26 appm He). This additional hardening is attributed to the effect of high He content in ^{58}Ni- samples as compared to ^{60}Ni-doped samples. However, this additional increase in σ_{YS} is not as high as reported from STIP results in conventional FM and RAFM steels [2]. Figure 27 presents the dose dependent loss in UEp and TEp of the Ni doped alloys. It is evident that He seems to have negligible effect on UEp for doses as high as >80 dpa. This is unsurprising because RAFM steels like F82H already have very little UEp after neutron irradiation in the absence of He (less than 0.5% typically), so margin to further lose UEp by He addition will be small. But He does deleteriously affect TEp, likely due to the additional hardening introduced by He-induced cavities/bubbles in the microstructure that will act as obstacles to the dislocation motion. Because of the extremely low UEp remaining in the steel variants, the strain hardening figure of merit (σ_{UTS}/σ_{YS}) in all the tested materials is generally very low.

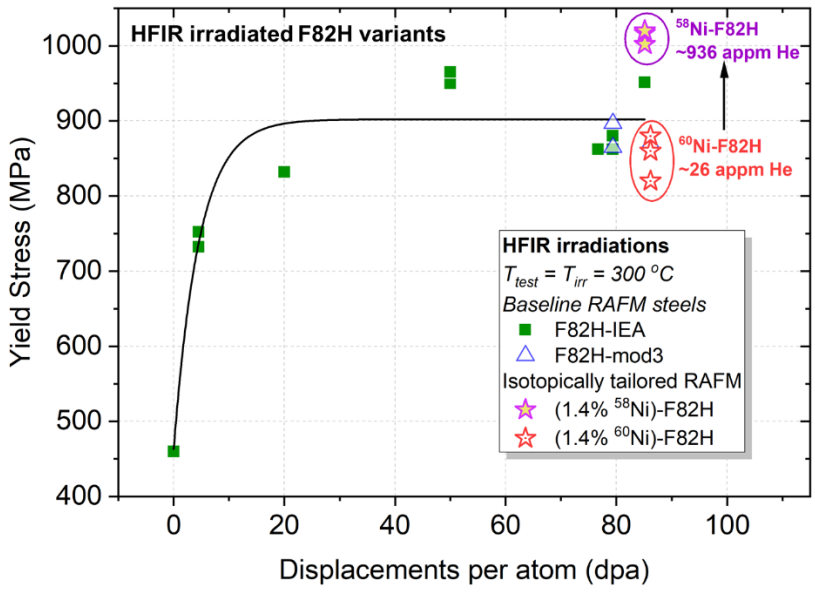

Figure 26. Dose dependent yield stress in F82H steel variants (IEA, mod3), compared with 1.4% ^{58}Ni-F82H and ^{60}Ni-F82H isotopically tailored steels that were irradiated at ORNL in HFIR.

There is a non-negligible effect of test temperature on measured irradiation hardening, as visible in Figure 28. The additional hardening because of He was estimated to be ~101 MPa for tests performed at RT versus ~160 MPa when tests were performed at 300 °C. The effect of tensile test temperature on measured

irradiation hardening has been recently further highlighted by Bhattacharya et al. [1], and together with the present results shows that irradiation hardening should not be assumed constant with test temperature in this class of materials.

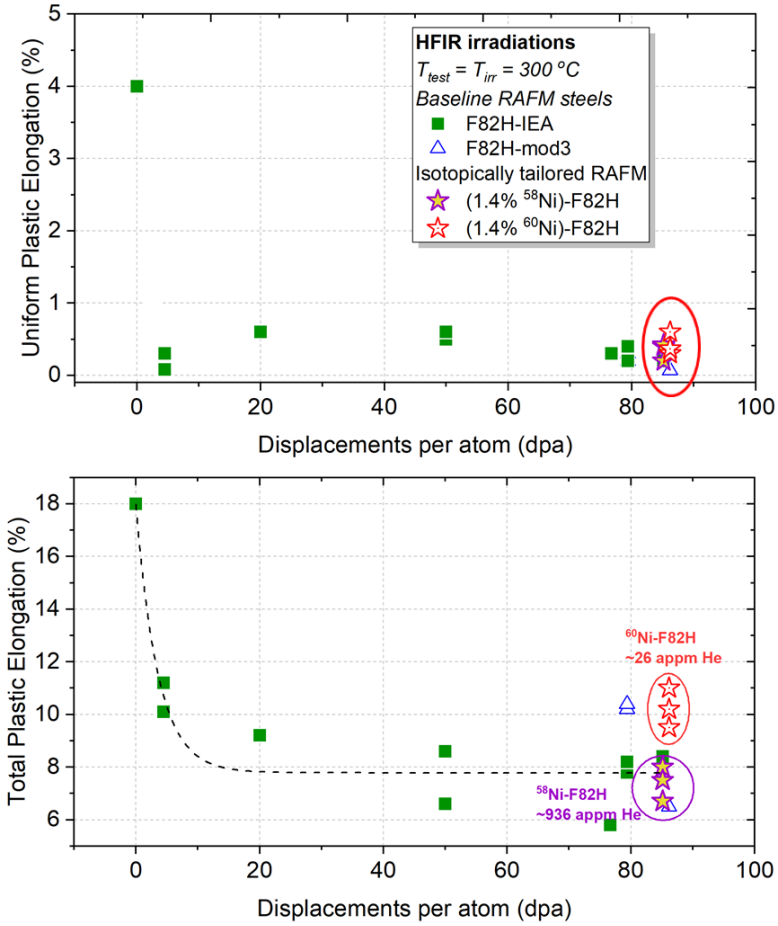

Figure 27. Dose dependent reduction in uniform and total plastic elongations in F82H variants compared with high dose data on 1.4% ^{58}Ni-F82H and ^{60}Ni-F82H isotopically tailored steels.

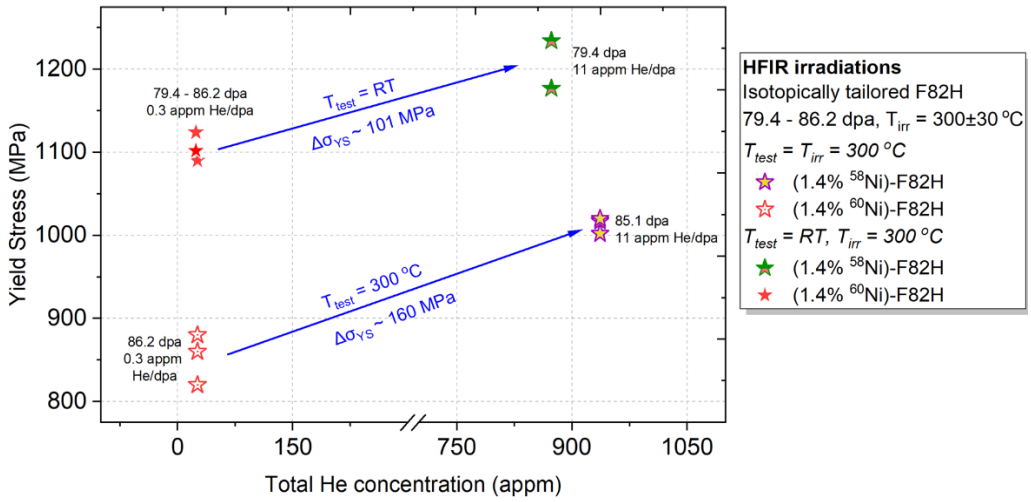

Figure 28. The effect of tensile test temperature on measured irradiation hardening in HFIR irradiated 1.4% ^{58}Ni-F82H and ^{60}Ni-F82H isotopically tailored steels.

2.10.5 FUTURE RESEARCH

STEM and APT investigation of the F82H variants included the Ni-doped varieties are currently ongoing in collaboration between fusion materials program and with an LDRD funded project at ORNL on first wall/blanket structural steels.

2.10.6 REFERENCES:

[1]. A. Bhattacharya, S.J. Zinkle, J. Henry, S.M. Levine, P.D. Edmondson, M.R. Gilbert, H. Tanigawa, C.E. Kessel, Irradiation damage concurrent challenges with RAFM and ODS steels for fusion reactor first-wall/blanket: a review, J. Phys. Energy 4 (2022) 034003.

2.11 PERFORMANCE EVALUATION OF MODIFIED 3Cr-3WVTa BAINITIC STEELS

Y. Yamamoto (yamamotoy@ornl.gov)

2.11.1 OBJECTIVE

This work aims to evaluate the advantages in the mechanical performance of newly proposed, modified 3Cr-3WVT bainitic steels developed at ORNL. The proposed steel was designed to eliminate the need for post-weld heat treatment (PWHT), as well as providing improved mechanical properties of both base metal and weldments compared to those of existing commercial bainitic steels or ferritic-martensitic (F-M) steels. The target applications are high-temperature structural components in fusion reactors, such as helium-cooled vacuum vessels operating up to 450 °C and blanket support structures operating up to 550 °C.

2.11.2 SUMMARY

Optimization of thermo-mechanical treatment to refine prior-austenite grain size, followed by evaluation of mechanical properties in both base metal and across the weldment, of the modified 3Cr-3WVTa steel were conducted. The major accomplishments in this fiscal year include (1) completion of the process optimization to refine prior-austenite grain size to less than ~100 μm with fully bainitic ferritic microstructure; (2) >25% improvement of the creep-strength in the base metal compared to non-optimized modified steel base metal and ~10% improvement of the cross-weld creep strength to date; and (3) achieving low ductile-brittle transition temperature (-45 °C) in the modified steel weld metal in the as-GTAW condition.

2.11.3 PROGRESS AND STATUS

Compositionally modified 3Cr-3WVTa bainitic steel ("Modified" steel) containing a higher Mn and lower C than in the "Original" steel, as summarized in Table 6, have been proposed and studied in the present project. The modification was based on an alloy design strategy of "high hardenability with low hardness" in the as-welded conditions to minimize the variation of mechanical properties between the base metal, weld metal, and the heat-affected zone.

Table 6. Nominal compositions of the steels in weight percent (balance Fe).

Wt.%	Cr	**Mn**	Si	Ta	V	W	**C**
Original	3.0	**0.4**	0.16	0.1	0.2	3.0	**0.1**
Modified	3.0	**2.0**	0.16-0.5	0.1	0.2	3.0	**0.05**

note: N < 50 wppm, P < 50 wppm, S < 20 wppm, and O = 20-60 wppm, from chemical analysis

Previously the modified steel was thermo-mechanically processed (hot-rolled and normalized) at 1100 °C, which followed the process conditions for the original steel and resulted in the as-processed (as-normalized) microstructure consisting of fully bainitic ferritic microstructure with relatively coarse prior-austenite grains (PAGS, ~300-500 μm), as shown in Figure 29a. By applying a modified thermo-mechanical process at 1000 °C, the PAGS was successfully refined into ~50-100 μm (Figure 29b) which could directly be connected to the improvement of room-temperature tensile properties and impact toughness, relative to the

coarse PAGS. In addition, as summarized in Figure 29c, the refined PAGS also resulted in improving the creep-rupture performance of the modified steel tested at 550 °C and 295 MPa. The steels after normalization + tempering at 700 °C for 1 h showed the nearly doubled creep-rupture life after PAGS refinement, and the creep test of the as-normalized specimen last more than 11,000 h at the same test condition (still on-going). The improvement mechanism is unknown, although it is speculated that the refined PAGS may promote the nucleation frequency (and therefore the refinement) of the carbide-free acicular bainite ferrite formation which benefits the hardenability of the steel. Detailed characterization is required to elucidate the mechanism, and the sample preparation is currently in progress.

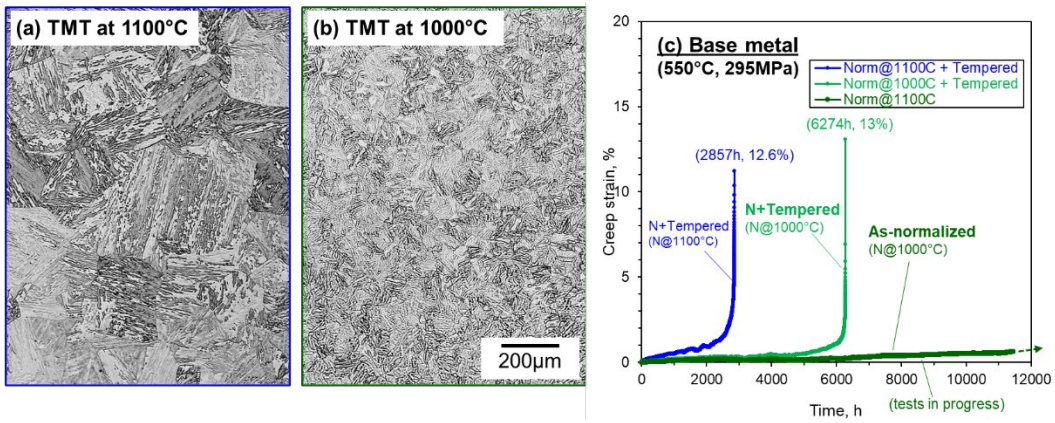

Figure 29. Optical micrographs showing a bainitic ferritic microstructure of modified 3Cr-3WVTa steel after hot-rolling and annealing at (a) 1100 °C and (b) 1000 °C, together with (c) creep-rupture curves of three different heat-treated specimens tested at 550 °C and 295MPa.

Creep-rupture performance of the base and the cross-weld materials for both original and modified steels is summarized in a Larson-Miller Parameter plot in Figure 30a. The modified steel specimens tested at 500-550 °C demonstrated >25% improvement of creep strength in the base metal, compared to the original steel. The modified steel specimens across the weldment (in the as-GTAW, gas-tungsten arc weld, with compositionally matched weld filler metal) also showed ~10% improvement of creep strength compared to the original steel weld after PWHT (at 700 °C for 1 h), suggesting successful achievement of high creep performance in the modified steel weld without PWHT. Charpy impact toughness test of the weld metal in the as-GTAW condition exhibited low ductile-brittle transition temperature (-45 °C), which also promises the advantage of the modified steel to be used without PWHT.

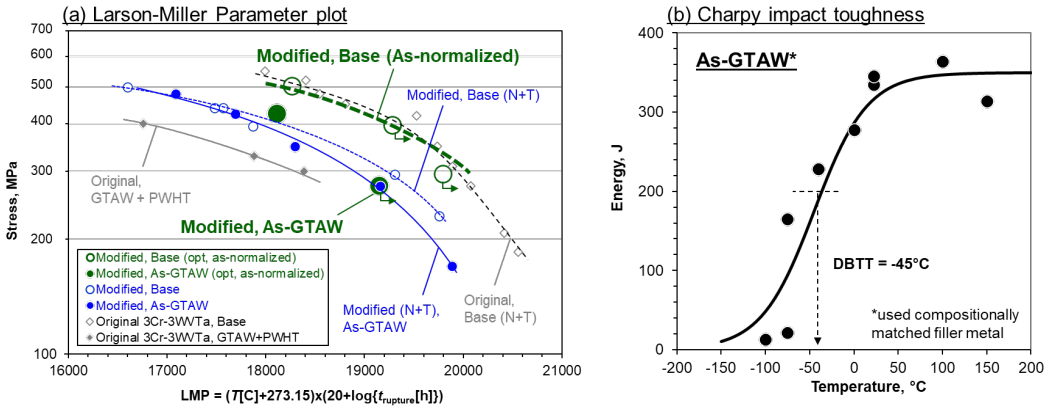

Figure 30. (a) Larson-Miller Parameter plot of the base and the cross-weld materials for the original and the modified 3Cr-3WVTa steels. (b) Charpy impact toughness.

2.11.4 FUTURE WORK

Additional creep-rupture tests will be performed. Detailed microstructure characterization will also be conducted to prove the advantage of PAGS refinement in the creep-performance. A trial AM print (wire-DED) of the modified steel is planned to build a component; possibly with less hardness variations than the original steel in the as-printed process.

3. CERAMIC AND COMPOSITE MATERIALS

3.1 ADVANCED CHARACTERIZATION OF SILICON CARBIDE MATERIALS

T. Koyanagi (koyangit@ornl.gov), Y. Katoh, D. Sprouster (State University of New York, Stony Brook)

3.1.1 OBJECTIVE

The goal of this task is to develop advanced characterization techniques for irradiated SiC materials to accelerate materials development. Modern analytical tools including Raman spectroscopy and high-energy x-ray diffraction (XRD) were employed.

3.1.2 SUMMARY

Understanding chemical disordering during irradiation of SiC materials at elevated temperatures by evaluating defect cluster chemical composition and analyzing homonuclear bonds will help prediction of material lifetime under fusion irradiation environments. Modern analytical studies of SiC detected irradiation-induced C clusters by Raman spectroscopy and quantified the displacement damage of the C and Si sublattice sites by high-energy XRD. Formation of the C clusters evidenced by Raman spectroscopy is consistent with the preferential C disordering found by XRD. The experimental results provided valuable evidence to support some of the atomic-scale modeling results.

The details of the experiment and analysis are reported in *Journal of Nuclear Materials 565 (2022) 153766.*

3.1.3 PROGRESS AND STATUS

3.1.3.1 Raman Spectroscopy

The key advantage of applying Raman spectroscopy to study irradiated SiC is its ability to analyze Si–Si and C–C homonuclear bonds, which makes this technique a common evaluation approach in recent studies on irradiation of SiC. The Raman spectra of the unirradiated SiC show that the peaks of the transverse optical (TO) and longitudinal optical (LO) phonon lines of β-SiC appear at around 800 and 950 cm^{-1}, respectively. Additional broad bands were observed only in irradiated specimens (Figure 31a). Those peaks are identified as related to vibrations of Si−Si (∼520 cm^{-1}) and C−C (∼1400 and ∼1600 cm^{-1} [D and G bands, respectively]) bonds.

This study highlights the presence of the D and G bands after irradiation. Figure 31b summarizes C–C bond peak development in SiC neutron- and ion-irradiated under various temperature and dose conditions and shows the coexistence of the D and G bands following irradiation at temperatures of >300 °C. The G band is attributed to the sp_2 C−C bond vibrations in graphite rings, and the D band is related to the disorder-induced Raman scattering. The recent Raman studies reached the consensus that graphitic C clusters are formed under irradiation at elevated temperatures, while irradiation at ambient temperature results in broad peak at ∼1420 cm^{-1} indicating amorphous-like C–C bonds. This is a significant finding because irradiation-induced C clustering was studied by computational simulation, but experimental evidence was lacking.

3.1.3.2 High-energy XRD

To understand short- and medium- range order, including bond length and structural disorder, recent studies employed pair distribution function (PDF) measurements using high-energy x-rays. This is an ideal method for uncovering the irradiation-induced structural disorder of both heteronuclear and homonuclear bonds.

Figure 32a shows the PDF of polycrystalline β-SiC unirradiated and neutron-irradiated at 540 °C to 0.01 dpa. $G(r)$ denotes the number of atoms in a spherical shell at a distance (r) in the SiC lattice. The first three Si–C, Si–Si and C–C, and Si–C correlation peaks are at 1.88, 3.08, and 3.62 Å, respectively. The difference of the PDF before and after irradiation (orange line in Figure 32a) identifies short- range radiation-induced disorder. A decrease in the intensity of the homonuclear and heteronuclear peaks indicates vacancy formation, and the formation of a new peak indicates interstitial-type defects.

Changes in defect populations, quantified by the PDF analysis, include an irradiation dose-dependent and temperature-dependent increase in the lattice defects, leading to an increase in the Si and C atomic displacement parameters (ADPs). The ADP captures diminished x-ray intensity from atom displacements from their mean positions in a crystal structure and is affected by lattice defects. Figure 32b shows changes in Si and C ADPs by neutron irradiation at low (60 °C) and elevated temperatures (380–790 °C). For all the cases, the ADP of C is greater than that of Si, indicating the preferential atomic displacement from the C sublattice relative to the Si sublattice. At the low temperature involving irradiation-induced amorphization, the ratio of C ADP relative to Si ADP was 2.2 (Figure 32b). The relative C ADP was ~1.5 in the case of irradiation at 380–790 °C where the material is still crystalline, indicating that the preferential C displacement is less significant at the elevated temperatures. The preferential C atom displacement could be a source of the C homonuclear bond formations found by Raman spectroscopy.

3.1.3.3 Future Work

To gain a complete picture of the chemical disordering, chemical analysis with a high-spatial resolution will be required to correlate bulk disorder characteristics, microstructure, and atomic-scale models. Experimental validations for the predictive model on the effects of chemical disordering on material properties will also be of importance.

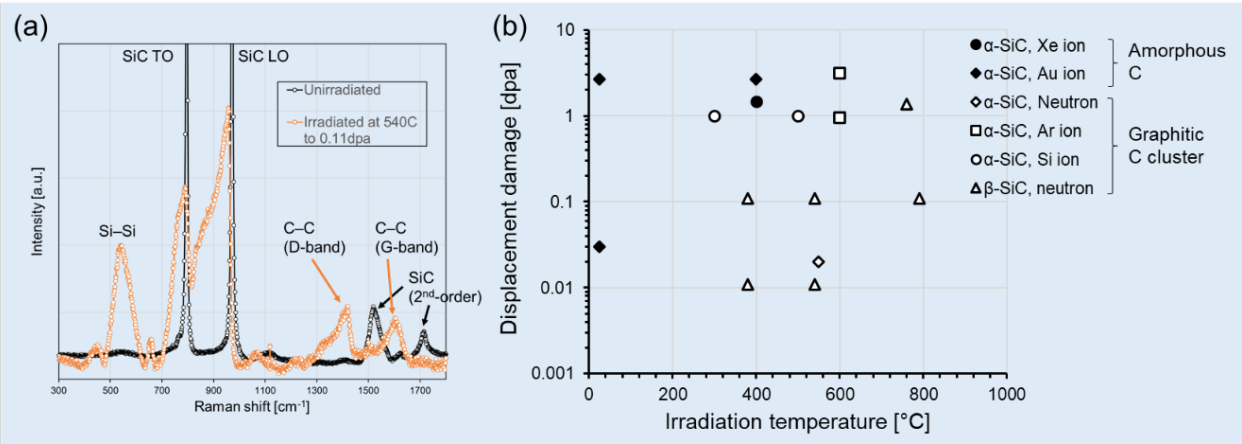

Figure 31. (a) Analysis of homonuclear bonds using Raman spectroscopy and (b) summary of C–C bond peak development in ion- and neutron-irradiated SiC. The broad peak at ~1420 cm^{-1} and the coexistence of D and G bands are attributed to the amorphous C phase and graphitic C cluster, respectively. The graph (b) includes literature data.

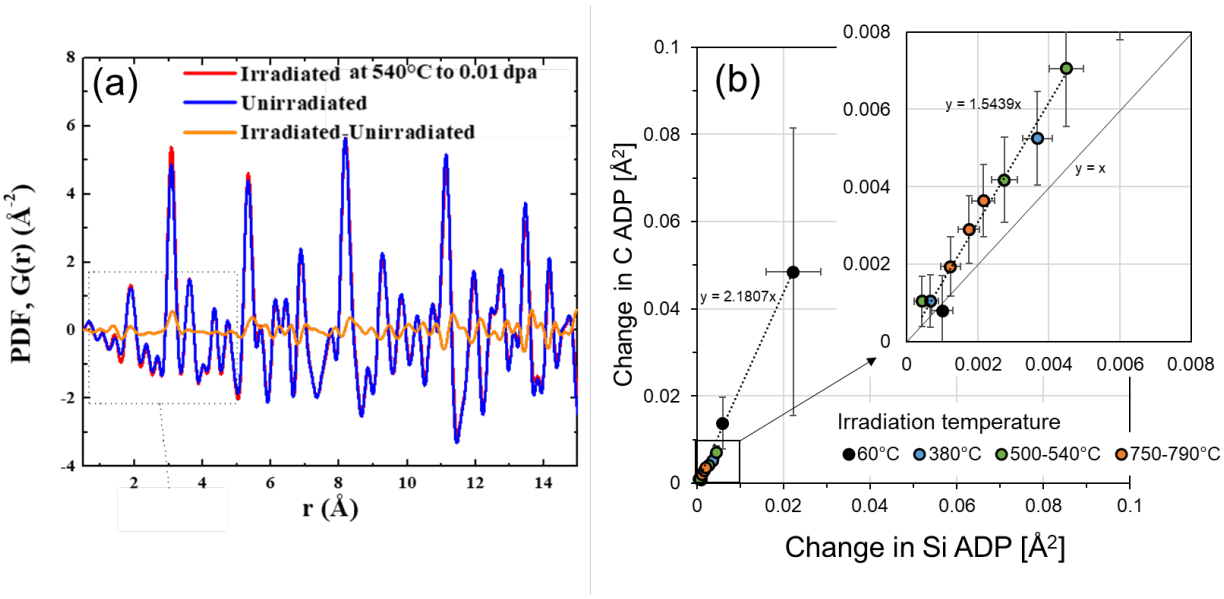

Figure 32. (a) Atomic-scale lattice disorder revealed via high-energy XRD-PDF analysis and (b) changes in Si and C ADPs by neutron irradiation at low (60 °C) and elevated temperatures (380–790 °C).

3.2 FAILURE EVALUATION OF NEUTRON-IRRADIATED SiC/SiC COMPOSITES

T. Koyanagi (koyangit@ornl.gov), Y. Katoh, T Nozawa (National Institutes for Quantum Science and Technology), H. Tanigawa (National Institutes for Quantum Science and Technology)

3.2.1 OBJECTIVE

Understanding the statistical properties of mechanical properties of unirradiated and neutron-irradiated SiC fiber reinforced SiC matrix (SiC/SiC) composites is essential for design of fusion reactor components. This study aims to evaluate the failure statistics and detailed damage accumulation behavior of the composites. Failure probability analysis was conducted based on the experimental data obtained.

3.2.2 SUMMARY

The underwater acoustic emission (AE) technique was applied to evaluate the failure behavior of miniature SiC/SiC composites specimens with flexural modes. Weibull statistical data of flexural properties of neutron-irradiated SiC/SiC composites were obtained, showing no serious degradation of AE onset stress, proportional limit stress (PLS), and ultimate flexural strength (UFS) by irradiation. The data analysis indicates that increasing the reliability of composites is essential to expand the design margin.

The technical details are fully described in a published article. (Journal of Nuclear Materials 566 [2022] 153787).

3.2.3 PROGRESS AND STATUS

3.2.3.1 Development of underwater AE technique

Underwater AE technology was adopted for post-irradiation experiments of miniature SiC/SiC composite specimens. Underwater AE generally travel straight in the water, and signals detected on the tank surface can be utilized in failure detection and evolution. To raise the reliability of damage monitoring by this developmental underwater AE technique, it is essential to establish a data calibration method oriented to the experimental setup. Several calibration runs have been conducted using reference specimens. The final test setup used for the post-irradiation examination is shown in Figure 33.

3.2.3.2 Failure probability analysis

Underwater AE technique combined with flexural test provided three key mechanical properties: AE onset stress, PLS, and UFS. For a structural design using a deterministic approach, the design stress is generally determined by considering a safety factor based on the reference strength. For example, the lower limit of the 95% confidence bounds of the 0.2% proof strength is one of the reference values used for design of structural components. In the case of composites, AE-onset stress, PLS, and ultimate strength could be considered in design. Figure 34 shows the probability density function of AE onset stress, PLS and UFS for Tyranno SA3 SiC/SiC composite before and after irradiation. The PLS peak was slightly (5–10%) reduced by irradiation, but the difference was negligible when focusing on the lower limit of the 95% confidence bound (both at about 170 MPa, about 50% of the mean stress). Similarly, when AE onset stresses were compared, both the peak stress and the lower limit of the 95% confidence bound were reduced by about 19% by irradiation. The lower limit of the 95% confidence bound of the AE onset stress of Tyranno SA3 SiC/SiC composite is about 75 MPa (about 40% of the mean stress) after irradiation, which corresponds to 20% of the mean value of the unirradiated PLS. The UFS peak was about 20% decreased by irradiation. The lower limit of the 95% confidence bounds for UFS after irradiation was approximately 270 MPa (58% higher than that of PLS). The data analysis indicates that the effects of irradiation on the mechanical properties were not significant but increasing the reliability of composites is essential to expand the design margin and to realize SiC/SiC composite structural components for fusion reactor applications.

3.2.4 FUTURE WORK

Ongoing efforts include design and development of next generation SiC/SiC composite materials with enhanced radiation resistance and base mechanical properties.

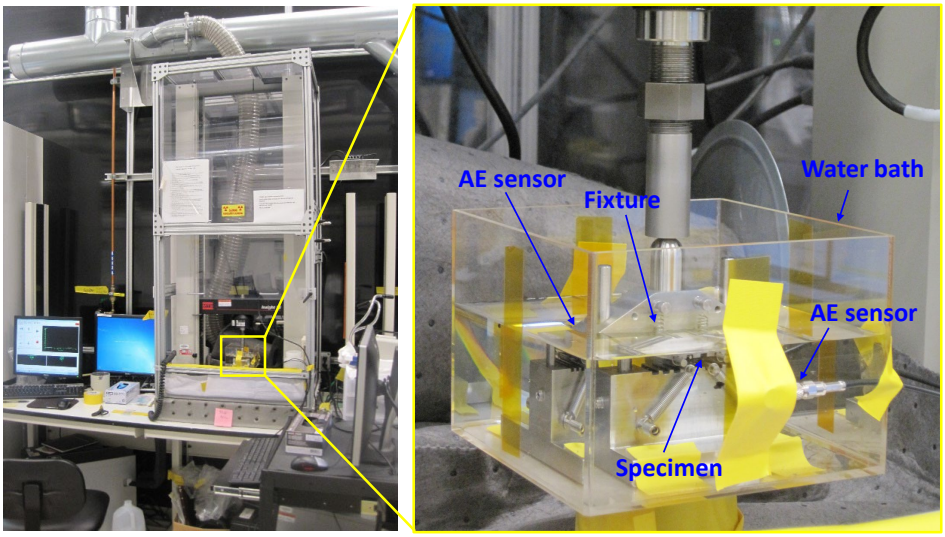

Figure 33. Experimental setup of underwater AE for irradiated SiC/SiC composites in LAMDA facility.

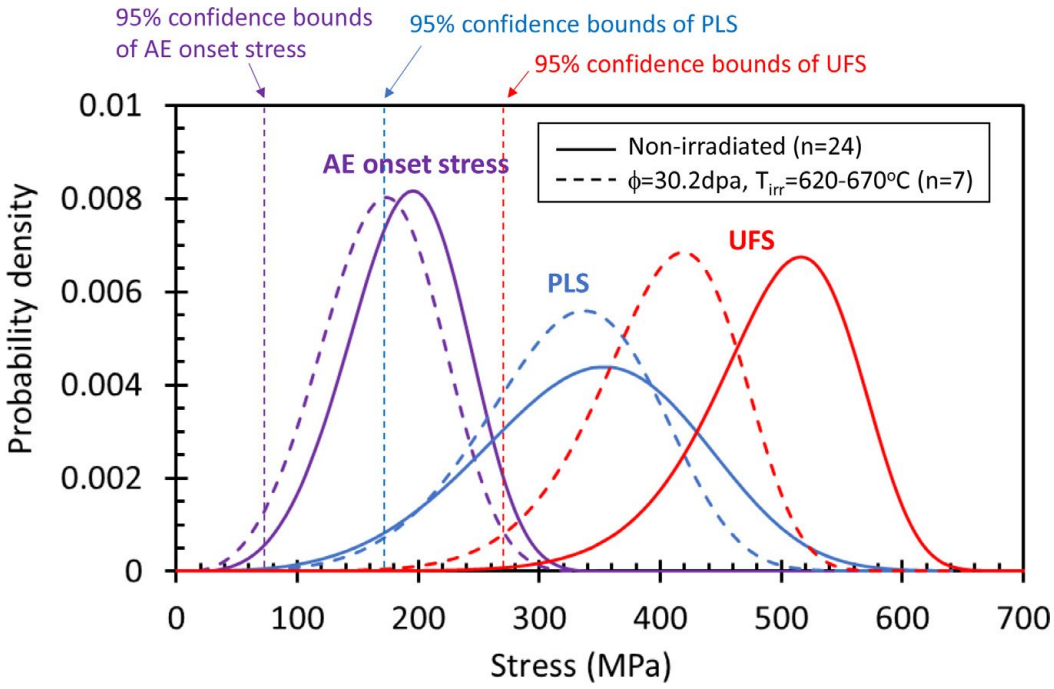

Figure 34. The fragility of Tyranno SA3 SiC/SiC composite specimens before and after neutron irradiation (neutron damage: 30 dpa, irradiation temperature: 620–670 °C). Note that the lower limits of the 95% confidence bounds are indicated for neutron-irradiated cases.

4. HIGH HEAT FLUX AND PLASMA FACING MATERIALS

4.1 NEUTRON IRRADIATION-ENHANCED GRAIN GROWTH IN TUNGSTEN AND TUNGSTEN ALLOYS

H. Gietl, T. Koyanagi (koyangit@ornl.gov), Xunxiang Hu, Y. Katoh, M. Fukuda (National Institutes for Quantum Science and Technology), A. Hasegawa (Tohoku University)

4.1.1 OBJECTIVE

To understand the microstructural stability of candidate plasma-facing materials under fusion-relevant environments, post-irradiation examinations of neutron-irradiated W and W based alloys were conducted.

4.1.2 SUMMARY

Neutron irradiation of W and W-3%Re alloys with and without K or La dopants was performed in the mixed-spectrum HFIR at nominal temperatures of ~850 °C and ~1100 °C to ~0.4 dpa. To the best of our knowledge, this study presents the first experimental evidence of radiation-enhanced recrystallization in W and undoped W–Re alloys at ~850 °C, conditions where thermal annealing does not cause any grain growth in a similar timescale. Radiation-enhanced crystallization is an important consideration when designing and applying W to plasma-facing components in future nuclear fusion reactors.

The details of the experiment and analysis are reported in *Journal of Alloys and Compounds 901 (2022) 163419*.

4.1.3 PROGRESS AND STATUS

Orientation maps obtained via electron backscatter diffraction (EBSD) for W materials in the as- fabricated, heat treated, and irradiated case are shown in Figure 35. High angle grain boundaries (HAGBs) are marked in white, and low angle grain boundaries (LAGBs) are marked in red. The recrystallization fraction did not change during the 24-day heat treatment at 850 °C, and there was significant recrystallization of W and W-3%Re after irradiation at 850 °C. After irradiation at >850 °C, all materials showed a recrystallization fraction greater than 70%, except La-doped W-3%Re, which showed superior resistance to recrystallization. Interestingly, K-doped W exhibits more significant recrystallization at higher irradiation temperatures compared with pure W, although the doped K inhibits grain growth when irradiated at 850 °C.

Radiation-enhanced diffusion theory was used to explain the observed low-temperature recrystallization. The degree of self-diffusion at 850 °C under neutron irradiation could be equivalent to that at 1200 °C without irradiation. The analysis suggested that the rate of displacement damage and defect sink effects of grain boundaries, precipitates, and dislocation loops largely affects radiation-enhanced recrystallization. The irradiation experiment at the higher temperature found that the La-doped W-3%Re alloy has the greatest resistance to recrystallization among the tested materials.

4.1.4 FUTURE WORK

Further microstructural investigations of the La-doped W-3%Re alloy, the most promising material among the tested alloys, will be conducted to gain insights for improvement of the microstructural stability under irradiation.

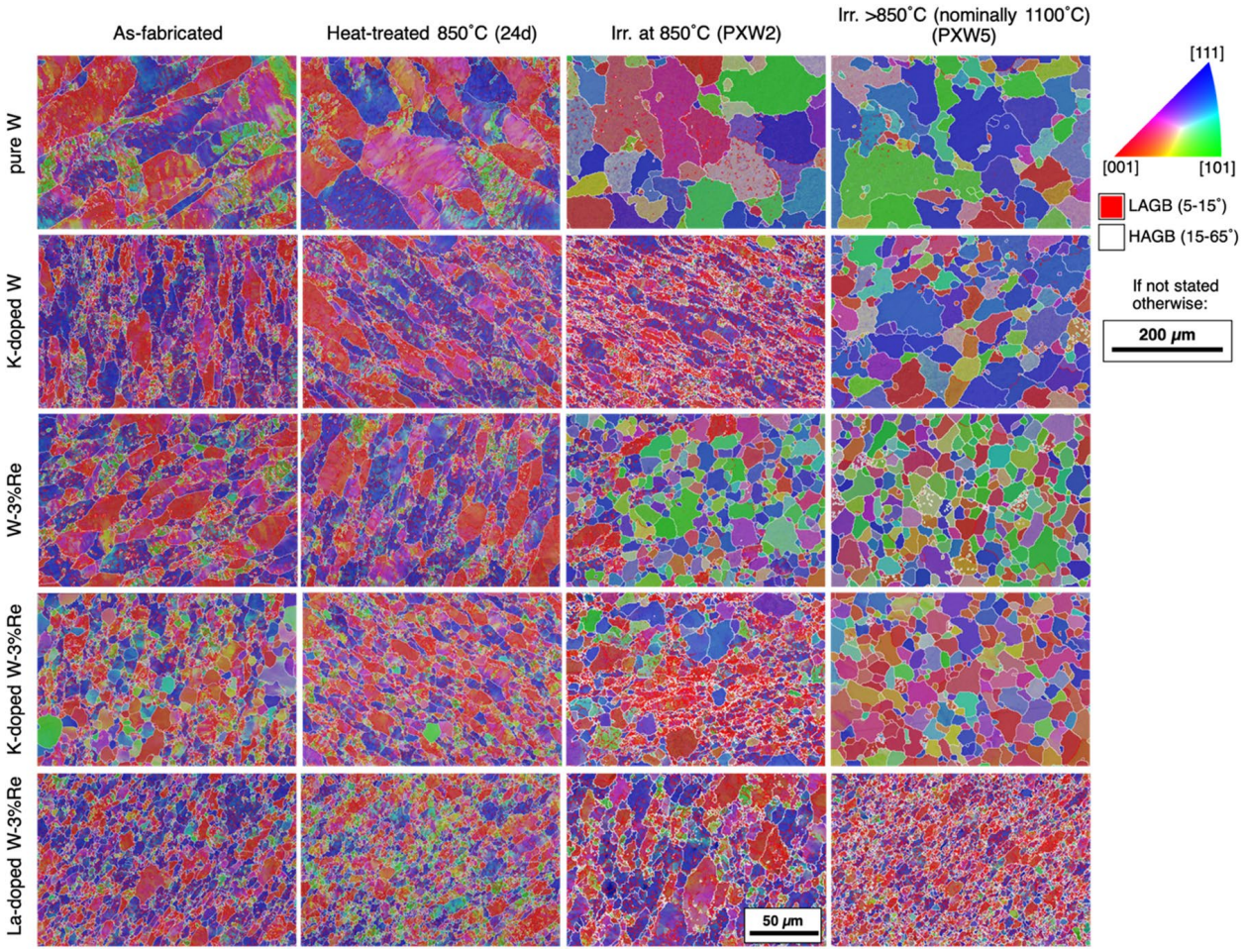

Figure 35. EBSD orientation maps for the nonirradiated and irradiated materials after correction and spike reduction.

4.2 HARDNESS TESTING OF MATERIALS IN THE FRONTIER COLLABORATION

L.M. Garrison (garrisonlm@ornl.gov), C. Abbott, N. Reid

4.2.1 OBJECTIVE

The Fusion Research Oriented to Neutron Irradiation and Tritium Behavior at Material Interfaces (FRONTIER) US-Japan collaboration aims to evaluate candidate plasma-facing materials, including alloys, composites, and joints between these materials. The microhardness measurements of the companion unirradiated materials were completed.

4.2.2 SUMMARY

In FY2022 irradiation capsules were built and underwent irradiation. Vickers microhardness tests have been completed on the unirradiated control materials from the FRONTIER neutron irradiation study. These tests are part of the Task 1 goals of the program and will be followed by microstructural investigations, miniature disc 3-point bend tests, and thermal property measurements.

4.2.3 PROGRESS AND STATUS

The FRONTIER project is a US-Japan collaboration which is investigating the effects of neutron irradiation on candidate plasma-facing materials. These materials include unalloyed reference materials, alloys of W and Cu, W-based composites, and joints between these materials. The project focuses on irradiation effects at interfaces, which include internal interfaces in composites as well as the interfaces between dissimilar materials in a joint. To understand the effects of neutron bombardment on these materials, the specimens will be irradiated in HFIR at 300, 500, and 800 °C for 1 and 3 cycles. For Task 1 of the FRONTIER collaboration, which focuses on the neutron irradiation effects on the materials, all the irradiated capsules were designed to use 3 mm diameter, 0.5 mm thick disc samples. Hardness, electrical resistivity, thermal conductivity, and microstructural analysis are among the properties which will be measured to understand the effects of irradiation. In this report the materials are described and the unirradiated microhardness results are given.

Each material type was given a code, and each individual sample was given a sample identification number. For sample IDs with two characters, the first character is the material type, and the second character is the unique identifier. For example, samples AZ and AB, both are material type A and the Z and B differentiate the individual samples. If a sample has three characters engraved, the first character is the material type and the second two characters are the unique identifier (used in cases where there were more samples than could be accommodated with only one character for a unique identifier). For sample IDs with four characters, the first two characters indicate the material type, and the second two digits indicate the unique identifier for the sample. For example, samples WC44 and WC46 and both WC type material and the 44 and 46 identify the individual samples. The material types and their codes are described in Table 7.

Table 7. The material codes and descriptions for the US Task 1 FRONTIER materials. The # represents the sample unique identifier character(s) that would appear after the code for the material type. If applicable, the collaborator who provided the samples for the project is listed.

Material Type	Short Description	Composition	Collaborator
WC##	Tungsten carbide	WC	Humphry-Baker (Imperial College London), and Smith (Oxford University)
FC##	Tungsten carbide with FeCr second phase	90 vol% WC, 10 vol% of Fe with 8 wt% Cr	Humphry-Baker (Imperial College London), and Smith (Oxford University)
P2##	Tungsten with titanium carbide particles fabricated with spark plasma sintering	W, 1% TiC	Allain (Penn State U.)
PT##	Tungsten with zirconium carbide particles fabricated with spark plasma sintering	W, 1% ZrC	Allain (Penn State U.)
A#	Alfa Aesar produced tungsten machined in “A” orientation	W	N/A
T#	Alfa Aesar produced tungsten machined in “B” orientation	W	N/A
HT##	Tungsten with Ni and Fe from laser additive manufacturing	95 wt% W, 3.5 wt% Ni, 1.5 wt% Fe	Trelewicz (Stony Brook U.)
GT##	Tungsten from laser additive manufacturing	W	Trelewicz (Stony Brook U.)
AE##	Tungsten from electron beam additive manufacturing	W	N/A
ST##	Tungsten and steel spark plasma sintered composite	50vol% W, 50vol% steel	Dorow-Gerspach, Ganesh, (Jülich)
LT##	Tungsten-steel laminate ()	50 vol% W and 50 vol% Fe-9Cr-2W-0.5Mo	N/A
F#	Tungsten 150 μm diameter fiber in tungsten matrix	W, trace oxide interlayer	Riesch (IPP-Garching)

KW##	Tungsten and copper particle reinforced composite	75vol% W, 25vol% Cu	N/A
X1##	Tungsten and copper fabricated with binder jet printing and infiltration of molten Cu	W, Cu	N/A
N#	Copper alloy with Cr, Nb, and Zr	95.6% Cu, 2% Cr, 1.35% Nb, 0.15% Zr	Snead, Cheng (Stony Brook U.)
C#	Copper reference	Cu	N/A

The tungsten carbide materials, WC## and FC## are considered for plasma facing components and shielding applications in fusion reactors. The P2## and PT## materials were prepared to understand the effects of dispersed carbide particles on tungsten microstructure during irradiation. The GT## is a control material to compare with HT## prepared by the same laser additive manufacturing method but including additives to try to maintain small grains at high temperatures and be fabricated by laser beam additive manufacturing without cracking. Electron-beam melted additively manufactured tungsten, AE##, was investigated to understand the interface between tungsten and internal pores. The ST## tungsten steel particle material and LT tungsten steel laminate are important for fusion applications that will need a tungsten to steel bond. The KW## material is a two-phase composite between tungsten and copper, because they do not diffuse into each other, the interfaces are perfect before irradiation. The advanced copper alloy, N#, has better high temperature creep resistance than standard CuCrZr alloys and was compared to the pure copper, C#. The Alfa Aesar tungsten plate material has been used previously in the PHENIX collaboration irradiations, and the same orientation naming convention was used here as used previously. The A# labeled samples were cut in orientation A and the T# labeled samples were cut in orientation B as shown in Figure 36.

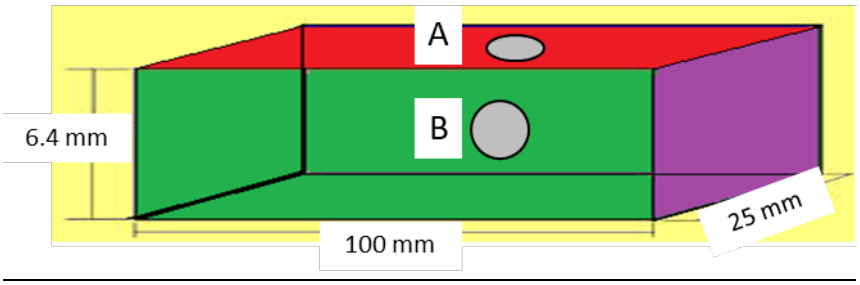

Figure 36. Illustration of the relative orientations of A (sample code A#) and B (sample code T#) tungsten plate produced by Alfa Aesar.

4.2.3.1 Hardness

The hardness of the materials was measured using a Future-Tech FM-700 Digital Microhardness tester. Each sample was indented 5 times with a load of 1 kg and a dwell time of 10 s. It was ensured that the indents were spaced out at least four times the width of each indent and that the thickness of the material

was more than ten times the depth of the indent. Furthermore, the guidelines for Vickers microhardness testing described in ASTM E384-17 were also followed.

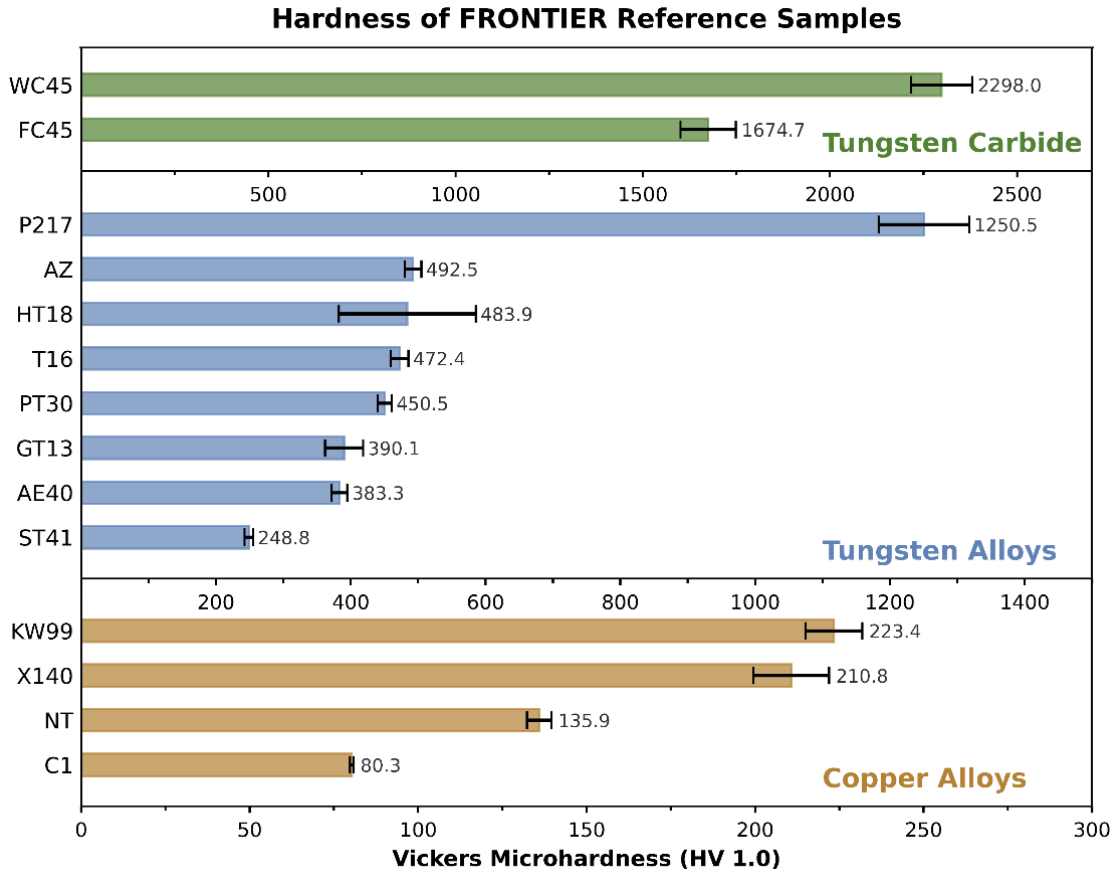

Figure 37. Mean hardness and standard deviation of unirradiated US Task 1 FRONTIER specimens. The individual sample IDs are listed for each bar. Note the different x-axis scale in the different sections of the graph.

The mean hardness and standard deviation of the materials in Table 7 were calculated and plotted in Figure 37. The tungsten carbide samples, WC45 and FC45, had a high hardness compared to the others, which matched expectations. The tungsten carbide with the iron and chromium had decreased hardness compared to the unmodified tungsten carbide. For the tungsten alloys, most of specimens were in a range of 380-500 HV. Adding titanium carbide particles to tungsten, sample P217, significantly increases the hardness. The tungsten steel composite, sample ST41, had a lower hardness than the other W-based materials, nearly as low as the W-Cu composite. For the copper-containing materials, each material was observed to be harder than the pure copper sample. The tungsten copper composite, KW99, had the highest hardness, followed closely by the additive manufactured tungsten copper composite, X140. The CCNZ alloy, NT, had a significantly increased hardness compared to the pure Cu, but significantly less than the W containing composites.

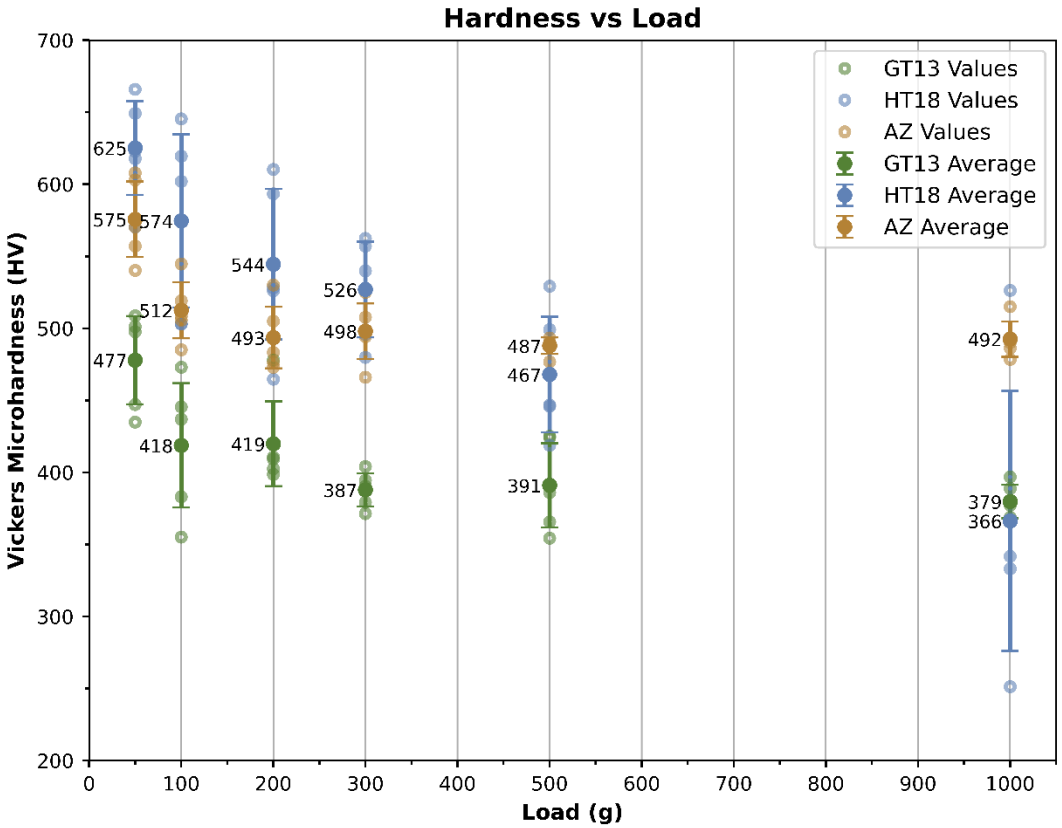

Figure 38. Hardness verses load plot of specimens HT18, GT13, and AZ.

Typically, a 1 kg load has been used to hardness-test tungsten-based materials for the US-Japan collaborations. However, the HT18 sample had a high standard deviation when a load of 1 kilogram was used. Upon examining the indents, cracks and imperfections in the indent pyramid shape was the reason for the spread in the data. A load versus hardness scan was performed and the uneven indents were not observed for lower loads than 1 kg. A sample with a similar fabrication history that did not visibly crack, GT13, and the standard pure W material A# were subjected to the same testing for comparison (Figure 38). From this scan, 500 g would be a more appropriate load for testing the HT## materials in the future, while the GT## and A# materials plateaued at indent values of 300 g and higher.

5. PLASMA-MATERIALS INTERACTIONS

5.1 CONSISTENT DESCRIPTION OF DEUTERIUM INTERACTION WITH TUNGSTEN SURFACE AS PART OF THE MPEX DIGITAL TWIN DEVELOPMENT

G. Samolyuk (samolyukgd@ornl.gov), Y. Osetskiy

Funded by Validated Design and Evaluation of Fusion Wall Components LDRD initiative # 10790.

5.1.1 OBJECTIVE

For the near future, the Material Plasma Exposure eXperiment (MPEX) will be the main experimental tool to be used in Oak Ridge National Laboratory for investigating processes during plasma material interactions (PMI) relevant to the fusion reactor conditions. The MPEX digital twin initiative aims to develop an interlinked set of computer model software to accelerate PMI science understanding and accelerate MPEX commissioning in achieving reactor-relevant fluences. The main objective of this task is to substitute the oversimplified binary collision approximation (BCA) for interaction of deuterium (D) with plasma facing materials, used so far, by the more realistic atomistic multibody modeling approach using classical and *ab initio* molecular dynamics.

5.1.2 SUMMARY

The interaction of D with the tungsten (W) surface was investigated using classical molecular dynamics (MD). A large statistic (>5000 modeling runs for each W surface orientation and D incident direction) of individual deuterium collision with W was used to collect data on deuterium backscattering, penetration depth and W sputtering for typical surface orientations. The atomistic modeling results were compared with the Stopping and Range of Ions in Matter (SRIM) code. It is found that the penetration depth obtained with MD is almost two times larger and is much more sensitive to surface orientation. The MD results for D backscattering are close to those obtained with SRIM. Target atoms sputtering, observed in SRIM modeling, was not observed at all in atomistic modeling for 100 eV energy of D interaction with W at 500 K.

5.1.3 PROGRESS AND STATUS

The molecular dynamics approach as implemented in the Large-scale Atomic/Molecular Massively Parallel Simulator (LAMMPS) [1] was used to model the interaction of D with the W surface. W-W and W-D interaction were described by EAM interatomic potential developed in [2]. The W surface was represented by a sample containing approximately 320,000 atoms. Thus, for [001] surface orientation it contains $20 \times 20 \times 400$ two atomics cubic cells. During calculations the position of atoms in the three bottom layers were fixed and periodic boundary conditions were applied in all directions. The periodic images of the system along one direction were separated by a vacuum layer of ~30 Å width representing W surface. During evolution, the system was treated as an NVE ensemble, and each incident ion was modeled in a system equilibrated for a different time to account for statistics on the atomic displacements for the corresponding temperature. The timestep of 0.5 fs was small enough to obtain the necessary accuracy. For each of three W surface orientations, {001}, {110}, and {111} three angles, corresponding to the velocity vectors {1,2,10}, {1,4,4}, and {4,4,1} were considered for 100 eV D incident atom.

As it was observed, for the same incident angle the ion trajectories are sensitive to the specific position from where D atom collides with the W-target surface. To account for this, the average values in our calculations, for the each angle we tested 6×6 matrix of different entrance positions distributed in the rectangular area were considered (see Figure 39 left as an example for {001} surface orientation). For each

initial position D atoms position we executed 150 trajectories, each starting at different time of equilibrating W-target. Each run continues until the D atom stops (localized with one elementary cell).

The results for {1,2,10} D angle and {001} W surface orientation penetration depth and back scattering ration are presented in Figure 39b and Figure 39c, respectively. All calculations were executed both with and without accounting for the electronic stopping power. As it can be seen (Table 8) the accounting for electronic stopping significantly changes the MD calculated penetration depth, l.

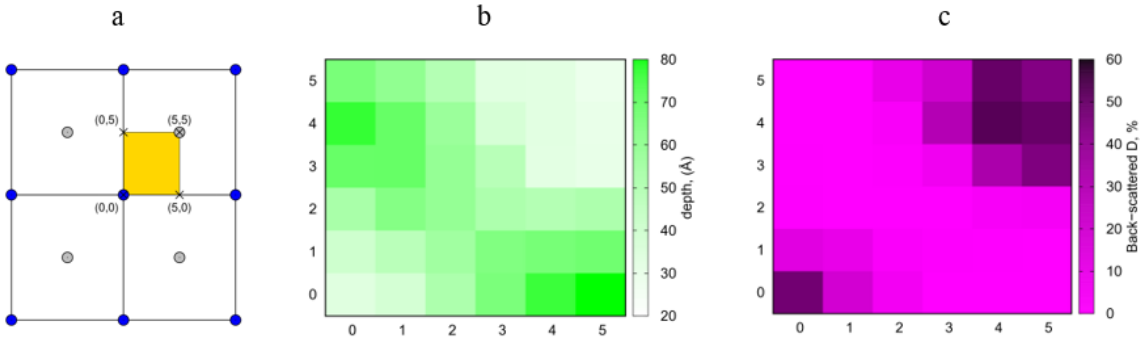

Figure 39. a) The rectangular area consists of 6x6 matrix of initial positions of the incident D atom for {001} W surface shown by yellow square; b) the penetration depth value for each position, averaged over ~150 runs, and c) fraction of backscattered D atoms. The D atom velocity is along {1,2,10} direction.

Thus, for D with initial velocity along {1,2,10} direction and interacting with {001} surface, the penetration depth calculated with the electronic stopping power is reduced from 253 to 53 Å. One of the most important findings is the two-times difference between MD and SRIM results. It worth mentioning that for D angle almost parallel to the surface, {4,4,1}, all D atoms in MD are backscattered, while in SRIM the penetration depth weakly depends on D atom velocity.

Table 8. D penetration depth, in Angstroms. The results presented in brackets are obtained without electronic stopping.

Incident direction	Incident angle, °	{001}	{111}	{110}	SRIM (5400 full cascades)
{1,2,10}	12	53 (253)	52 (230)	52 (181)	28
{1,4,4}	46	31 (150)	30 (163)	53 (192)	27
{4,4,1}	80	0	0	0	25

The result obtained for D backscattering ratio obtained with electron stopping are much closer to those obtained with the SRIM (Table 9). However, for close to normal to the W surface D velocity direction, the MD results give only about half of the penetration depth obtained in SRIM modeling.

Table 9. Fraction of backscattered incident D atoms, in %. The results presented in brackets are obtained without electronic stopping.

Incident direction	Incident angle, °	{001}	{111}	{110}	SRIM
{1,2,10}	12	20 (22)	21 (26)	25 (51)	47
{1,4,4}	46	47 (50)	36 (49)	37 (54)	58
{4,4,1}	80	100	100	100	75

5.1.4 FUTURE WORK

We continue collecting data on D penetration depth, back scattering, and W sputtering for a set of W energies and incident angles typical of MPEX plasma conditions. The collected data will be used for machine learning training a surrogate model predicting statistically averaged characteristics of plasma D interaction W surface on the fly. Later this will be used as part of MPEX digital twin and potentially a digital model of future fusion reactors.

5.1.5 REFERENCES

[1] LAMMPS Molecular Dynamics Simulator, https://www.lammps.org/#gsc.tab=0.

[2] P. Grigorev, D. Terentyev, G. Bonny, E.E. Zhurkin, G. Van Oost, J-M. Noterdaeme, Interaction of hydrogen with dislocations in tungsten: An atomistic study, J. Nucl. Mater., 465 (2015) 364.

6. LIQUID METAL COMPATIBILITY

6.1 LIQUID METAL COMPATIBILITY IN FUSION SYSTEMS

M. Romedenne (romedennem@ornl.gov) Y. Zhang and B. A. Pint

6.1.1 OBJECTIVE

Liquid metal compatibility studies consist of three separate tasks evaluating Li, Sn and Pb-17at.%Li for various fusion blanket and plasma-facing applications. Compatibility between Li or PbLi with RAFM-type steels (e.g., F82H) has been studied for many years; the current project considers the susceptibility of F82H to liquid metal embrittlement for liquid Li plasma facing components (divertor); and coated (aluminized) F82H interaction with SiC in flowing PbLi for the dual-coolant lead-lithium (DCLL) blanket concept. Characterization has been completed for the flowing Sn experiment and the project is now focused on inserting Sn-filled irradiation capsules into HFIR.

6.1.2 SUMMARY

Two thermal convection loop (TCL) experiments were completed in FY2021 and characterization of specimens from both experiments was completed in FY2022. Both TCLs were fabricated from Kanthal alloy APMT (Fe-21Cr-5Al-3Mo) and studied specimens that were pre-oxidized to form an alumina surface scale to inhibit alloy-liquid interactions. One TCL exposed pre-oxidized oxide-dispersion strengthened (ODS) FeCrAl specimens for 1000 h to flowing Sn with a peak temperature of 400 °C. Large specimen mass losses in the hot leg suggests that Sn is very corrosive, which was not observed in previous static capsule testing at 400 and 500 °C. The other TCL exposed SiC and pre-oxidized and coated F82H specimens to flowing Pb-Li with a peak temperature of 650 °C. Pre-oxidation of the exposed specimens and the slightly lower temperature resulted in much less interaction between the exposed alloys and SiC in PbLi compared to a previous TCL with a peak temperature of 700 °C with mostly bare alloys. For Li liquid metal embrittlement (LME), hollow specimen tensile testing of type 4340 steel demonstrated that the technique is able to identify LME when the material is susceptible.

6.1.3 PROGRESS AND STATUS

Liquid metals are being explored as a potential solution for the extreme environment at the plasma interface (liquid metal plasma facing divertor). For Li, the high vapor pressure is not attractive, but compatibility is reasonably good with RAFM steels up to 600 °C. Low alloyed carbon-steels (e.g., 4340 steel) were reported to be susceptible to liquid metal embrittlement (LME) and therefore is an area of concern for RAFM type steels where limited data is available. An LME evaluation and characterization of F82H (Fe-8Cr-2W) and 4340 steel are in progress using hollow tensile specimens primarily tested at 200 °C. In FY2021, experiments with F82H were conducted with no significant evidence of LME observed. In FY2022, hollow 4340 specimens were tested and confirmed LME in liquid Li (Figure 40a). The fractured surfaces were characterized (Figure 41b). A second set of hollow F82H specimens have been loaded with Li and are awaiting testing.

An alternative approach for this application is to use Sn, which has a much lower vapor pressure, but is known to be corrosive to most conventional alloys. Previous static capsule experiments showed good Sn compatibility with pre-oxidized APMT in Mo capsules at 400 °C and 500 °C for up to 2000 h. The next step in the evaluation with Sn was a flowing TCL experiment in which the specimens consisted of APMT and two ODS FeCrAl alloys (Fe-(10-12)Cr-6Al from ORNL and Japan) that were all pre-oxidized for 2 h at 1000 °C in air to form α-Al_2O_3. The experiment ran for 1000 h with a peak temperature of 400 °C and a

100 °C temperature gradient. In FY2022, characterization was completed, and a manuscript is being prepared. The final task is to test the performance of pre-oxidized FeCrAl in Sn at 400 °C under irradiation.

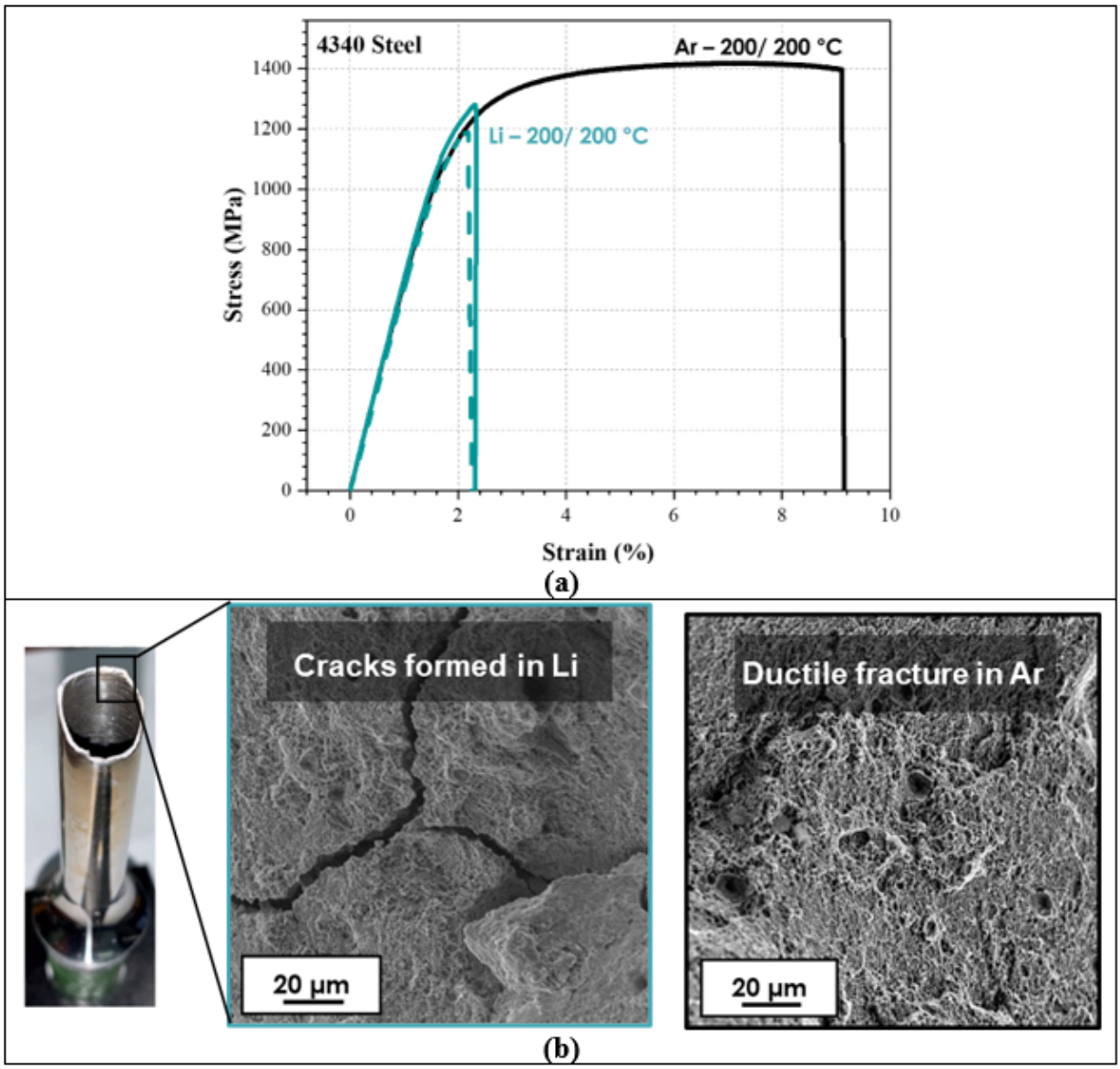

Figure 40. (a) Tensile test of 4340 steel in Ar (black) or Li (green) at 200 °C (1h pre-heat at 200 °C and test at 200 °C) (b) Secondary electron images of fracture surface after tensile tests in Li and Ar at 200 °C

In FY2021, the sixth Pb-Li TCL experiment also completed 1000 h with a peak temperature of 650 °C and characterization of exposed specimens was completed in FY2022. The previous TCL experiment with a 700 °C peak temperature exposed CVD SiC, ODS Fe-10Cr-6Al and a few APMT specimens and revealed a large dissimilar material interaction between SiC and FeCrAl with large metal losses and Fe-Cr carbide and silicide formation on the SiC specimens. By lowering the temperature and exposing primarily aluminized and pre-oxidized F82H specimens and CVD SiC specimens, lower mass transfer was observed with Figure 41a showing the thickness of the reaction product on the SiC specimens. TEM characterization identified carbides and silicide layers (Figure 41b) in agreement with the previous TCL experiment.

6.1.4 FUTURE WORK

During FY2023, six Sn-filled capsules with pre-oxidized FeCrAl specimens will be inserted into cycle 500 at HFIR. The next round of F82H LME experiments will be completed and characterized. Finally, the next Pb-Li TCL experiment is being assembled for 2,000 h operation to better determine the kinetics for the reaction with dissimilar material interaction between SiC, aluminized F82H and the APMT tubing.

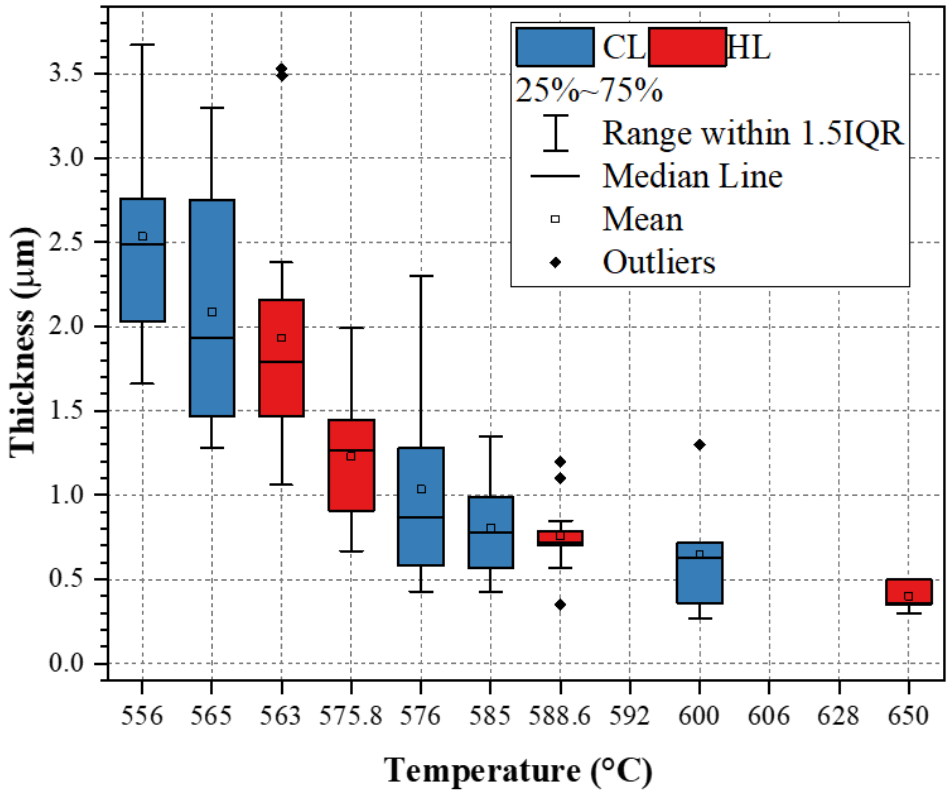

(a)

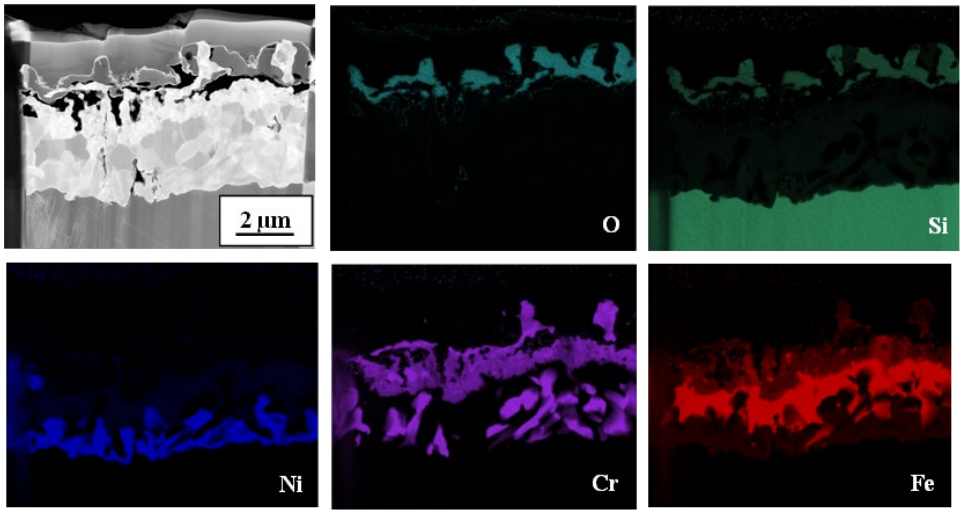

(b)

Figure 41. (a) Thickness of the corrosion layer formed on the surface of the CVD SiC coupons as a function of estimated exposure temperature in the TCL after 1000 h and (b) annual dark field TEM image and quantified EDX maps of the CVD SiC specimen located at the bottom of the cold leg (556 °C).

7. EXPLORATORY, UNIQUE, AND INNOVATIVE MATERIALS

8. GASSES IN MATERIALS

8.1 HYDROGEN DESORPTION BEHAVIORS FOR FUSION BLANKET STRUCTURAL MATERIALS AND MODEL ALLOYS

Weicheng Zhong (Oak Ridge National Laboratory)

8.1.1 OBJECTIVE

The objective of this work is to investigate hydrogen isotope desorption behaviors in castable nanostructured alloys (CNAs). CNAs have complex microstructural features, including grain boundaries, dislocation, and $M_{23}C_6$ and MX precipitates, which serve as hydrogen trapping sites. The experiments will investigate the thermal desorption behaviors in castable nanostructured alloys and binary model alloys of various microstructure. The results of this work will promote understanding on the contribution of different microstructure feature to hydrogen retention.

8.1.2 SUMMARY

Castable nanostructured alloys have multiple types of intrinsic microstructural features in as-fabricated materials. To promote understanding of these features individual contributions to hydrogen retention properties, this work investigated representative fusion structural materials of different microstructure, including as-received CNAs, aged CNAs, Fe-9%Cr binary model alloys with coarse grains, and heat-treated Fe-9%Cr alloys. Thermal desorption results show that the binary model alloys have less hydrogen retention than CNAs, likely due to fewer hydrogen trapping sites.

8.1.3 PROGRESS AND STATUS

Reduced activation ferritic-martensitic steels have complex structures, including hierarchical grain structure, high density of dislocations, and precipitates (include $M_{23}C_6$, with M = Cr primarily, and MC precipitates, where M = Ti/V/Ta primarily). A prior study has investigated hydrogen retention and desorption behaviors on a variety of RAFM and ODS steels [1]. However, the contributions of individual microstructure features to the hydrogen retention and desorption behaviors are not known. In this work, we have investigated CNAs of different microstructure. In addition, we have fabricated binary model alloys Fe-9%Cr, which were subjected to different heat treatments to produce different microstructures.

Figure 42 shows the inverse pole figure maps from the electron backscatter diffraction of the investigated alloys, including as-fabricated CNA, aged CNA, binary Fe-9%Cr of different microstructure. As-fabricated CNAs have the tempered martensite grain structure, where some grain grows after the thermal aging of 1100 hours at 775 ℃. Cr-rich $M_{23}C_6$ and Ti-rich MC precipitates have commonly observed in CNAs [2]. Although more detailed characterization, such as transmission electron microscopy, is required to confirm, aged CNA is expected to have reduced dislocation density and coarser precipitates with lower number density due to the thermal aging effects. We also include binary Fe-9%Cr alloys that exhibits large and equiaxed grain structure (designated as Fe9Cr CG) as shown in Figure 42c, where some grains exhibit >100 μm grain size. In addition, quenched and tempered binary Fe-9%Cr alloys (designated as Fe9Cr HT) is also included. Fe9Cr HT also exhibits large grains, but some subgrain boundaries are also observed. No $M_{23}C_6$ and MC precipitates are expected in Fe9Cr CG and Fe9Cr HT.

These CNA and binary model alloys are selected for thermal desorption analysis as they represent different grain structures and have different densities of dislocation and precipitates, therefore representing different population of hydrogen trapping sites.

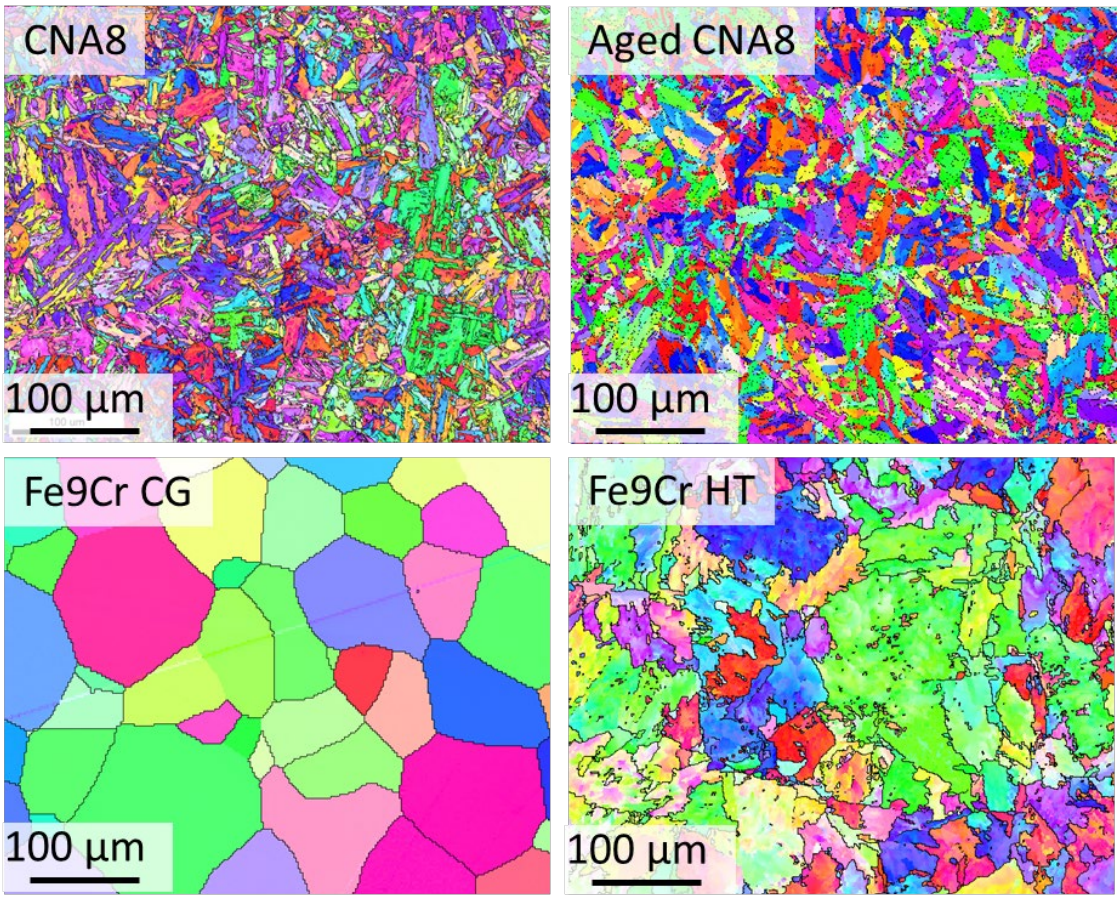

Figure 42. Inverse pole figure EBSD maps for CNAs and Fe-9%Cr binary model alloys of different microstructure; a) as-fabricated CNA, b) aged CNA, c) binary model alloy Fe-9%Cr CG, and d) binary model alloy Fe-9%Cr HT.

Samples were machined into 6 mm diameter discs, and they were polished using the standard metallurgical steps with the final polishing step using the vibratory polishing with 0.05 µm colloidal silica solution on both sides. Deuterium charging was in a deuterium environment of 1 atmosphere at 450 °C, which was followed by the thermal desorption measurement within 2 hours after the completion of the deuterium charging.

Figure 43 shows the thermal desorption results for all investigated samples. As-fabricated CNAs exhibited the highest hydrogen retention due to the most complex structure that include high number density of $M_{23}C_6$ and MC precipitates, dislocations, and hierarchical grain structure. The aged CNA shows reduced retention with the similar desorption peak temperature, which is consistent with the similar possible trapping sites with reduced population for the aged CNAs. The binary model alloys show lower hydrogen retention, which agree with their simpler microstructure, with lower population of boundaries and precipitates.

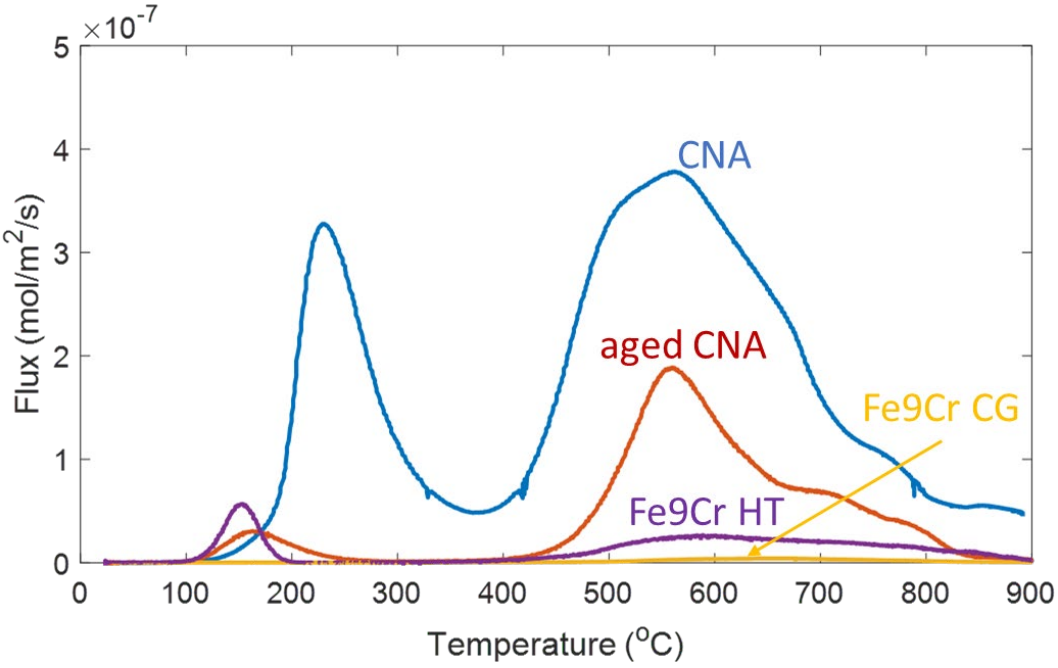

Figure 43. Hydrogen desorption as a function of temperature for as-received CNA, aged CNA, Fe-9Cr CG and Fe-9Cr HT.

8.1.4 REFERENCES

[1] Z. Chen, X. Hu, M. Ye and B. D. Wirth, "Deuterium transport and retention properties of representative fusion blanket structural materials," Journal of Nuclear Materials, p. 152904, 2021.

[2] L. Tan, L. Snead and Y. Katoh, "Development of new generation reduced activation ferritic-martensitic steels for advanced fusion reactors," Journal of Nuclear Materials, vol. 478, pp. 42-49, 2016.

9. ADVANCED MANUFACTURING

9.1 BENCHMARKING REDUCED ACTIVATION FERRITIC MARTENSITIC STEEL FABRICATED VIA ADDITIVE MANUFACTURING

T. Graening (graeningt@ornl.gov), N. Sridharan

9.1.1 OBJECTIVE

The production of reduced activation ferritic martensitic (RAFM) steels for structural applications with unconventional and novel designs for commercial fusion reactors, requires additive manufacturing of such materials. Here, the main objectives were to benchmark a 9Cr-2WVTa alloy fabricated via AM and rank its performance with wrought variants of the same alloy. Furthermore, to understand the response of the alloy to post-processing heat treatments and compare the performance of similar treatments on wrought counterparts and to identify gaps in processing. This provides insight into further areas for alloy design and set the stage for future activities in this area.

9.1.2 SUMMARY

The conducted study demonstrates that while tensile properties at room temperature and high temperatures are satisfactory, the as-build and samples after post-processing heat treatments (PPHT) exhibit significant heterogeneity in tensile elongation. This has been attributed to the presence of discontinuities in the build. The as-fabricated samples have an average tensile strength of 1190 + 12 MPa and an average elongation of 15 + 5% at room temperature and 658 ± 20 MPa ultimate tensile strength (UTS) and 14 ± 7% at 600 °C. After the post-weld heat treatment, mechanical properties decrease to around 600–650 MPa and an elongation between 20–25% at room temperature to 300 MPa UTS and 25–28% elongation at 600 °C. The characterization of microstructures at various length scales demonstrates that the as-fabricated structure has a significant fraction of delta ferrite in a lath martensitic matrix. No precipitates could be identified in the as-fabricated structure. PPHT led to a decrease in the area fraction of delta ferrite and precipitation of $M_{23}C_6$ and MX. Detailed characterization clearly demonstrates that the lack of precipitates in the as-fabricated structure could be due to the slow tempering response of the alloy.

9.1.3 PROGRESS AND STATUS

Four blocks of RAFM steel were printed using the same processing parameters, with three of these blocks heat treated to typical temperatures and times used for Eurofer97 and CNA steels. Microstructure characterizations using SEM and TEM have been performed from samples taken from different locations and orientations and tensile samples were machined from the printed blocks in build and transversal direction as shown in Figure 44. This enabled to investigate the effect of an intrinsic heat treatment during the DED process.

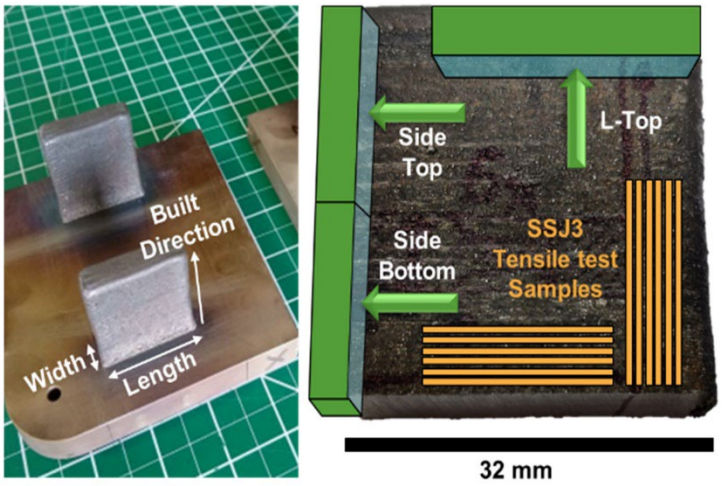

Figure 44: DED printed sample blocks, investigated orientations, and tensile sample orientation.

The tensile test results revealed a strong dependence on the orientation of the samples, with values matching Eurofer97 after heat treatments. Values in as-build condition, showed higher strength, but a much-lowered ductility, presumably caused by the higher amount of delta ferrite in as-build condition (see Figure 45).

The microstructure characterization showed no significant difference in void sizes for all conditions. The major differences were found in precipitate size and distribution, as well as elemental distribution inside precipitates. The results of the characterization are shown in Figure 46 and clearly demonstrate the necessity of a PPHT.

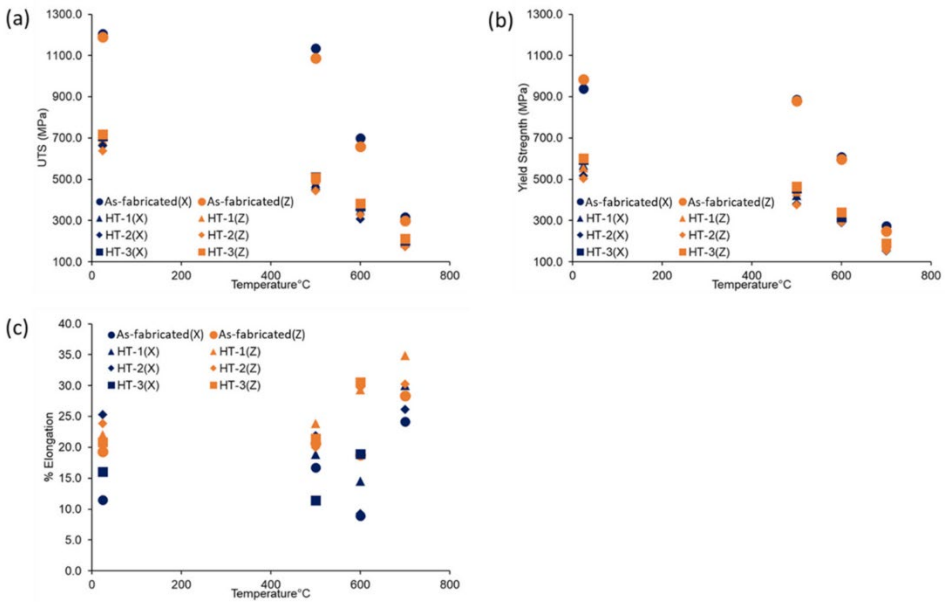

Figure 45: Tensile test results show the ultimate tensile strength (UTS), Yield Strength (YS) and total elongation for all conditions from room temperature to 700 C.

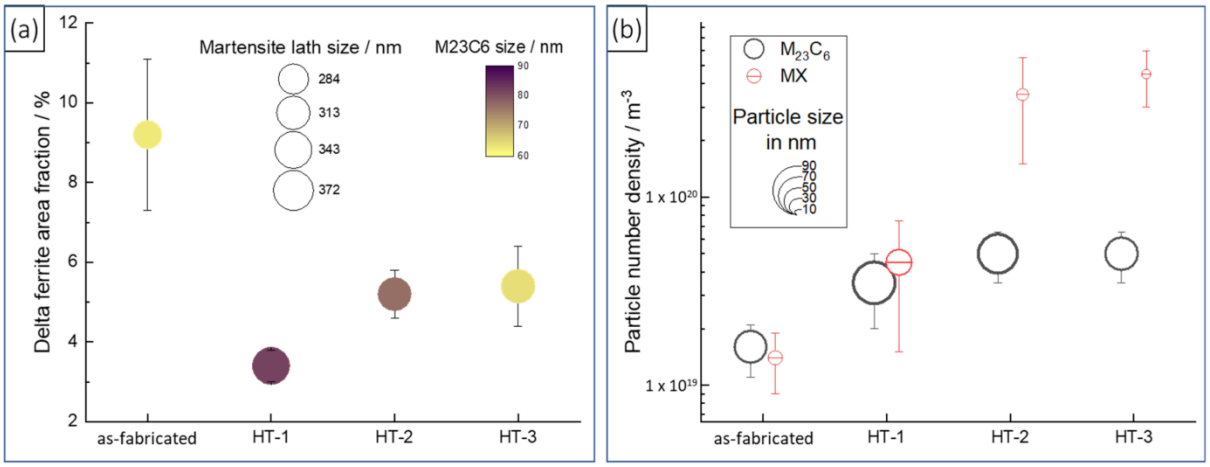

Figure 46: Summary of the microstructure properties of the four conditions.

9.1.4 FUTURE WORK

The research on the AM RAFM steel concluded successfully. Research to change processing parameters to reduce the required heat treatment would be valuable, but there are currently no plans to further investigate that research area.

REFERENCES

[1] Gräning, T.; Sridharan, N. Benchmarking a 9Cr-2WVTa Reduced Activation Ferritic Martensitic Steel Fabricated via Additive Manufacturing. Metals 2022, 12, 342. https://doi.org/10.3390/met12020342

9.2 GAMOW 3T PROJECT – ADDITIVE MANUFACTURING OF TUNGSTEN USING ELECTRON BEAM MELTING

M. Kirka, C. Ledford, T. Graening (graeningt@ornl.gov),

9.2.1 OBJECTIVE

Within the framework of the 3T GAMOW ARPA-E project, tungsten electron beam melting (EBM) was developed at MDF ORNL. The goal was to determine process parameters which enable EBM of tungsten for fusion applications. A high density, comparable mechanical properties to its rolled counterparts and the advantages of novel design approaches were the benchmark criteria.

9.2.2 SUMMARY

The GAMOW 3T project started in April 2021, which included the additive manufacturing of tungsten as a task set to be completed within 3 years. Initial testing using EMB was performed on tungsten followed by tungsten-rhenium powder later on. Prisms were manufactured and the spatial location of porosity was correlated to the density and the actual process variables and machine settings. An unsupervised Hierarchical Bayesian Model to was used to identify porosity seen in near-IR, while the model learns the probability distributions based on several labels and their distribution with the neighborhood association. The recyclability of tungsten powder was characterized by determining the oxygen content of the powder and final build across multiple prints. Process parameter – density maps were created to find the processing parameter sets enabling component densities of 99.98%. Differently shaped blocks and first complex-shaped component prints have been produced as shown in Figure 47. The influence of the energy density on the produced texture within the printed components revealed the potential for tailoring the texture. Higher energy densities changed the preferred 111 orientation of grains in build direction to a strong 001 orientation. The texture change was also shown for different thicknesses of prints.

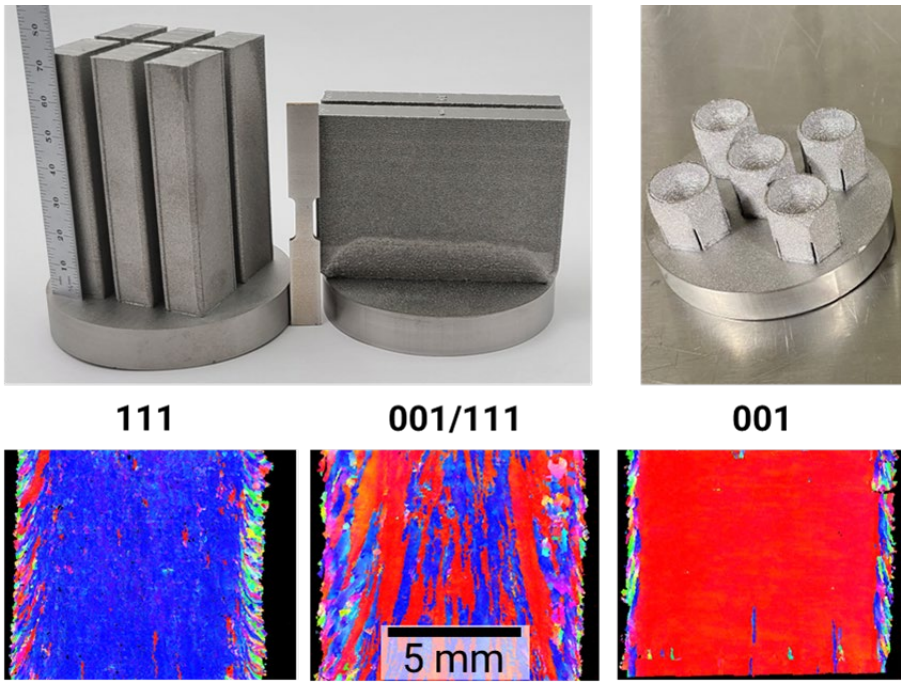

Figure 47: Top row: EBM printed tungsten blocks next to tungsten heads from the HEMJ design for divertors. Bottom row: Increasing energy density changes the texture in build direction from 111 to 001 orientation.

9.2.3 FUTURE WORK

The project is ongoing, investigating how W3Re could decrease the printing time by requiring a lowered energy density for full densification of the printed components. Additionally, components are printed for future DED transition layer printing on top of the tungsten printed HEMJ heads. An LDRD starting in FY23 will investigate the thickness anisotropy impact to inform microstructure tailoring. Furthermore, the minimum wall thickness with oriented grain sizes will be investigated.

10. COMPUTATIONAL MATERIALS SCIENCE

10.1 Li-BASED SOLID BREEDING MATERIALS: STABILITY AND TRITIUM RETENTION

G. Samolyuk (samolyukgd@ornl.gov), Y. Osetskiy

The research was supported by the Blanket and Fuel cycle program.

10.1.1 OBJECTIVE

The main objective of this task is to understand the basic mechanisms of the evolution of Li-ceramic breeding materials under the complex effects of Li burn-up and neutron irradiation. We are interested in identifying the mechanisms responsible for extending breeder material stability vs Li burn-up and improving tritium (T) retention properties over the irradiation cycle.

10.1.2 SUMMARY

The stability of Li-based ceramic breeder materials is studied using the multiscale approach. Density functional theory (DFT) modeling is used to identify low-scale properties such as defects and their transition state energies, phase stability, vibrational properties, and electric and thermal conductivity. Larger-scale kinetic Monte Carlo is planned to model atomic transport, defect evolution, accumulation, and tritium retention under Li burn-up and irradiation conditions.

10.1.3 PROGRESS AND STATUS

An important property defining the lifetime of the breeder is structural stability relative to Li burn-up level. During the Li burn-up, the transmutation reaction produces vacancies in Li sites, the accumulation of which may result in the destabilization of the original lattice. The initial approximation approach we used is directly removing Li from the system which simulates the reduction of Li content due to its burn-up. If the modeled system size is large enough, each "transmutation" just slightly increases the vacancy concentration so we can define the instability concentration quite accurately. Structural stability was studied by analyzing phonons dispersion in Li_2TiO_3 with Li vacancies using the DFT approach.

The electronic structure of the compounds is calculated within the DFT approach, using the generalized gradient approximation and the Perdew-Burke-Ernzerhof [1] parametrization of the electronic exchange-correlation functional. The calculations are executed using the plane-wave basis projector augmented-wave approach [2] as implemented in the Vienna Ab-initio Simulation Package (VASP) [3]. A plane-wave energy cutoff of 350 eV and $3 \times 3 \times 3$ **k**-mesh are used. The phonon dispersion spectra and thermal conductivity are calculated using second-order force constants obtained from VASP calculations as implemented in the PHONOPY [4]. The second-order constants are obtained from energy changes due to a finite atomic displacement of 0.03 Å. The second order constants in Li_2TiO are calculated in a $2 \times 2 \times 1$ super cell, this choice has been made because the elongated shape of the unit cell along the c-axis direction. Both results with and without the non-analytical term correction (LO-TO splitting) are presented. Li_2TiO_3 transforms toβ-Li_2TiO_3 above 575 K [5] with the monoclinic Li_2SnO_3-type structure, space group C2/c (15), lattice parameters of a = 0.50622, b = 0.87712, c = 0.97487 nm, β = 101.01°, and the unit cell contains 24 atoms [6], thus, the force constants were calculated in a super-cell containing 96 atoms. The Li burnup was modeled by the introduction of Li vacancies in the supercell (removing Li atoms). To model the random vacancy distribution, we applied a special-quasirandom-structure (SQS) [7].

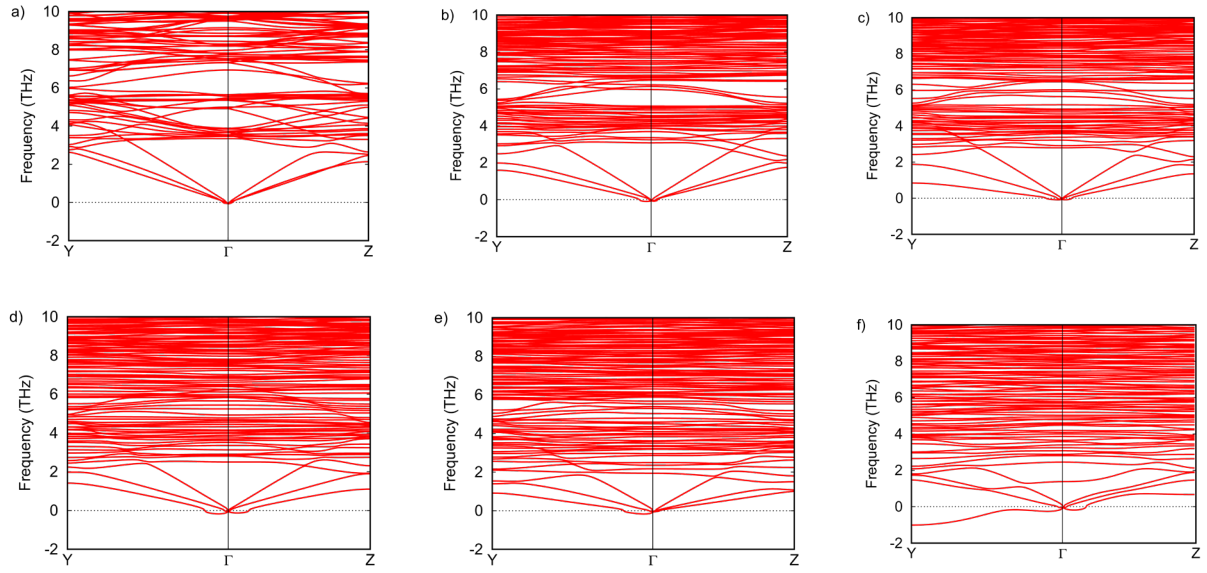

Figure 48. Phonon dispersion along the high symmetry direction in the irreducible part of Brillouin zone in $Li_{2(1-x)}TiO_3$ with Li vacancies concentration x: a) 0.00, b) 0.21, c) 0.26, d)0.32, e) 0.41, and f) 0.5, respectively.

The calculated phonon dispersion along high symmetry directions in the irreducible part of the Brillouin zone (BZ) is presented in Figure 48. In pristine Li_2TiO_3 all frequencies are positive. In the current work, we use the following notation to specify the concentration of Li vacancies, x, $Li_{2(1-x)}TiO_3$. The first weak instabilities are formed near the Γ-point at x=0.21, Figure 48a. This could be a precursor of structural transitions, [8, 9] modulated with a long wave vector structure at low temperatures and is usually washed out with increasing temperature due to an anharmonic contribution growing with temperature (see discussion in the provided references). Even if the k-space area of negative frequencies slightly increases with the change of vacancies concentration from x=0.21 to x=0.41. The first case of fully developed lattice instability formation corresponds to x=0.5, Figure 48e. In this case negative the acoustic phonon branch with negative frequency is formed along $\Gamma - X$ direction and reaches the largest negative value -1 THz at BZ boundary in point X.

Thus, it was demonstrated that the Li_2TiO_3 lattice is structurally stable up to about the point where half of the Li atoms burn up.

10.1.4 FUTURE WORK

The first approach will be modified by considering the temperature and accumulation of tritium atoms due to Li transmutation.

10.1.5 REFERENCES

[1] J.P. Perdew, K. Burke, M. Ernzerhof, Generalized gradient approximation made simple, Physical Review Letters 77(18) (1996) 3865-3868.

[2] P.E. Blöchl, Projector augmented-wave method, Physical Review B 50(24) (1994) 17953-17979.

[3] G. Kresse, J. Furthmüller, Efficient iterative schemes for ab initio total-energy calculations using a plane-wave basis set, Phys. Rev. B 54 (1996) 11169.

[4] A.Togo, L. Chaput, I. Tanaka, Distributions of phonon lifetimes in Brillouin zones, Physical Review B 91(9) (2015) 094306.

[5] A.Gicquel, M. Mayer, R. Bouaziz, SUR QUELQUES COMPOSES OXYGENES DU TITANE ET DES ALCALINS (LI, NA); ETUDE DES BINAIRES M2O-TIO2 DANS LES ZONES RICHES EN OXYDE ALCALIN, 1972.

[6] Z. Wan, Y. Yu, H.F. Zhang, T. Gao, X.J. Chen, C.J. Xiao, First-principles study of electronic, dynamical and thermodynamic properties of Li2TiO3, The European Physical Journal B 85(6) (2012) 181.

[7] A. Zunger, S.H. Wei, L.G. Ferreira, J.E. Bernard, Special quasirandom structures, Physical Review Letters 65(3) (1990) 353-356.

[8] V.G. Vaks, G.D. Samolyuk, A.V. Trefilov, On anomalies of anharmonic effects for soft phonons in alkali and bcc alkali-earth metals, Physics Letters A 127(1) (1988) 37-42.

[9] G.D. Samolyuk, Y.N. Osetsky, G.M. Stocks, J.R. Morris, Role of Static Displacements in Stabilizing Body Centered Cubic High Entropy Alloys, Physical Review Letters 126(2) (2021) 025501.

11. INTERNATIONAL COLLABORATIONS

11.1 UKAEA PROJECT

T.S Byun, J.W. Geringer, Y. Lin, Y. Katoh (ORNL), A. Quadling (UKAEA)

11.1.1 BACKGROUND

The United Kingdom Atomic Energy Authority (UKAEA) is engaged in exploring critical challenges related to the realization of fusion energy, including fundamental research on structural materials that can survive the harsh environments envisaged inside a future fusion reactor. The required research needs to use irradiation and post-irradiation testing and evaluation capabilities, which the United Kingdom do not have. The ORNL is under contract to perform the Neutron Irradiation and analyze the Materials Properties by preparation, irradiation, and post-irradiation examination/evaluation (PIE) of these select materials to determine their suitability for use in fusion energy systems. This requires the use of several unique ORNL facilities including HFIR and the Irradiated Materials Examination and Testing (IMET) hot cell facility and Low Activation Materials and Development Analysis (LAMDA) laboratory.

The purpose of the program is to perform basic research on understanding key phenomenon regarding irradiation induced degradation mechanisms in structural materials envisaged for fusion reactor applications.

11.1.2 PROJECT SCOPE

This collaborative fundamental research focuses to investigate the behaviors of fusion structural materials under irradiation. The materials of interest in order of priority include Fe-Cr binary alloys, 10-14%Cr ODS alloys, CNA alloys, FM steel welds, austenitic stainless steels, Cu alloys and SiC/SiC composites. The two main project components: (i) a PIE campaign on existing HFIR irradiated materials available at ORNL and (ii) new HFIR irradiations using rabbit capsules and PIE. The PIE activities include mechanical testing at IMET and LAMDA, physical property measurement, and microscopy. In addition to the funding for PIE and irradiations, UKAEA will provide assignees to help with the campaign.

11.1.3 PROGRESS AND STATUS

- The new proposal is being reviewed and expected to kick-off during the first quarter of calendar year 2023.
- Materials are collected for new irradiation.

11.2 EUROFUSION PROJECT

T.S Byun, J.W. Geringer, T. Graening, Y. Katoh (ORNL), M. Reith (KIT)

11.2.1 BACKGROUND

The Karlsruhe Institute of Technology (KIT), as an EUROfusion project, seeks to produce blanket, baseline, design-relevant materials properties data for EUROFER material variants. ORNL is under contract to assist the neutron irradiation and materials testing and evaluation tasks by preparation, irradiation, and post-irradiation examination/evaluation (PIE) of the steels to determine their suitability for use in fusion energy systems. This requires the use of several unique ORNL facilities including the HFIR, Irradiated Materials Examination and Testing (IMET) hot cell facility, and Low Activation Materials Development and Analysis (LAMDA) laboratory.

11.2.2 WORK SCOPE

The Phase I contract ended back in 2019 after completing Phase 1a project. Later, both KIT and ORNL intended to continue the collaboration project in the field of neutron irradiation and post-irradiation examination (PIE) for qualification of EUROfusion materials in simulated fusion reactor environments. The current KIT-ORNL collaboration program has two subprojects:

One (Phase 1b) project is to perform the PIE of specimens that are still irradiated within the Phase 1a (EUROfusion LOT-I campaign) KIT-ORNL contract. This Phase 1b project (LOT-I PIE) can be started as soon as HFIR irradiation is completed.

The second project targets at the investigation of neutron irradiation damage by gas transmutation in 9%Cr steels based on isotopic tailoring. The KIT-ORNL application (Phase 2) includes various elements: (1) Extending an already running irradiation of EUROFER-54Fe to 25-30 dpa, (2) 54Fe and 58/60 Ni isotope procurement, fabrication of isotopic tailored EUROFER-type materials, and machining samples, (3) design and fabrication of irradiation capsules, (4) neutron irradiation to approximate target levels of 12-15, 25-30, and >50 dpa, (5) PIE of EUROFER-54Fe from point (1), and (6) PIE of isotopic tailored materials from point (2) after 12-15 dpa.

11.2.3 PROGRESS AND STATUS

After the Phase I contract ended back in 2019, the 14 remaining irradiation vehicles (i.e., rabbit capsules) completed the original planned irradiation in HFIR, which targeted at 25 dpa (~12 cycles) and temperatures ranging between 200 to 400 °C. The capsules were loaded with Eurofer-97 alloys provided by KIT and the EUROfusion program collaborators.

11.2.4 FUTURE PLANS

- PIE for the Phase-1b specimens to be started in middle 2023.
- Phase 2 irradiation is expected to start in late 2023.

11.3 US-JAPAN (QST) COLLABORATIONS ON STRUCTURAL MATERIALS

C. On (onc1@ornl.gov), A. Bhattacharya, X. Cheng, J. W. Geringer, Y. Katoh (ORNL), T. Nozawa, M. Ando, D. Hamaguchi, T. Kato, H. Tanigawa (QST, Japan)

11.3.1 BACKGROUND

This long-standing collaboration between the US DOE and the National Institutes for Quantum Science and Technology (QST), Japan, jointly pursues activities using the advanced capabilities for materials irradiation and post-irradiation examination at ORNL, especially using HFIR, hot cells, and LAMDA. The focus is on ferritic steels and other advanced materials, especially the development of the materials database for the design of facilities beyond ITER. The goals include achieving DEMO-relevant performance data on structural materials neutron irradiated in HFIR to high levels of displacement damage.

The DOE-QST collaboration continues to steadily build the materials databases for the RAFM alloys that include F82H, ODS, and Eurofer97 steels and other materials such as nuclear grade SiC composites and copper alloys. This database is being used by QST to predict performance of components of a DEMO fusion reactor.

11.3.2 PROGRESS AND STATUS

The annual steering committee meeting was hosted by ORNL and remotely held on February 14 and 17, 2022. The restrictions of the COVID-19 pandemic continued preventing assignees to visit Oak Ridge. However, both parties noted with satisfaction, that the steady progress and high productivity of this partnership continued despite the limitations imposed by the pandemic.

During the past year irradiation experiments that continued irradiation in the reactor included rabbit capsules of the F13 series, the JCR series, the SCF series for FSM-P8 and the FMP series. The rabbit capsules with reduced activation ferritic/martensitic (RAFM) steels, mainly F82H as well as some SiC specimens, have completed irradiation while other high fluence capsules remain in the reactor. Rabbit capsules with Cu alloy variations completed irradiation. A new rabbit capsule irradiation series, the FH series with F82H alloy variations, has started with the first set of 5 dpa rabbit capsules in HFIR. The next set for 80 dpa exposure is scheduled to start irradiation during FY23.

The post-irradiation examination (PIE) completed this past year include hardness measurements, tensile testing, and steel and SiC microstructural analysis. PIE on specimens from experiment JP28-31, RB-15J, RB-19J is continuing. The disassembly of FMP01, -02, -04, and -05 rabbit capsules are completed.

11.3.3 FUTURE PLANS

The next QST steering committee meeting will be hosted in ORNL on March 1-2, 2023.

11.4 US-JAPAN FRONTIER PROGRAMS

C. On (onc1@ornl.gov), L. Garrison, B. Pint, J. W. Geringer, C. Kessel, Y. Katoh

11.4.1 BACKGROUND

In April 2019, the US/Japan Fusion Research Collaboration started a new Project, FRONTIER (Fusion Research Oriented to Neutron irradiation effects and Tritium behavior at material IntERfaces), with the objective of evaluating reaction kinetics and neutron irradiation effects at interfaces in DEMO divertor systems. FRONTIER consists of four tasks: (1) evaluate irradiation effects on reaction dynamics at plasma-facing material/structural material interfaces; (2) perform tritium transport through interface and reaction dynamics in accident conditions; (3) measure corrosion dynamics at liquid-solid interfaces under neutron irradiation for liquid divertor concepts; and, (4) engineering modeling. As in PHENIX, the project participants include ORNL, INL, SNL, NIFS, and Japanese universities. ORNL is leading three of the four tasks.

11.4.2 PROGRESS AND STATUS

During FY 2022, the FRONTIER efforts continued with focus on maturing the bonded or joint plasma facing materials, the development of irradiation capsules to support the irradiation matrices for the various tasks, the execution of a flowing Sn test, and the examination of a specific concept that focusses on liquid lithium, divertor only LM PFC and flowing liquid metal, to define a more detailed engineering design model.

The third FRONTIER steering committee meeting was held remotely on February 1-2, 2022, and hosted by ORNL. The majority of personnel exchanges and workshops were either postponed or held virtually due to the COVID19 pandemic restrictions.

Thirty capsules have been designed for Phase I and include the 3 mm disk design, 6 mm disk design, fracture toughness bend bar design, and the Sn corrosion rabbit design. Twenty-one capsules are assembled and placed in HFIR for irradiation. Thirteen capsules already completed irradiation in HFIR cycles 495-498. Nine of the remaining capsules are assembled and are scheduled to start irradiation in HFIR cycles 499 and 500.

11.4.3 FUTURE PLANS

The fourth FRONTIER steering committee meeting will be hosted in ORNL on March 9-10, 2023.

12. EXPERIMENTAL TECHNIQUES AND LABORATORY SYSTEMS

12.1 SMALL SPECIMEN TEST TECHNIQUES DEVELOPMENT: MASTER CURVE FRACTURE TOUGHNESS ROUND ROBIN STUDY

X. Chen (chenx2@ornl.gov), M. Serrano (CIEMAT), R. Hernández (CIEMAT), J. Reed, E. Manneschmidt, M. A. Sokolov, S. Gonzalez De Vicente (IAEA), Y. Katoh

12.1.1 OBJECTIVE

Under the International Atomic Energy Agency (IAEA) Coordinated Research Projects (CRP) framework, this work aims for evaluating specimen size and geometry effects on Master Curve fracture toughness measurement of fusion structural materials. The goal is to establish a Mater Curve testing and analysis guideline based on interlaboratory round-robin results and best practices.

12.1.2 SUMMARY

The development of Small Specimen Test Techniques (SSTT) is necessary to evaluate the performance of fusion structural materials. Under the auspices of the IAEA CRP framework, a round robin study of specimen size and geometry effects on the fracture toughness properties of EUROFER97 and F82H was initiated among Oak Ridge National Laboratory (ORNL), Centre for Energy, Environment and Technology (CIEMAT), and the UK Atomic Energy Authority (UKAEA). The latest findings are:

1) There was no obvious specimen size effect in 0.5T compact tension (CT) and 4 mm mini-compact tension (miniCT) specimens on measured Master Curve reference temperature T_0, while 1.65 mm bend bar specimens yielded a higher (more conservative) T_{0Q}.
2) For the minimum number of specimens needed for evaluating T_0, ASTM E1921 requirements (number of specimens here?) can be applied for 0.5T CT and 4 mm miniCT specimens, whereas for 1.65 mm bend bar specimens, 12 uncensored tests are required.
3) Experimental quality control, especially the quality of fatigue precracking, is critical for yielding valid Master Curve results.

12.1.3 PROGRESS AND STATUS

ORNL is leading the Maser Curve Round Robin tests with participation from CIEMAT and UKAEA. The materials used in the round-robin project are EUROFER97 batch-3 and F82H-BA12 reduced activation ferritic-martensitic (RAFM) steels. A wide variety of specimen sizes and geometries have been tested, allowing in-depth investigation of the specimen size effect on measured fracture toughness. More detailed results can be found in Refs. [1&2] and are briefly summarized here:

1. The ASTM E1921 Master Curve and its tolerance bounds show excellent representation of transition fracture toughness for EUROFER97 batch-3 and F82H-BA12. Figure 49 shows that, except for a few data points from the 1.65 mm bend bar specimen, all valid data are bounded by the Master Curve tolerance bounds and as expected, the Master Curve predicts the medium fracture toughness values.
2. Within one standard deviation ($\pm 1\sigma$), there is no obvious specimen size effect in 0.5T and 4 mm miniCT specimens for the measured Master Curve reference temperature T_0, whereas the 1.65 mm bend specimens yielded a higher T_{0Q} (a more conservative value) as shown in Figure 50. In addition, ORNL and CIEMAT T_0 results are consistent within $\pm 1\sigma$.

3. For the minimum number of specimens needed for evaluating T_0, ASTM E1921 requirements can be applied for 0.5T CT and 4 mm miniCT specimens, whereas, for 1.65 mm bend bar specimens, 12 uncensored tests are required for measured T_{0Q} to be converged within ±2σ from the final T_{0Q} based on random sampling, as shown in Figure 51.
4. Experimental quality control, especially the quality of fatigue precracking, is critical for yielding valid Master Curve results. Figure 52 shows one example of the impact of fatigue precrack on T_0. Due to the fatigue frame misalignment, the first batch of 0.5T CT specimens had skewed fatigue precrack fronts, and an unrealistically low T_0 was measured from these specimens. After improving the fatigue frame alignment, we obtained straight fatigue precrack fronts with the second batch of specimens and the measured T_0 was within the expected range.

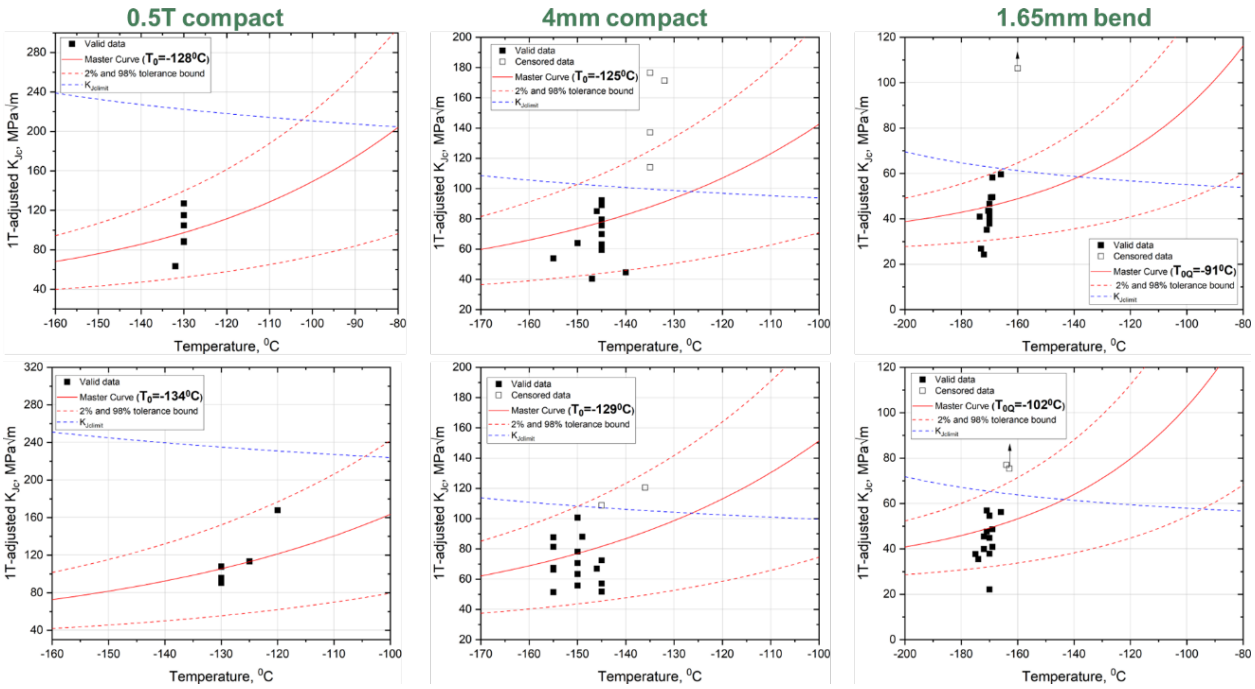

Figure 49. Master Curve results for EUROFER97 batch-3 on the top row and F82H-BA12 on the bottom row.

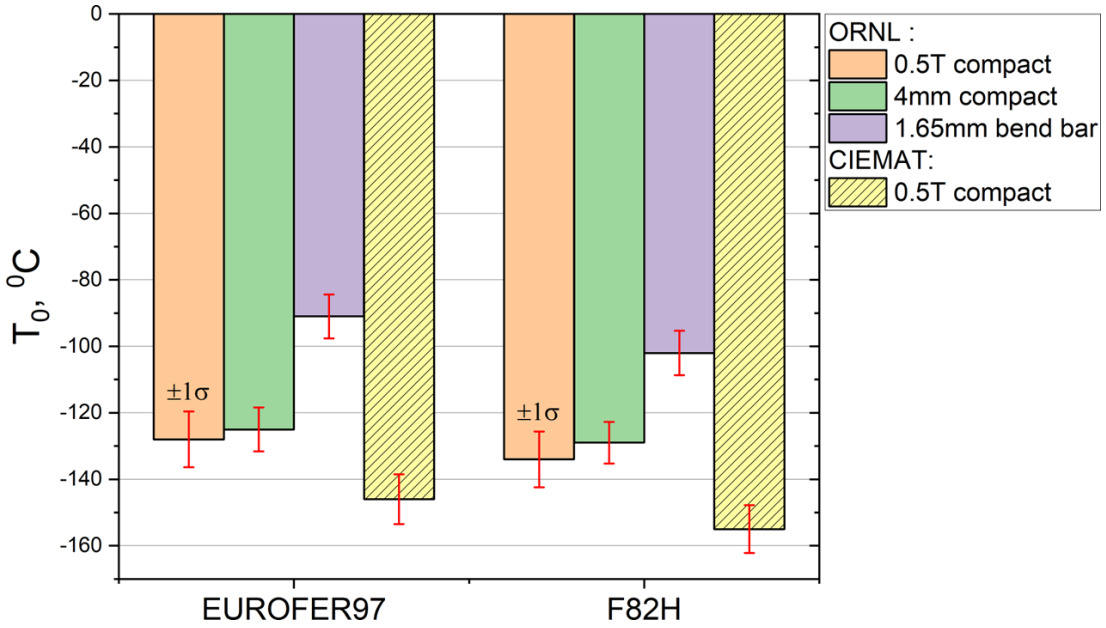

Figure 50. Comparison of measured Master Curve reference temperature T_{0Q} for EUROFER97 batch-3 and F82H-BA12 tested with three different specimen types. Error bars correspond to ± 1σ.

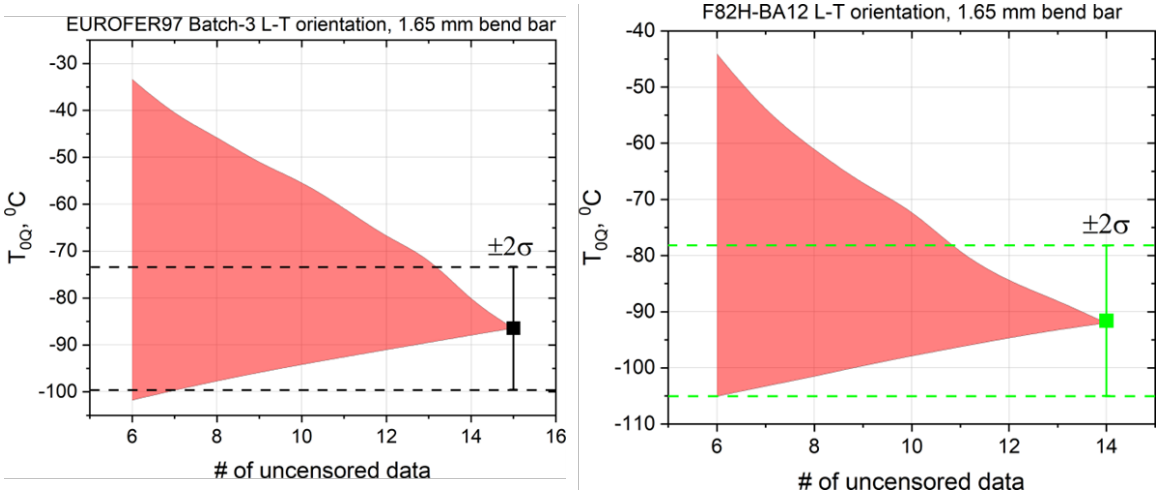

Figure 51. The effect of the number of uncensored data on T_{0Q} determination for 1.65 mm bend bar specimens based on random sampling.

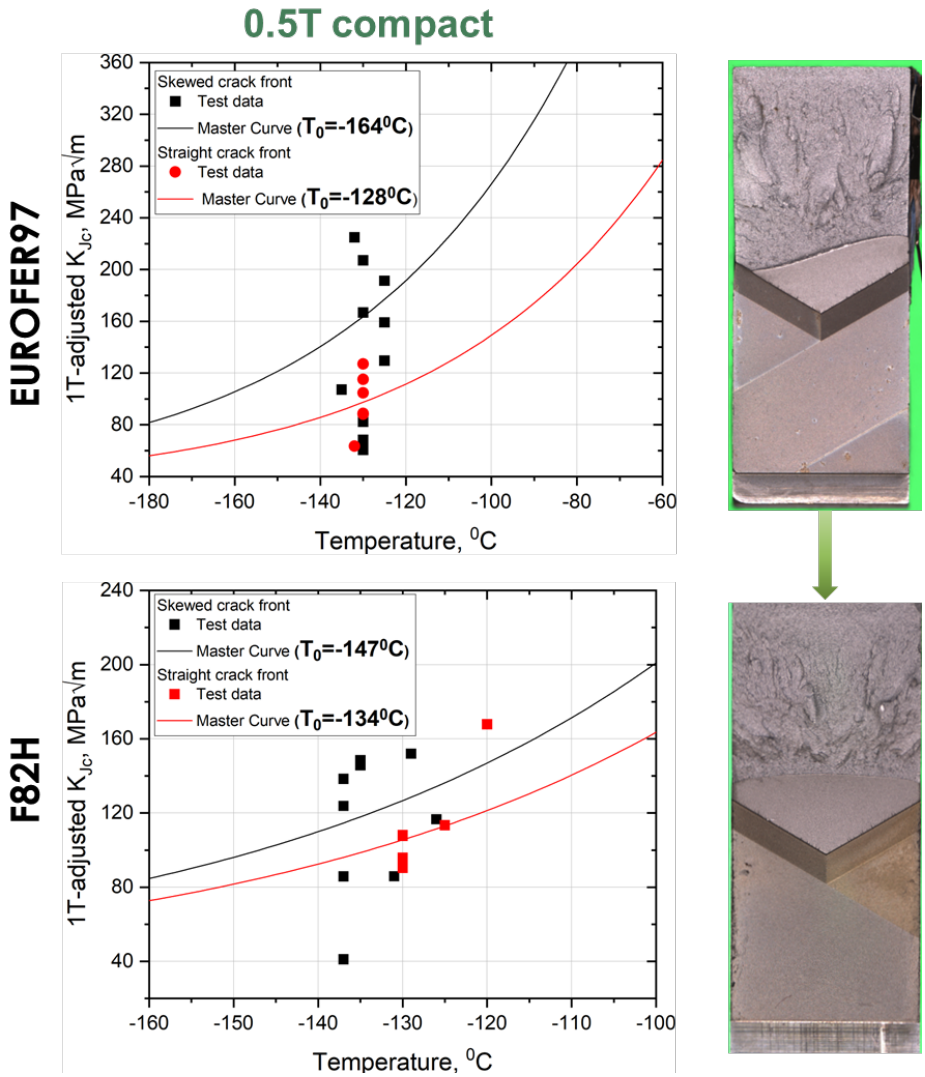

Figure 52. Effect of fatigue precrack front straightness on T_0.

12.1.4 FUTURE WORK

Current results will be published in a peer-reviewed journal. Additional efforts on rationalizing the bend bar specimen size effect will focus on potential loss of constraint, revisiting Master Curve methodology, etc. In addition, we plan to participate the Phase II of the IAEA CRP "Towards the Standardization of SSTT for Fusion Applications" starting in early 2023.

12.1.5 REFERENCES

[1] X. Chen et al., "SPECIMEN SIZE AND GEOMETRY EFFECTS ON THE MASTER CURVE FRACTURE TOUGHNESS MEASUREMENT OF EUROFER97 AND F82H STEELS", Fusion Materials Semiannual Report 6/30/2022, DOE/ER-313/72.

[2] X. Chen et al., “SPECIMEN SIZE AND GEOMETRY EFFECTS ON THE MASTER CURVE FRACTURE TOUGHNESS MEASUREMENTS OF EUROFER97 AND F82H STEELS”, Proceedings of the ASME 2022 Pressure Vessels & Piping Conference, July 17-22, 2022, Las Vegas, NV, USA, PVP2022-84514

13. HFIR IRRADIATION PROGRAM

13.1 FUSION 2022 FRONTIER TASK 3 IRRADIATION CAPSULE DESIGN

N. Russell (russellng@ornl.gov)

13.1.1 OBJECTIVE

The Fusion 2022 Frontier Task 3 irradiation program plans to irradiate five capsules with a design temperature of 400 °C. Loading will include FeCrAl tensile specimens and tin (Sn) shot designed to melt and interact with the specimens to test corrosion performance.

13.1.2 SUMMARY

The Fusion 2022 Frontier Task 3 irradiation program plans to irradiate FeCrAl tensile specimens submerged in molten Sn to determine corrosion effects during irradiation. The design has a target average specimen temperature of 400 °C for one HFIR cycle. Images of the design and thermal analysis for the molten Sn corrosion experiment are shown in Figure 53.

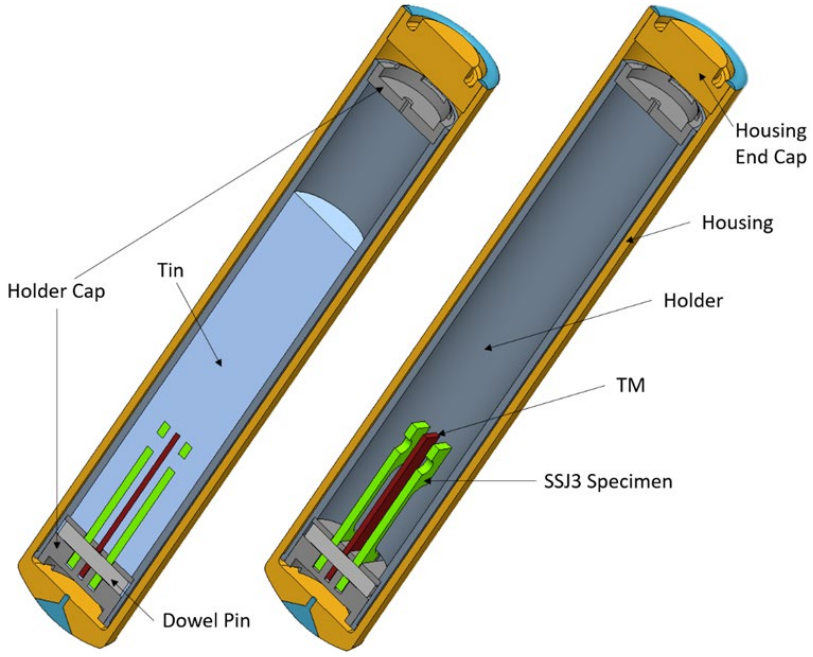

Figure 53. CAD representation (left) with Sn hidden for ease of viewing and representative thermal analysis (right) of Frontier Task 3 molten Sn corrosion irradiation capsules.

13.1.3 PROGRESS AND STATUS

These five rabbit capsules (SNF01-SNF05) were delivered to HFIR for irradiation in cycle 500. Cycle 500 was scheduled to start up on November 8, 2022, and end on December 2, 2022. An example set of capsule internal assembly photos is shown in Figure 54 with the completed capsule in Figure 55.

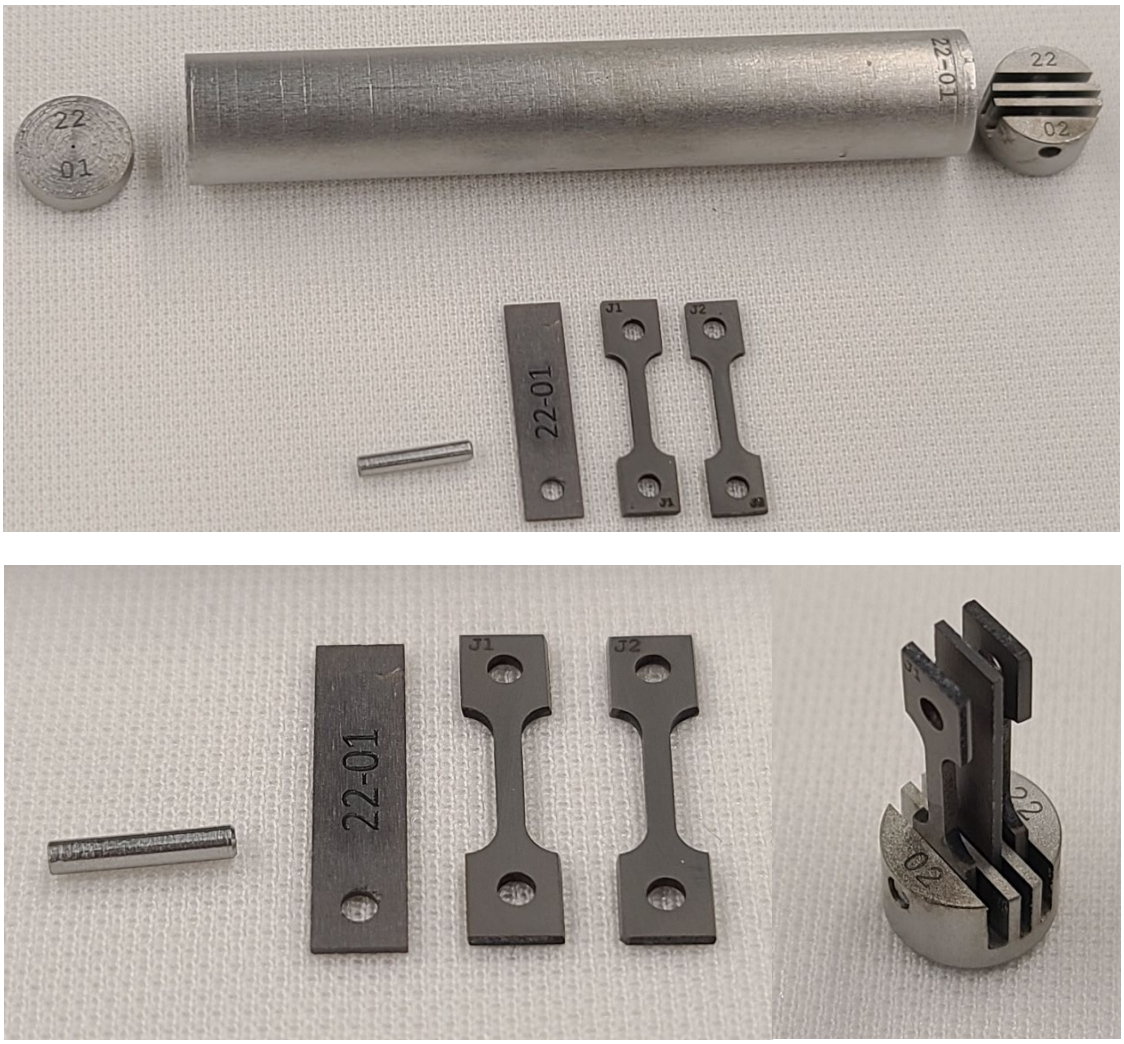

Figure 54: SNF01 internal parts.

Figure 55. SNF01 completed rabbit capsule.

The thermal safety calculation has been accepted by RRD for use in HFIR. As part of the safety review, a single molybdenum secondary containment was filled with tin, welded, and tested for leaks per standard building procedures. This secondary containment underwent a set of tests to prove that a breach in the holder was not likely due to thermal cycling or HFIR safety limiting condition scenario (LCS). The thermal cycling represents the event that HFIR has an unplanned scram, allowing the experiment to cool, and then

reheat when the reactor continues operation. The holder assembly was welded into a stainless-steel capsule to represent the inert atmosphere of the experiment and was heated in a furnace to 400 °C and allowed to cool, this was repeated for a total of five cycles. Then, the target was heated in the furnace to 750 °C to represent the experiment during an LCS in HFIR. No evidence of a failure in the holder assembly was witnessed. The holder assembly used for the heated testing was also used to perform a demonstration disassembly with the hot cell staff to give confidence the disassembly procedure.

A summary of the five rabbit capsule builds is shown in Table 10 with the predicted temperatures in Table 11. From the thermal analysis it is shown that the average TM temperature is about 7.4 °C hotter than the average specimen gauge region temperature. During post-irradiation examination, this temperature difference can be used to estimate the actual temperatures experienced in the specimen gauge region.

Table 10. Rabbit capsule build summary.

Capsule ID	Holder OD (mm)	Housing ID (mm)	Gas gap (μm)	Fill Gas	Specimen Type (Specimen IDs)
SNF01	9.350	9.521	85.5	Helium	Japan ODS (J1, J2)
SNF02	9.355	9.523	84.0	Helium	Japan ODS (J3, J4)
SNF03	9.360	9.527	83.5	Helium	ORNL ODS (O1, O2)
SNF04	9.350	9.522	86.0	Helium	ORNL ODS (O3, O4)
SNF05	9.360	9.525	82.5	Helium	APMT (1, 2)

Table 11. Design rabbit capsule temperatures.

Capsule ID	Part	Temperature (°C)		
		Avg	Max	Min
SNF01	Specimen	410.1	417.5	387.7
	Specimen Gauge	404.0	410.8	398.1
	TM	411.4	420.9	393.6
SNF02	Specimen	406.3	414.3	383.9
	Specimen Gauge	400.2	407.1	394.3
	TM	407.6	417.1	389.8
SNF03	Specimen	405.2	413.2	382.8
	Specimen Gauge	399.1	405.9	393.2
	TM	406.5	416.0	388.6
SNF04	Specimen	411.5	418.8	389.1
	Specimen Gauge	405.4	412.2	399.5
	TM	412.7	422.2	394.9
SNF05	Specimen	402.5	410.5	380.1
	Specimen Gauge	396.4	403.2	390.5
	TM	403.7	413.3	385.9

13.2 IRRADIATION OF QST F82H TENSILE AND BEND BAR SPECIMENS IN HFIR

N. Russell (russellng@ornl.gov), C. On, X. Chen, J. Geringer

13.2.1 OBJECTIVE

The objective of this task is the implementation of the general tensile (GENTEN) and general bend bar (GENBEN) designs for irradiation of QST F82H specimens in HFIR. There is a total of 21 irradiation capsules within this campaign consisting of three low dose (5 dpa) capsules and 18 high dose (50 and 80 dpa, 9 of each). There are three different average specimen irradiation temperatures of 300 °C, 400 °C, and 500 °C for these capsules.

13.2.2 SUMMARY

The temperature performance within an irradiation capsule is controlled by optimizing the specimen holder outer diameter (OD), holder material, and fill gas to create an insulating gas gap between the hot inner holder assembly and the cold capsule housing in direct contact with HFIR coolant. Much care and consideration were taken to apply the existing GENTEN and GENBEN designs. These designs developed a surface response model that allows the user to quickly and accurately determine a combination of holder OD, holder material, and fill gas to achieve an average specimen goal temperature. These two capsule designs can be seen below in Figure 56 and Figure 57.

QST requested hold points be introduced to our standard irradiation capsule build procedure. The first hold point form was for holder design approval. This allowed the ORNL PI and QST PI to be involved choosing appropriate holder ODs and the math behind the neutron induced swelling. All of the first hold point forms for the QST irradiation capsules have been reviewed and signed by the capsule designer, ORNL PI, and QST PI. The second hold point was introduced between assembly of the capsule parts and before welding. This hold point form for the capsules show pictures of every step in the assembly process so that QST could review the process and confirm specimen orientation. This hold form is approved for all capsules.

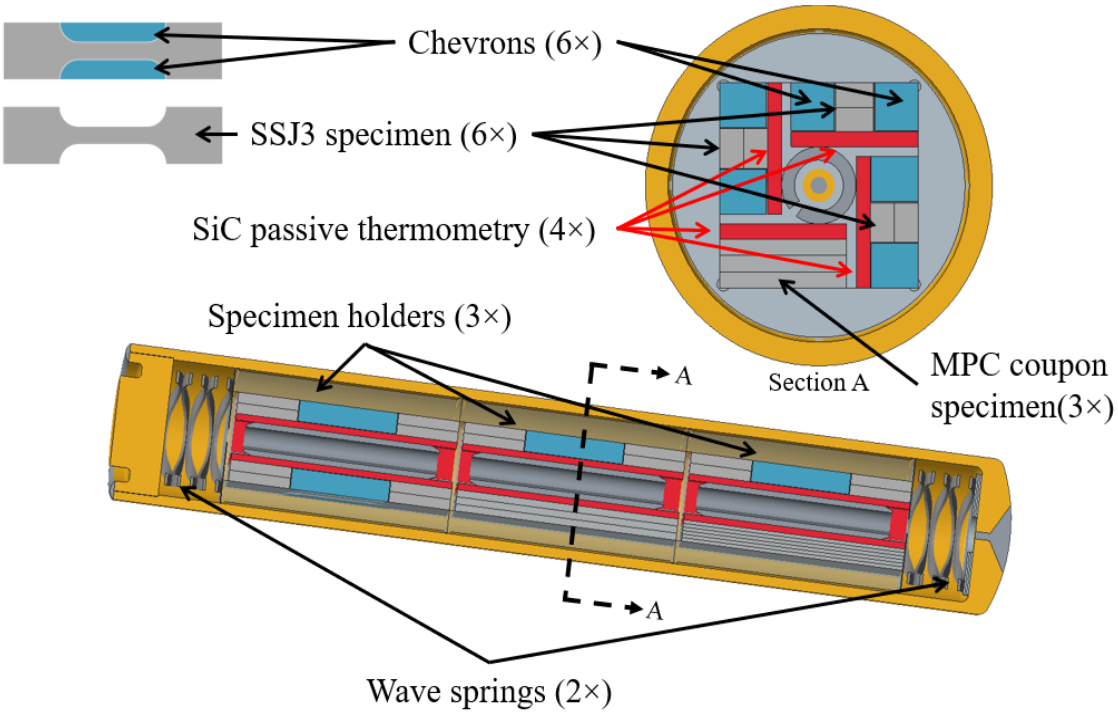

Figure 56. GENTEN irradiation capsule design

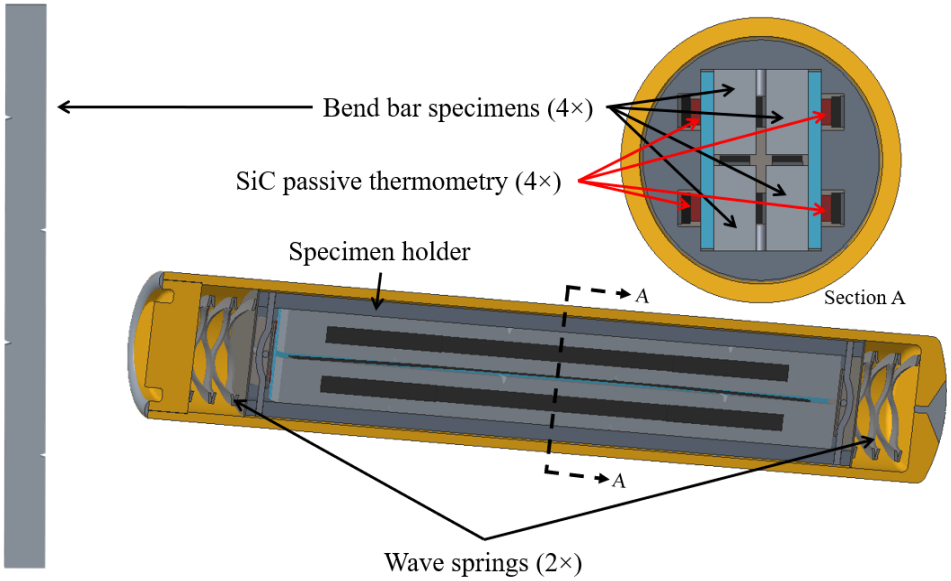

Figure 57. GENBEN irradiation capsule design.

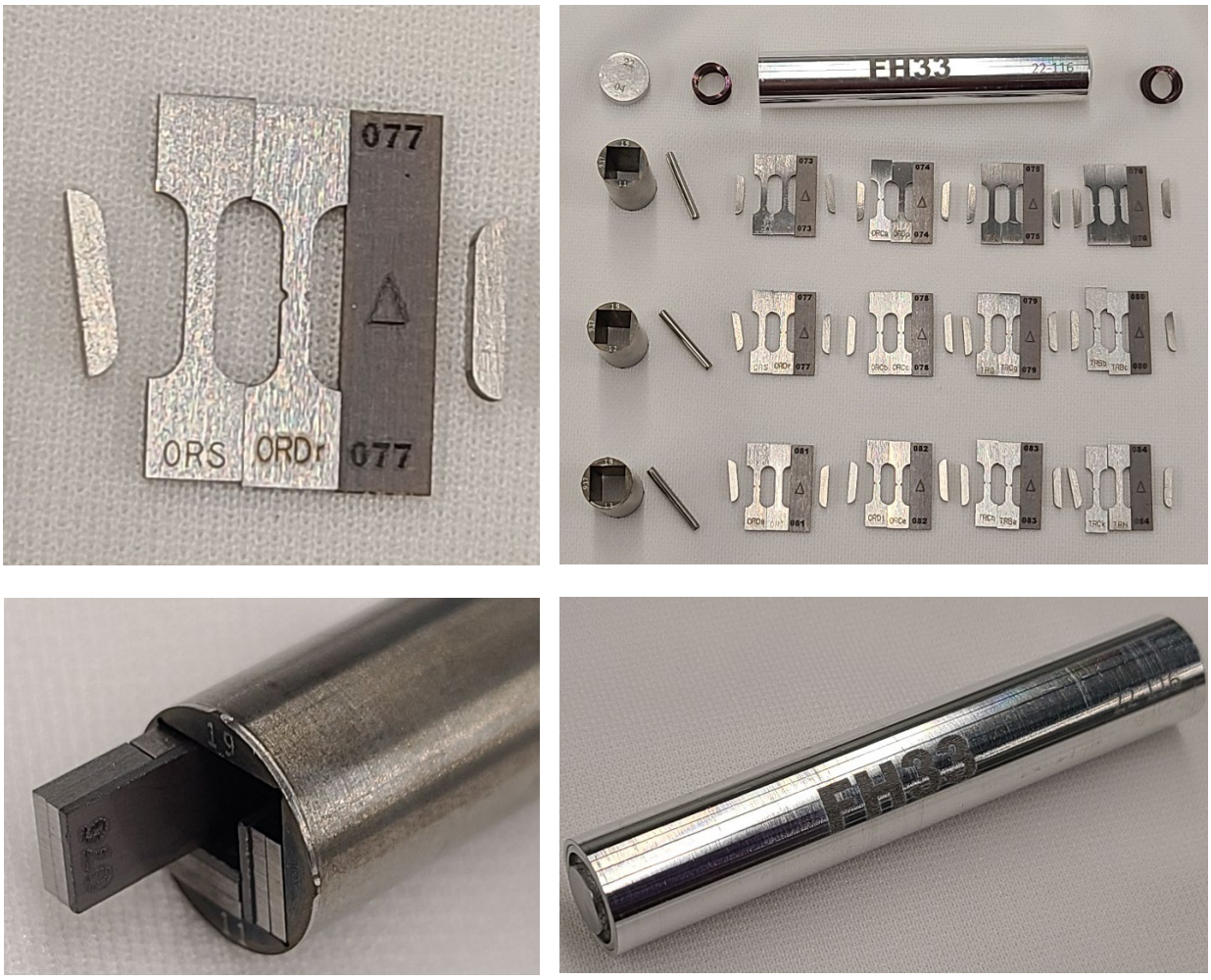

Figure 58. 50 dpa capsule GENTEN example (FH33).

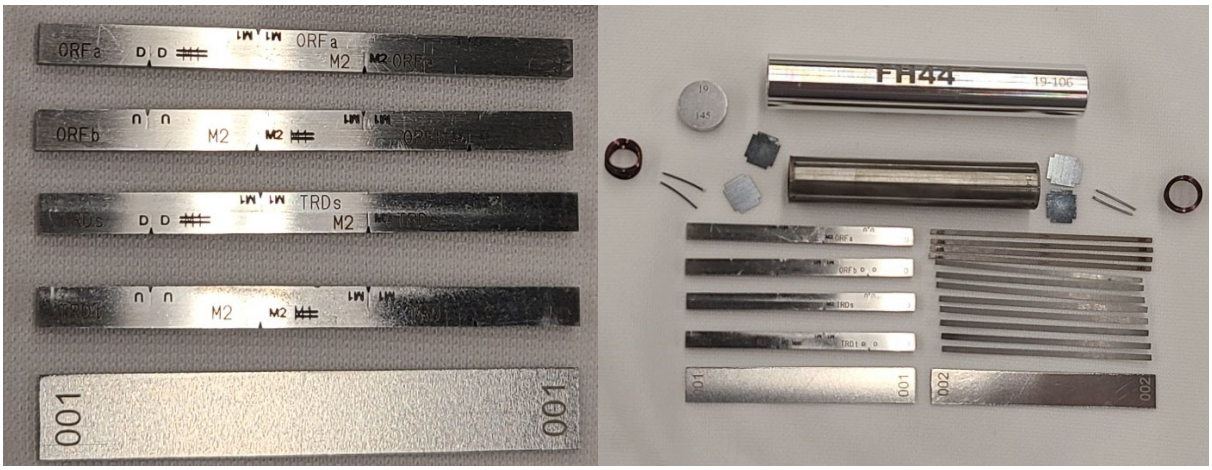

Figure 59. 50 dpa GENBEN example (FH44).

13.2.3 PROGRESS AND STATUS

Moving forward, all the low dose capsules have completed irradiation in HFIR (cycles 490-493). The 80 dpa irradiation capsules began irradiation in HFIR cycle 496 with capsule removal estimated to begin after cycle 541. The 50 dpa irradiation capsules have been accepted by HFIR and will begin irradiation in HFIR cycle 500 with capsule removal estimated to begin after cycle 528. Some example photos of the 50 dpa GENTEN assembly are shown in Figure 58, with a GENBEN example in Figure 59. All of the hold-point forms for the capsules have been approved and are included with the fabrication packages.

13.3 HFIR IRRADIATION EXPERIMENTS

C. On (onc1@ornl.gov)

13.3.1 SUMMARY

Neutron irradiation experiments were performed in support of the research and development of fusion reactor materials using various materials irradiation facilities in the High Flux Isotope Reactor (HFIR). The reactor operating history for the period from October 1, 2021 to September 30, 2022 is detailed in Table 12 and consists of five operating cycles.

Table 12. HFIR operating record for FY2022.

Cycle Number	Cycle End Date	Power (MWD)
495	October 17	2202.82
496*	February 4	2210.62
497	March 20	2183.34
498**	May 7	2152.69
499	October 23	2163.05

*Cycle was in three parts, due to reactor scram and electrical outage. Cycle 496A received 6.147 MWD, 496B received 890.653 MWD, while cycle 496C received 1313.82 MWD.

**Cycle was in two parts, due to reactor scram. Cycle 498A received 895.91 MWD, while cycle 496B received 1256.78 MWD.

Twenty-nine target zone rabbit capsules remain in the reactor to complete scheduled irradiations. These capsules are listed in Table 13 along with condensed information on the material, specimen type, temperature, fluence, and period of irradiation. Twenty rabbits have completed the scheduled irradiation as shown in Table 14.

Table 13. The rabbit capsules to continue irradiation in HFIR.

Experiment Designation	Primary Materials	Specimen Types	Irradiation Temperature (°C)	Max Exposure (dpa)	Number of Reactor Cycles	HFIR Cycles Start – End
FH11	F82H-IEA / F82H-mod3	Tensile	300	80	46	496 - 541
FH12	F82H-IEA / F82H-mod3	Tensile	400	80	46	496 - 541

FH13	F82H-IEA / F82H-mod3	Tensile	500	80	46	496 - 541
FH21	F82H-IEA / F82H-mod3	Bend Bar	300	80	55	496 - 550
FH22	F82H-IEA / F82H-mod3	Bend Bar	300	80	55	496 - 550
FH23	F82H-IEA / F82H-mod3	Bend Bar	400	80	55	496 - 550
FH24	F82H-IEA / F82H-mod3	Bend Bar	400	80	55	496 - 550
FH25	F82H-IEA / F82H-mod3	Bend Bar	500	80	48	496 - 543
FH26	F82H-IEA / F82H-mod3	Bend Bar	500	80	48	496 - 543
FMP07	F82H	Tensile	300	20	21	487 - 507
FMP08	F82H	Tensile	300	80	45	487 - 531
FMP11	F82H	Tensile	385	20	21	488 - 508
FMP12	F82H	Tensile	385	80	45	488 - 532
FMP14	F82H	Tensile	525	20	21	484 - 504
FMP17	F82H	Tensile/MPC*	650	80	45	484 - 528
FMP22	F82H	Bend Bar	300	20	21	488 - 508
FMP23	F82H	Bend Bars	300	80	45	488 - 532
FR11	Joint Tungsten Alloy	Disc (D6)	300	1.2	6	495 - 500
FR12	Joint Tungsten Alloy	Disc (D6)	300	1.2	6	497 - 502
FR53	Joint Tungsten Alloy	Disc (D3)	800	0.6	3	498 - 500
JCR11-03	SiC/SiC	Mini Bend Bar	950	200	100	487 - 586

JCR11-05	SiC/SiC	Mini Bend Bar	950	200	115	444 - 568
JCR11-08	SiC/SiC	Mini Bend Bar	950	200	115	444 - 560
JCR11-11	SiC/SiC	Mini Bend Bar	950	100	55	448 - 524
SCF4	SiC/SiC	Miniature Flexure Bar	250	100	90	457 - 547
SCF5	SiC/SiC	Miniature Flexure Bar	250	200	45	457 - 511
SCF8	SiC/SiC	Miniature Flexure Bar	600	100	45	457 - 502
SCF9	SiC/SiC	Miniature Flexure Bar	600	200	90	457 - 548
SCF11	SiC/SiC	Miniature Flexure Bar	950	100	57	458 - 517

*MPC= Multi-Purpose Coupon

Table 14. The rabbit capsules that completed irradiation in FY2022.

Experiment Designation	Primary Materials	Specimen Types	Irradiation Temperature (°C)	Max Exposure (dpa)	Number of Reactor Cycles	HFIR Cycles Start – End
FR01	Joint Tungsten Alloy	Disc (D6)	300	0.4	2	495 & 498
FR04	Joint Tungsten Alloy	Disc (D6)	500	0.2	1	495 - 495
FR07	Joint Tungsten Alloy	Disc (D6)	800	0.2	1	495 - 495
FR21	Joint Tungsten Alloy	Fracture Toughness Bar	300	0.2	1	496 - 496
FR22	Joint Tungsten Alloy	Fracture Toughness Bar	500	0.2	1	496 - 496

FR23	Joint Tungsten Alloy	Fracture Toughness Bar	800	0.2	1	496 - 496
FR32	Joint Tungsten Alloy	Disc (D3)	500	0.2	1	496 - 496
FR13	Joint Tungsten Alloy	Disc (D6)	500	0.6	3	495 - 497
F13B4	FeCrAlY Steel	Tensile	300	50	29	451 - 497
FR05	Joint Tungsten Alloy	Disc (D6)	500	0.2	1	498 - 498
FR06	Joint Tungsten Alloy	Disc (D6)	500	0.2	1	498 - 498
FR08	Joint Tungsten Alloy	Disc (D6)	800	0.2	1	498 - 498
FR15	Joint Tungsten Alloy	Disc (D6)	800	0.6	3	496 - 498
FR34	Joint Tungsten Alloy	Disc (D3)	800	0.2	1	498 - 498
FR02	Joint Tungsten Alloy	Disc (D6)	300	0.4	2	498 - 499
FR14	Joint Tungsten Alloy	Disc (D6)	500	0.6	3	497 - 499
FR31	Joint Tungsten Alloy	Disc (D3)	300	0.2	1	499 - 499
FR41	Joint Tungsten Alloy	Fracture Toughness Bar	300	0.6	3	497 - 499
FR42	Joint Tungsten Alloy	Fracture Toughness Bar	500	0.6	3	497 - 499

FR43	Joint Tungsten Alloy	Fracture Toughness Bar	800	0.6	3	497 - 499

14. AWARDS, HONORS, AND RECOGNITIONS

14.1 AWARDS DURING FY2022

14.1.1 S. J. ZINKLE:

- American Nuclear Society Seaborg medal (2022) for outstanding scientific or engineering research achievements associated with the development of peaceful uses of nuclear science.
- The Minerals, Metals and Materials Society (TMS) Leadership award (2022).

14.1.2 T. KOYANAGI:

- 2022 Masaji Yoshikawa Memorial Prize for Fusion Energy Award from the Fusion Energy Forum of Japan.

14.2 PUBLICATION HONORS IN FY2022

14.2.1 X. Hu

- Journal of Nuclear Materials 'Rising Star Awards', awardee.
- Appointed to the Editorial Board of the Journal of Nuclear Materials.

14.2.2 T. Koyanagi

- Journal of Nuclear Materials 'Rising Star Awards', finalist.

14.3 PROFESSIONAL RECOGNITION IN FY2022 AND CONTINUING

- The article titled “Future fusion reactors could be built on 3D-printed ceramics” was posted on Fusion and Fission Energy and Science Directorate website. (Led by Takaaki Koyanagi, DOE FES Fusion Materials Program) https://www.ornl.gov/organization-news/future-fusion-reactors-could-be-built-3d-printed-ceramics.
- The article titled “High-Energy X-Rays Open a New View of Degradation in Potential Fusion Reactor Material” was posted on the Office of Science website. (Led by Takaaki Koyanagi, DOE FES Fusion Materials Program) https://www.energy.gov/science/fes/articles/high-energy-x-rays-open-new-view-degradation-potential-fusion-reactor-material.
- Takaaki Koyanagi, Lead organizer of the symposium “Development and Applications of Advanced Ceramics and Composites for Nuclear Fission and Fusion Energy Systems” for the 46th International Conference and Expo on Advanced Ceramics and Composites (ICACC2022) virtual conference (Jan. 24-28).
- Takaaki Koyanagi, Brookhaven National Laboratory NSLSII Technical Review Panel.

15. PUBLICATIONS AND PRESENTATION IN FISCAL YEAR 2022

15.1 PAPERS PUBLISHED IN FY2022

1. **A. Bhattacharya, X. Chen, T. Graening, J. W. Geringer, J. Reed**, J. Henry, L. Pilloni, D. Terentyev, A. Puype, **T.S. Byun, Y. Katoh**, M. Rieth, and S. J. Zinkle, "Irradiation hardening and ductility loss of Eurofer97 steel variants after neutron irradiation to ITER-TBM relevant conditions," Fusion Engineering and Design 173 (2021) 112935. DOI: 10.1016/j.fusengdes.2021.112935
2. **A. Bhattacharya**, J. Henry, B. Decamps, **S.J. Zinkle**, and E. Meslin, "Helium causing disappearance of ½ a<111> dislocation loops in binary Fe-Cr ferritic alloys", Journal of Nuclear Materials 556 (2021) 153213, DOI: 10.1016/j.jnucmat.2021.153213
3. **A. Bhattacharya**, S.M. Levine, S.J. Zinkle, W.-Y. Chen, P. Baldo, **C.M. Parish,** and **P.D. Edmondson**, "Radiation induced amorphization of carbides in additively manufactured and conventional ferritic-martensitic steels: In-situ experiments on extraction replicas," Journal of Nuclear Materials, V563 (2022) 153646. DOI: 10.1016/j.jnucmat.2022.153646
4. **A. Bhattacharya**, S.J. Zinkle, J. Henry, S.M. Levine, **P.D. Edmondson**, M.R. Gilbert, H. Tanigawa, and **C.E. Kessel**, "Irradiation damage concurrent challenges with RAFM and ODS steels for fusion reactor first-wall/blanket: A review," Journal of Physics-Energy V4(3) (2022) 034003. DOI: 10.1088/2515-7655/ac6f7f
5. **T. S. Byun**, N. Bibhanshu, M. G. Gussev, and T. G. Lach, "Deformation mechanism transition in additively manufactured compositionally graded Fe-base alloys," JOM (2022) 1-17. DOI: 10.1007/s11837-022-05401-1
6. **N.O. Cetiner**, Y. Hatano, **J.L. McDuffee**, **D. Ilas**, **Y. Katoh, J.W. Geringer,** and T.Toyama, "Neutron irradiation of tungsten in hydrogen environment at HFIR," Fusion Engineering and Design, V178 (2022) 113089. DOI: 10.1016/j.fusengdes.2022.113089
7. **H. Gietl, T. Koyanagi, X. Hu**, M. Fukuda, A. Hasegawa, and **Y. Katoh**, "Neutron irradiation-enhanced grain growth in tungsten and tungsten alloys," Journal of Alloys and Compounds V901 (2022) 163419. DOI: 10.1016/j.jallcom.2021.163419
8. **H. Gietl**, J. Riesch, T. Höschen, M. Rieth, J.W. Coenen, R. Neu, "Charpy impact tests of tungsten fiber–reinforced composite from −150 °C to 1000 °C," Materials Letters V311 (2022) 131526. DOI: 10.1016/j.matlet.2021.131526
9. M.R. Gilbert, K. Arakawa, Z. Bergstrom, M.J. Caturla, S.L. Dudarev, F. Gao, A.M. Goryaeva, S.Y. Hu, X. Hu, R.J. Kurtz, A. Litnovsky, J. Marian, M-C Marinica, E. Martinez, E.A. Marquis, D.R. Mason, B.N. Nguyen, P. Olsson, **Y. Osetskiy**, D. Senor, W. Setyawan, M.P. Short, T. Suzudo, J.R. Trelewicz, T. Tsuru, G.S. Was, B.D. Wirth, L. Yang, Y. Zhang, **S.J. Zinkle**, "Prospectives on multiscale modelling and experiments to accelerate materials development for fusion" Journal of Nuclear Materials, 554 (2021) 153113. DOI: 10.1016/j.jnucmat.2021.153113.
10. **T. Graening**, M. Rieth, H. Leiste, and A. Moeslang, "On the mechanical alloying of novel austenitic dual-precipitation strengthened steels," Materials & Design V213 (2022) 110316. DOI: 10.1016/j.matdes.2021.110316

11. **T. Gräning** and **N. Sridharan**, "Benchmarking a 9Cr-2WVTa Reduced Activation Ferritic Martensitic Steel Fabricated via Additive Manufacturing," Metals V12(2) (2022) P. 342. DOI: 10.3390/met12020342

12. **T. Koyanagi**, "Irradiation-induced chemical disordering in ceramics: The case of SiC." Journal of Nuclear Materials, V565 (2022) 153766. DOI: 10.1016/j.jnucmat.2022.153766

13. T. Nozawa, **T. Koyanagi, Y. Katoh**, and H. Tanigawa, "Failure evaluation of neutron-irradiated SiC/SiC composites by underwater acoustic emission," Journal of Nuclear Materials V566 (2022), 153787. DOI: doi.org/10.1016/j.jnucmat.2022.153787

14. **T. Lach**, C. Silva, Y. Zhou, W. Boldman, P. Rack, W. Weber, and Y. Zhang, "Dynamic substrate reactions during room temperature heavy ion irradiation of CoCrCuFeNi high entropy alloy thin films," npj Materials Degradation V6 (2022) 60. DOI: 10.1038/s41529-022-00260-2

15. S.M. Levine, C. Pareige, Z. Jiao, **P.D. Edmondson**, G.S. Was, S.J. Zinkle, and **A. Bhattacharya**, "Phase instabilities in austenitic steels during particle bombardment at high and low dose rates," Materials & Design, V217 (2022) 110588. DOI: 10.1016/j.matdes.2022.110588

16. S.M. Levine, C. Pareige, Z. Jiao, **P.D. Edmondson**, G.S. Was, S.J. Zinkle, and **A. Bhattacharya**, "Data on Cu- and Ni-Si-Mn-rich solute clustering in a neutron irradiated austenitic stainless steel," Data in Brief V42 (2022) 108263. DOI: 10.1016/j.dib.2022.108263

17. **Y-R Lin, A. Bhattacharya**, D. Chen, Yajie Zhao, J-J Kai, J. Henry, and **S.J. Zinkle**, "The role of Cr concentration and temperature on cavity swelling with co-injected helium in dual ion irradiated Fe and Fe-Cr alloys", Materials & Design 223 (2022) 111134. DOI: 10.1016/j.matdes.2022.111134

18. Y.-R. Lin, **A. Bhattacharya**, and S.J. Zinkle, "The effect of helium on cavity swelling in dual-ion irradiated Fe and Fe-10Cr ferritic alloys," Journal of Nuclear Materials, V569 (2022) 153907. DOI: 10.1016/j.jnucmat.2022.153907

19. T. Muroga, Y. Hatano, D. Clark, and **Y. Katoh**, " Characterization and qualification of neutron radiation effects – Summary of Japan-USA Joint Projects for 40 years," Journal of Nuclear Materials, V560 (2022) 153494. DOI: 10.1016/j.jnucmat.2021.153494

20. N. Olynik, B. Cheng, D.J. Sprouster, **C.M. Parish**, and J.R. Trelewicz, "Microstructural Transitions during Powder Metallurgical Processing of Solute Stabilized Nanostructured Tungsten Alloys," Metals, V12(1) (2022): 159. DOI: 10.3390/met12010159

21. **Y. Osetsky**, "Strengthening of tungsten by coherent rhenium precipitates formed during low fluence irradiation," Tungsten V4 (2022) 20-27. DOI: 10.1007/s42864-021-00088-4

22. **C.M. Parish**, "Cluster Analysis of Combined EDS and EBSD Data to Solve Ambiguous Phase Identifications," Microscopy and Microanalysis, 28(2) (2022) P. 371-382. DOI: 10.1017/S1431927622000010

23. **A. Sabau**, K. Tokunaga, S. Gorti, Y. Ueda, **Y. Katoh,** and L. Snead , "Thermo-Mechanical Distortion of Tungsten-Coated Steel During High Heat Flux Testing Using Plasma Arc Lamps," Fusion Science and Technology, V78(4) (2022) P. 291-317. DOI: 10.1080/15361055.2021.1994325

24. D.J. Sprouster, **T. Koyanagi**, D.L. Drey, **Y. Katoh**, and L.L. Snead, "Atomic and microstructural origins of stored energy release in neutron-irradiated silicon carbide," Physical Review Materials (2021) V5(10), 103601. DOI: 10.1103/PhysRevMaterials.5.103601

25. A. Talignani, R. Seede, A. Whitt, S. Zheng, J.-C. Ye, I. Karaman, **M. Kirka, Y. Katoh**, and M. Wang, "A review on additive manufacturing of refractory tungsten and tungsten alloys," Additive Manufacturing, DOI: 10.1016/j.addma.2022.103009

26. Y. Zhao, **A. Bhattacharya**, C. Pareige, C. Massey, P. Zhu, J. Poplawsky, J. Henry, and S.J. Zinkle, "Effect of heavy ion irradiation dose rate and temperature on α′ precipitation in high purity Fe-18%Cr alloy," Acta Materialia V231 (2022) 117888. DOI: 10.1016/j.actamat.2022.117888

15.2 REPORTS ISSUED IN FY2022

1. —, "Fusion Materials Semiannual Progress Report for the Period Ending June 30, 2021," Volume 70
2. —, "Fusion Materials Semiannual Progress Report for the Period Ending December 31, 2021," Volume 71
3. M. G. Burke, Y. Katoh, S. Melton, F. W. Wiffen, "Fusion Materials Research at Oak Ridge National Laboratory in Fiscal Year 2021," ORNL/TM-2021/2352
4. C. M. Parish, Y. Katoh, and C. On, "ORNL Fusion Materials Program Quarterly Progress Report Highlight for the 1st Quarter of FY2022."
5. C. M. Parish, Y. Katoh, and C. On, "ORNL Fusion Materials Program Quarterly Progress Report Highlight for the 2nd Quarter of FY2022."

15.3 PAPERS SUBMITTED IN FY2022

1. N. Bibhanshu, M.N. Gussev, **T.S. Byun**, "Two-step deformation-induced martensitic transformation in additively manufactured High-Si stainless steel," Materials Science and Engineering-A (2022).
2. T. Koyanagi, C. Deck, "Novel ceramics processes for nuclear applications", Elsevier book chapter.

15.4 PRESENTATIONS DELIVERED IN FY2022

15.4.1 International Conference on Fusion Reactor Materials (ICFRM) 20

- Anne Campbell, et al., "Investigation of the Source of F82H Pressurized Creep Tube Behavior," Poster at ICFRM-20, October 24-29, 2021 (virtual)
- Y. Yamamoto, R.G. Miller, A.F. Rowcliffe, "Performance Evaluation of Advanced 3Cr-3WVTa Bainitic Steels," Poster at ICFRM-20, October 24-29, 2021 (virtual)
- Yuri Osetsky, German Samolyuk, "Estimating the strengthening parameters for irradiated alloys using atomic scale dislocation dynamics," Poster at ICFRM-20, October 24-29, 2021 (virtual)
- Yuri Osetsky, German Samolyuk, "Atomic-scale strengthening mechanisms in irradiated tungsten," Poster at ICFRM-20, October 24-29, 2021 (virtual)
- A. Bhattacharya, T. Nozawa, Chad Parish, Josina W. Geringer, Yutai Katoh, "Effect of helium on neutron irradiated mechanical properties and microstructure evolution of isotopically tailored 54Fe base F82H steel," Poster at ICFRM-20, October 24-29, 2021 (virtual)
- A. Bhattacharya, J. Poplawsky, H. Tanigawa, T. Nozawa, M. Rieth, S.J. Zinkle, Y. Katoh, "Understanding neutron irradiation induced hardening-embrittlement of RAFM steels by advanced characterization," Poster at ICFRM-20, October 24-29, 2021 (virtual)
- S.M. Levine, J. Poplawsky, D.T. Hoelzer, Y. Katoh, S.J. Zinkle, A. Bhattacharya, "Dose and temperature effect on solute nanoclustering in neutron irradiated oxide dispersion strengthened alloys," Poster at ICFRM-20, October 24-29, 2021 (virtual)
- Y. Li, A. Bhattacharya, Y. Zhao, S.J. Zinkle, "Loop formation in ion-irradiated Fe and Fe-Cr alloys at different temperatures," Poster at ICFRM-20, October 24-29, 2021 (virtual)
- Adrian Schrell, et al., "Recent Advances in Irradiation Capabilities for Fusion Materials in HFIR," Presentation at ICFRM-20, October 24-29, 2021 (virtual)
- L. M. Garrison, J. R. Echols, N. C. Reid, T. Miyazawa, A. Hasegawa, Y. Katoh, "Mechanical Properties of Neutron Irradiated Tungsten as a Function of Transmutation," Invited presentation at ICFRM-20, October 24-29, 2021 (virtual)
- Chad M. Parish and Arunodaya Bhattacharya, "High-Throughput Characterization of Carbides in RAFM Fusion Steels," Invited presentation at ICFRM-20, October 24-29, 2021 (virtual)
- S.J. Zinkle. Y.R. Lin, Y. Zhao, S.M. Levine, Y. Li, L. Wang, S. Agarwal, A. Bhattacharya, R.E. Stoller, "Fundamental Aspects of radiation effects in materials science," Keynote at ICFRM-20, October 24-29, 2021 (virtual)
- Takaaki Koyanagi, Yutai Katoh, Kurt Terrani, Shay Harrison, Jian Liu, "Additive manufacturing of silicon carbide for nuclear applications," Invited presentation at ICFRM-20, October 24-29, 2021 (virtual)
- Omer Karakoc, Takaaki Koyanagi, Takashi Nozawa, Yutai Katoh, "Fiber/matrix debonding of SiC/SiC composites evaluated using the micropillar compression technique," Presentation at ICFRM-20, October 24-29, 2021 (virtual)
- Tim Graening, Weicheng Zhong, Lizhen tan, Priyam Patki, Kevin Field, "Role of MC and M23C6 Precipitates in Radiation Resistance and Helium Distribution" Presentation at ICFRM-20, October 24-29, 2021 (virtual)
- Tim Graening, Niyanth Sridharan, "Benchmarking a 9Cr 2WVTa Reduced Activation Ferritic Martensitic Steel Fabricated via Additive Manufacturing for Fusion Applications" Poster at ICFRM-20, October 24-29, 2021 (virtual)
- Yao Li, Arun Bhattacharya, Yajie Zhao, S.J. Zinkle, "Loop formation in ion irradiated Fe and Fe-Cr alloys at different temperatures", 20th International Conference on Fusion Reactor Materials (virtual meeting), Oct. 24-29, 2021
-

15.4.2 MATERIALS IN NUCLEAR ENERGY SYSTEMS (MINES)

- Y. Zhao, A. Bhattacharya, C. Pareige, C. Massey, J. Poplawsky, P. Zhu, J. Henry, S.J. Zinkle, "The Kinetics and Stability of Alpha Prime (a') Precipitates in FeCr Binary Alloy under Ion Irradiations," Materials in Nuclear Energy Systems (MiNES), November 8-11, 2021, Pittsburgh, PA and virtual
- Y. Li, A. Bhattacharya, L. Wang, Y. Zhao, J. Henry, S.J. Zinkle, "Effect of Cr and Temperature on Dislocation Loops in Heavy Ion Irradiated Ultra-high Purity FeCr Alloys," Materials in Nuclear Energy Systems (MiNES), November 8-11, 2021, Pittsburgh, PA and virtual
- Y.R Lin, A. Bhattacharya, J. Henry, S.J. Zinkle, "Cavity formation in irradiated Fe and FeCr ferritic alloys," Materials in Nuclear Energy Systems (MiNES), November 8-11, 2021, Pittsburgh, PA and virtual
- SM. Levine, A. Bhattacharya, A.R. Lupini, D.T. Hoelzer, Y. Katoh, S.J. Zinkle, "Dose and Temperature Effect on Dispersoids in Neutron Irradiated Oxide Dispersion Strengthened (ODS) Alloys," Materials in Nuclear Energy Systems (MiNES), November 8-11, 2021, Pittsburgh, PA and virtual
- A. Bhattacharya, S.M. Levine, Y. Katoh and S.J. Zinkle, "Low Temperature Hardening-Embrittlement Phenomenon in 9-14% Chromium Based Ferritic-Martensitic and Oxide Dispersion Strengthened Steels" (invited), Materials in Nuclear Energy Systems (MiNES), Pittsburgh, PA, Nov. 8-12, 2021
- A. Bhattacharya, S.M. Levine, Y. Katoh and S.J. Zinkle, "Low Temperature Hardening-Embrittlement Phenomenon in 9-14% Chromium Based Ferritic-Martensitic and Oxide Dispersion Strengthened Steels" (invited), Materials in Nuclear Energy Systems (MiNES), Pittsburgh, PA, Nov. 8-12, 2021
-

15.4.3 TOKAI VIRTUAL CONFERENCE

- Takaaki Koyanagi, Yutai Katoh, Sosuke Kondo, "Damage processes in fusion structural ceramics under neutron and ion irradiation" Invited presentation at the 30th International Toki virtual Conference, November 17, 2021 (virtual)

15.4.4 THE MINERALS, METALS, AND MATERIALS SOCIETY (TMS) 2022

- Takaaki Koyanagi et al., "Characterization of atomic-scale defects in neutron irradiated silicon carbide," Oral at TMS 2022 Annual Meeting & Exhibition, February 27-March 3, 2022
- A. Bhattacharya, Samara Levine, Xiang Chen, Takashi Nozawa, S.J. Zinkle and Yutai Katoh, "Low temperature hardening embrittlement in neutron irradiated ODS steels", TMS 2022 Annual Meeting & Exhibition, February 27-March 3, 2022
- Yan-Ru Lin, A. Bhattacharya, J. Henry and S.J. Zinkle, "Effect of Cr and He on Cavity Swelling in Dual-Ion Irradiated High Purity Fe-Cr Alloys", TMS 2022 Annual Meeting & Exhibition, February 27-March 3, 2022
- Yao Li, Yajie Zhao, A. Bhattacharya, Ling Wang and S.J. Zinkle, "Dislocation loop formation in self-ion irradiated ultra-high purity Fe-Cr Alloys", TMS 2022 Annual Meeting & Exhibition, February 27-March 3, 2022

15.4.5 ELECTRON BACKSCATTER DIFFRACTION (EBSD) 2022

- C. M. Parish, "Materials Science Applications of EBSD," invited tutorial at Electron Backscatter Diffraction 2022 (virtual), June 7-9, 2022

15.4.6 TECHNOLOGY OF FUSION ENERGY (TOFE) 2022

Technology of Fusion Energy (ToFE) was a topical meeting within the American Nuclear Society (ANS) meeting.

- C. M. Parish and P. D. Edmondson, "Analytical Electron Microscopy, Atom Probe, and Machine Learning for Transmutation Characterization," presentation at Technology of Fusion Energy, June 2022, Anaheim, CA, USA.
- D. Sprouster, L.L. Snead, J. Trelewicz, Y. Katoh, T. Koyanagi, W. Zhong, "Advanced Synchrotron Characterization Techniques for Fusion Materials Science," presentation at Technology of Fusion Energy, June 2022, Anaheim, CA, USA.
- A. Bhattacharya, S.J. Zinkle, S.M. Levine, M. Gilbert "Effect of Transmutation in Fusion First-Wall/Blanket Steels: Current Challenges and Path Forward," presentation at Technology of Fusion Energy, June 2022, Anaheim, CA, USA.
- L.M. Garrison, J.R. Echols, N.C. Reid, Y. Katoh (ORNL), "Transmutation Effects on Mechanical and Thermal Properties of Tungsten," presentation at Technology of Fusion Energy, June 2022, Anaheim, CA, USA.
- X. Chen *et al*., "Small Specimen Test Technique Development for Materials Qualification Using Fusion Neutron Source," presentation at Technology of Fusion Energy, June 2022, Anaheim, CA, USA.
- N.C. Reid, L.M. Garrison, T. Marchhart, J.P. Allain, "Flexural Testing of Neutron Irradiated Tungsten Materials by Three-Point Bend," presentation at Technology of Fusion Energy, June 2022, Anaheim, CA, USA.
- X. Chen, M. Serrano, R. Hernández, M.A. Sokolov, "Influence of Fatigue Precracking and Specimen Size on the Master Curve Fracture Toughness Measurements of EUROFER97 and F82H Steels," presentation at Technology of Fusion Energy, June 2022, Anaheim, CA, USA.
- M. Romedenne, B.A. Pint, Y. Zhang, " Corrosion Behavior of SiC and Aluminized F82H in flowing PbLi" presentation at Technology of Fusion Energy, June 2022, Anaheim, CA, USA
- I. Robin, T. Graening, Y. Yang, Y. Katoh, S. Zinkle "Microstructure and Thermal Stability Analysis of a Novel Transition Layer Joining of Tungsten and Reduced Activation Ferritic Martensitic Steel", presentation at Technology of Fusion Energy, June 2022, Anaheim, CA, USA
- S.J. Zinkle, L. Snead, Y. Katoh, N. Ghoniem, J. Marian, J. Trelewicz, K. Field, W. Setyawan, B. Wirth and G.R. Odette, Progress and Challenges for Fusion Materials " (invited plenary) at Technology of Fusion Energy, June 2022, Anaheim, CA, USA

15.4.7 INTERNATIONAL CONFERENCE ON ION BEAM MODIFICATION OF MATERIALS

- S.J. Zinkle, Y-R Lin, Y. Zhao, S. Levine, L. Wang, S. Agarwal and R.E. Stoller, "Fundamental Radiation Effects in Materials due to Ion Bombardment: Beyond NRT-DPA, ARC-DPA and RPA" (invited), International Conference on Ion Beam Modification of Materials, Lisbon, Portugal, July 11-15, 2022

15.4.8 15TH INTERNATIONAL CONFERENCE ON MODERN MATERIALS AND TECHNOLOGIES (CIMTEC 2022)

- X. Chen, M. Serrano, R. Hernandez, M.A. Sokolov, Y. Katoh, S. Gonzalez De Vicente, "Development of Small Specimen Test Technique for Master Curve Fracture Toughness Measurement of EUROFER97 and F82H", presented at the 15TH International Conference on Modern Materials and Technologies (CIMTEC 2022), June 2022, Perugia, Italy

15.4.9 ASME PRESSURE VESSELS & PIPING CONFERENCE 2022

- X. Chen, M. Serrano, R. Hernandez, M.A. Sokolov, Y. Katoh, S. Gonzalez De Vicente, "Specimen Size and Geometry Effects on the Master Curve Fracture Toughness Measurements Of EUROFER97 and F82H Steels", presented at the ASME Pressure Vessels & Piping Conference 2022, July 2022, Las Vegas, NV, USA

15.4.10 SYMPOSIUM ON FUSION TECHNOLOGY (SOFT) 2022

- T. Graening, Y. Yang, W. Zhong, T.M.K. Green, P. Patki, K. Field, "Castable Nanostructured Alloy Steels as Enhanced Reduced Activation Ferritic Martensitic Steel", presented at the 32nd Symposium on Fusion Technology, September 2022, Dubrovnik, Croatia
- Y. Yamamoto, R.G. Miller, T. Graening, A.F. Rowcliffe, "Advanced 3Cr-3WVTa bainitic steel development for large-scale fusion structural applications," presented at the 32nd Symposium on Fusion Technology (SOFT 2022), September 2022, Dubrovnik, Croatia
- A. Bhattacharya, T. Graening, X. Chen, Y. Katoh "Irradiation Behavior of Eurofer97 Steels - An ORNL-EUROfusion Collaboration", presented at the 32nd Symposium on Fusion Technology (SOFT 2022), September 2022, Dubrovnik, Croatia